

Yiu, Wai Kin (2025) Impact of doping and interfacial band bending of charge transport layer in inverted perovskite solar cells. PhD thesis.

https://theses.gla.ac.uk/85488/

Copyright and moral rights for this work are retained by the author

A copy can be downloaded for personal non-commercial research or study, without prior permission or charge

This work cannot be reproduced or quoted extensively from without first obtaining permission from the author

The content must not be changed in any way or sold commercially in any format or medium without the formal permission of the author

When referring to this work, full bibliographic details including the author, title, awarding institution and date of the thesis must be given

Enlighten: Theses
https://theses.gla.ac.uk/
research-enlighten@glasgow.ac.uk

Impact of Doping and Interfacial Band Bending of Charge Transport Layer in Inverted Perovskite Solar Cells

Wai Kin YIU

Thesis submitted in fulfillment of the requirements for the degree of Doctor of Philosophy

School of Chemistry
College of Science and Engineering
University of Glasgow

September 2025

Abstract

This thesis investigates the n-doping reaction mechanism and interfacial band bending of charge transport layers (CTLs) in inverted perovskite solar cells (PSCs). CTLs, comprising electron transport materials (ETMs) and hole transport materials (HTMs), play a crucial role in determining the efficiency of PSCs by facilitating efficient charge extraction and transport while minimising recombination losses. However, device performance is often hindered by challenges such as low intrinsic conductivity of organic ETMs. To address these challenges, this work explores the n-type doping in non-fullerene organic ETMs, with a focus on improving conductivity and studies self-assembled monolayers (SAMs) as HTMs, understanding the influence of fermi levels on high efficiency of inverted PSCs.

The study begins by examining functionalized bisflavin (BF) derivatives and naphthalenediimide (NDI) derivatives with glycol and alkyl side-chains as nonfullerene ETMs due to bio-inspired nature and more straightforward synthetic process, compared to conventional ETM such as [6,6]-phenyl-C61-butyric acid methyl ester (PCBM). Due to inherently lower conductivity of these pristine derivatives, n-type doping was performed to enhance the conductivity using the dopant to generate free radical, as confirmed through electron paramagnetic resonance (EPR) measurements. UV-vis absorption spectroscopy and conductivity studies revealed that derivatives with polar glycol side-chains (BFG and NDI-G) facilitated faster doping reactions compared to the non-polar alkyl counterparts (BFA and NDI-EtHx). This behaviour was attributed to the polarity compatibility between the glycol side-chains and the dopant, which promoted molecular interactions and enhanced the doping efficiency.

Interestingly, the BF and NDI systems exhibited distinct responses to doping effects. While the doped BF derivatives show limited improvement in charge transport, the doped NDI derivatives demonstrated significant conductivity enhancements. Optimised NDI-G doped materials achieved a conductivity exceeding 10⁻² S/cm, resulting in improved photovoltaic performance. Density functional theory (DFT) calculations explained these observations by highlighting

the formation of charge transfer complexes (CTCs) with strong binding energies. The alignment of energy levels between CTC and neutral molecules was found to be critical for effective electron transfer and the generation of free charges. Based on these findings, a detailed doping mechanism is proposed in this work.

Additionally, bulk defects such as ion vacancies caused the surface recombination in the PSC system, it is necessary to decouple the charge accumulation from recombination. In here, we investigate using a novel stabilization and pulse (SaP) measurement technique to decouple the ionic feature with electronic effect, studying the influence of SAMs on Fermi-level alignment in PSCs. SAMs with varying dipole moments (MeO-2PACz, Me-4PACz, and 2PACz) were studied, revealing distinct flat ion potentials (V_{flat}) that affected charge extraction efficiency. An optimal V_{flat} of approximately 0.8 V was identified, while higher values were associated with interfacial barriers and reduced performance. Supporting evidence from Kelvin probe microscopy (KPFM) and time-resolved photoluminescence (TRPL) further confirm this hypothesis.

In summary, this thesis contributes insights into the charge transport and recombination through the n-type doping of non-fullerene organic ETMs and the interfacial band bending of SAM-based HTMs in inverted PSCs. The findings underline the strategic importance the doping mechanism and the critical role of interfacial engineering in enhancing photovoltaic performance. These results have broader implications for advancing efficient perovskite-based solar technologies.

Declaration

I declare that the thesis represents my own work under supervision of Prof. Graeme Cooke and Dr. Pablo Docampo, except where due acknowledgement is made, and that it has not been previously included in a thesis, dissertation or report submitted to this University or to any other institution for a degree, diploma or other qualifications.

Name:

Acknowledgements

I would like to thank my supervisor, Prof. G. Cooke, and Dr. P. Docampo, for allowing me to join their research groups and mentoring me during my doctoral research. Their guidance has been instrumental in shaping my understanding of the research process, from formulating hypotheses to addressing research questions, and instilled in me a positive attitude toward learning and embracing the essence of science.

I extend my gratitude to Dr. M. Cariello, Dr. D. Wilkinson, Dr. L. Mackenzie, A. Shaka, A. Sekar, G. Macleod, Dr. N. Pant, Dr. B. Vella, M. Giza, F. Angus and M. McRoberts, for their assistance throughout my studies. I am also immensely grateful to Prof. A. B. Djurišić at the University of Hong Kong for her guidance during my placement, as well as to her group members, Dr. H. Mo, Miss Y. Li, Dr. M. U. Ali, and J. Wang, for their support. Acknowledge to Dr. D. Wilkinson and Dr. L. Mackenzie for their materials synthesis and DFT calculations, and to F. Angus for his support with SaP measurements during the publication of our work. I also thank Dr. S. Sproules for his help with EPR measurements.

List of Publications

- W. K. Yiu, D. Wilkinson, M. Cariello, M. Giza, N. Pant, N. Mohammed, B. Vella, S. Sproules, G. Cooke and P. Docampo, "n-type Doping of Bio-Inspired Electron Transporting Materials: The Influence of Charge-Transfer Complexation", RSC Energy Adv., 2024, 3, 2939-2946
- W. K. Yiu, L. Mackenzie, D. Wilkinson, M. Giza, B. Vella, M. Cariello, S. Sproules, G. Cooke and P. Docampo, "Influence of Imide Side-chain Functionality in the Doping Characteristics of Naphthalenediimide Derivatives for Enhanced Electron Transport in Perovskite Solar Cells", *Phys. Chem. Chem. Phys.*, 2025,27, 11898-11906
- F. J. Angus[†], W. K. Yiu[†], H. Mo, T. L. Leung, M. U. Ali, Y. Li, J. Wang, A. W. Y. Ho-Baillie, G. Cooke, A. B. Djurišić, P. Docampo, "Understanding the Impact of SAM Fermi Levels on High Efficiency p-i-n Perovskite Solar Cells", *J. Phys. Chem. Lett.*, 2024, 15, 10686–10695 († equally contribution)
- 4. R. Serrano-Nieto, <u>W. K. Yiu</u>, M. Giza, G. Cooke, P. Horcajada, Y. Pérez, P. Docampo, Controlling Band-Bending for Perovskite Optoelectronic Devices Using Bismuth-Based Interlayers, Submitted
- M. Giza, F. J. Angus, <u>W. K. Yiu</u>, M. McRoberts, B. Vella, J. Wang, A. B. Djurišić, E. Arca,
 P. Docampo, The Case of the Vanishing Perovskite Layer, Cell Rep. Phys. Sci.,
 Accepted
- 6. H. Mo[†], D. Li[†], A. Sergeev, **W. K. Yiu**, J. Wang, G. Zhang, Z. Yuan, Y. Li, Y. He, T. Zhu, M. Y. Lam, F. J. Angus, W. D. Li, J. Tang, K. S. Wang, G. Cooke, P. Docampo, J. Popović, G. Li and A. B. Djurišić, Fullerene Derivative Layer as a Charge Transfer Bridge for efficient and stable Perovskite Solar Cells, Adv. Funct. Mater., Accepted

Table of Contents

Declaration	i
Acknowledgements	ii
List of Publications	iii
Table of Contents	iv
List of Figures	vi
List of Tables	xi
Lists of abbreviations	xii
Lists of symbols	xvi
Chapter 1. Introduction 1.1. Overview of Solar Cells	1
1.2. The Emergence of Perovskite Solar Cells	2
1.3. Challenge of Perovskite Solar Cells	2
1.4. Thesis Outline	3
Chapter 2. Fundamental 2.1. Perovskte Solar Cell Structure and Operation	6
2.2. Compositional Flexibility of Perovskite Materials	10
2.3. Determination of Device Energetics	13
2.4. Advancements in Non-Fullerene Organic Electron Transport Materials	16
2.5. Enhancing Properties in Organic Electron Transport Materials Through n-type	40
Doping	19
Chapter 3. Expertimental Methods 3.1. Nickel Oxide Nanoparticles Synthesis	29
3.2. Inverted Perovskite Solar Cells Fabraication and Measurement	
3.2.1. Precursor Preparation	29
3.2.2. MAPbI ₃ and Double-cation Perovskite Based Device	30
3.2.3. Triple-cation Perovskite-Based Device	32
3.3. Characterisation	
3.3.1. Conductivtiy Measurement	33
3.3.2 Electron Paramagnetic Resonance Measurement	34
3.3.3. Scanning Electron Microscopy	36

37
37
39
40
42
44
46
: The
50
51
62
istics
67
68
85
p-i-n
90
91
105
109

List of Figures

- Figure 1.1. Structure of ABX₃ perovskites
- Figure 2.1. The architecture of a) regular and b) inverted PSCs
- Figure 2.2. a) Structure of 4Cl-BZS ligand and b)Record of PCEs of inverted and regular PSCs
- Figure 2.3. Working principle of in inverted PSC
- Figure 2.4. Typical J-V characteristic of photovoltaic device
- Figure 2.5. Device circuit models of a) bipolar transistor, V_C , V_B and V_E represent to the electrical potentials on collector, base and emitter terminals, respectively; and b) perovskite solar cell
- Figure 2.6. Schematic diagram of the formation of bonding and anti-bonding orbitals in perovskite due to hybridization of Pb and I atomic orbitals
- a) Side view and b) top view of the I- migration path for MAPbI₃; c) side view and d) top view for Ace_{0.25}MA_{0.75}PbI₃ perovskite and e) activation energies for iodide ion migration in MAPbI₃ and Ace_{0.25}MA_{0.75}PbI₃ systems, showing the maximum energy states associated with the hydrogen bond length between the migrating iodide ion and the nearest neighboring hydrogen atom
- Figure 2.8. Temperature dependent conductivity measurements of the a) MAPbI₃ and b) Ace_{0.25}MA_{0.75}PbI₃ devices
- Figure 2.9. Band diagrams of mobile ions of solar cell at a) after contact; b) in equilibrium in dark condition; c) after light illumination and d) in equilibrium under light illumination
- Figure 2.10. Simulation for vacancy density distribution of iodide at the interface between a) ETL/perovskite; b) perovskite/HTL (stabilisation voltages between 0 and 1.5 V) and c) electric potential distribution across the devices at 0.6 V pulse
- Figure 2.11. Structures of a) PCBM; b) flavin and c) NDI
- Figure 2.12. Structures of a) NDI-PM; b) NDI-PhE; c) DS1 and d) DS2
- Figure 2.13. Doping mechanism of a) ion pair formation of n-type doping and b) CTC formation
- Figure 3.1. Device pattern of MAPI and DC perovskite based device

- Figure 3.2. Device pattern of TC perovskite based device
- Figure 3.3 a) Pattern of etched ITO and b) conductivity measurement of the etched area
- Figure 3.4. Schematic diagram of an EPR spectrometer
- Figure 3.5. Comparison of a) absorption spectrum and b) ESR spectrum (first derivative)
- Figure 3.6. Schematic diagram of a) SEM components and b) operational principles
- Figure 3.7. Schematic diagram of X-rays incident on a crystal structure
- Figure 3.8. a) UV-vis absorption measurement and b) working principle
- Figure 3.9. Schematic diagram of energy level. Eopt represents the optical band gap between HOMO and LUMO. Efund is a fundamental gap, representing the energy difference between the IP and EA. Eb is the electron-hole pair binding energy. The Eopt is generally lower than Efund because the electron and hole remain electrostatically bound to another in the excited state
- Figure 3.10. Schematic diagram of charge carrier recombination process (Bimolecular-Trapping-Auger model)
- Figure 3.11. Illustration diagram of a) AM mode and b) FM mode
- Figure 3.12. Energy level diagram of sample and AFM tip: a) sample and tip are separated by distance, d with no electrical contact; b) sample and tip are electrical contact and c) external bias is applied to nullify the CPD. (E_v : vacuum energy level. E_{fs} and E_{ft} : Fermi energy levels of the sample and tip, respectively.)
- Figure 3.13. a) JV curves obtained from SaP measurements; b) Calculated gradient around Voc, with a 7-point 3rd order Savitzky-Golay filter applied to smooth the data; c) Second derivative of dJ/dV data, indicating the location of the steepest gradient and d) Final analysis of the electrostatic potential drop across the perovskite layer with shaded red region representing the range of linear fits
- Figure 4.1. Structures of BFA and BFG
- Figure 4.2. a) UV-vis absorption spectra of BFG and BFA in chlorobenzene (1 x 10⁻⁵ M); b) CV measurements of b) BFG and BFA, and c) N-DMBI (10⁻³ M in DMF,

scan rate 100 mV/s) with ferrocene as the reference, all redox processes are recorded by selecting a wide process window; and d) Energy levels of PCBM, BF derivatives and N-DMBI (HOMO/LUMO of BF derivatives calculated from DFT of BF)

- Figure 4.3. UV-vis absorption spectra of a) BFG and b) BFA in the presence of 0 mol% to 100 mol% N-DMBI; c) BFG and d) BFA with reaction times from 0 to 24 hours (Normalized at 558 nm, corresponding to one of the typical absorption peaks of pristine BF materials)
- Figure 4.4. EPR spectrum of a) BFG and b) BFA with and without N-DMBI in chlorobenzene ($\sim 2 \times 10^{-2} \, \text{M}$)
- Figure 4.5. a) Solid state UV-vis absorption spectra and b) conductivity measurement of BFG and BFA with and without N-DMBI
- Figure 4.6. J-V characteristics curves of champion devices based on PCBM, BFG and BFA PSCs
- Figure 4.7. Conductivity measurements of pristine PCBM films exposed in N_2 and air
- Figure 4.8. SEM images of a) PCBM, b) pristine BFG, c) pristine BFA, d) BFG and e)
 BFA with 20 mol% N-DMBI addition
- Figure 4.9. DFT calculations of energy levels of BF, [BF--] and [BF/N-DMBI].
- Figure 4.10. TD-DFT simulated UV-Vis spectra of neutral of BF and [BF/N-DMBI].
- Figure 4.11. a) ESP and b) spin density maps of [BF/N-DMBI].
- Figure 4.12. Calculated binding energies for [BF/N-DMBI]-, [BF/BF]- and BF/BF
- a) Structures of NDI-G, NDI-EtHx and N-DMBI; b) UV-vis absorption spectra of pristine NDI-G and NDI-EtHx (1 x 10⁻⁵ M in chlorobenzene); c) CV measurements of NDI-G and NDI-EtHx with ferrocene as reference (1 x 10⁻⁴ M in CH₂Cl₂; scan rate 0.1 mV/s); d) Energy levels of PCBM, methyl-NDI and N-DMBI (HOMO and LUMO levels of methyl-NDI obtained from DFT calculations) and e) conductivity measurements of pristine NDI-G, NDI-EtHx and PCBM self-doped in air
- Figure 5.2. EPR spectrum of pristine and after addition of N-DMBI for a) NDI-G (3.57x10⁻² M) and b) NDI-EtHx (4.08x10⁻² M) in chlorobenzene; c) UV-vis absorption spectra of pristine and after addition of N-DMBI for both NDI derivatives (1 x 10⁻⁵ M); d) simulated UV-vis spectra of neutral methyl-NDI,

- [methyl-NDI/ N-DMBI] complex and [methyl-NDI] radical anion
- Figure 5.3. a) Electrostatic potentials (ESPs) and b) spin density maps of [methyl-NDI/N-DMBI]• complex
- Figure 5.4. DFT predicted HOMO/LUMO maps and energies of methyl-NDI and [methyl-NDI/N-DMBI]•.
- Figure 5.5. a) DFT predicted HOMO/LUMO maps and energies of NDI-G and [NDI-G and [NDI-EtHx/N-DMBI]•
- Figure 5.6. UV-vis absorption spectra of a) NDI-G and b) NDI-EtHx in film on glass substrates with 50 mol% of N-DMBI in the presence of reaction times between 0 to 24 hours; c) NDI-G and d) NDI-EtHx in film on glass substrates in the presence of 0 mol% to 50 mol% of N-DMBI at 2 hours (NDI-G) and 16 hours (NDI-EtHx)
- Figure 5.7. UV-vis absorption spectra of NDI-G and NDI-EtHx films on glass substrates, each containing 50 mol% of N-DMBI. Solid lines represent data at 0 min, while dashed lines show spectra after 15 min of air exposure (The variations in absorption intensity spectra are mainly attributed to differences in film thickness, which arise from the spin-coating process. NDI molecules dissolve in chlorobenzene, and NDI-EtHx is more effectively solvated in nonpolar chlorobenzene, resulting in stronger intrinsic absorption. In contrast, NDI-G exhibits lower solubility than NDI-EtHx, leading to reduced absorbance. Film thickness can vary between the two materials, as the thicker or denser NDI-EtHx films further contribute to the higher absorption intensity)
- Figure 5.8. Logarithmic plot of conductivity measurements for N-DMBI doped in NDI-G and NDI-EtHx at a) reaction time ranging from 0 to 24 hours (50 mol% N-DMBI doping) and b) ranging from 0 mol% to 50 mol% (reaction time: 2 hours for NDI-G and 16 hours for NDI-EtHx). (Average of three samples with error bars for each data set) (The variation in conductivity for pristine NDI-G in Figure 5.8b is attributed to the variation for ITO substrates)
- Figure 5.9. a) J–V characteristic curves of champion devices based on PCBM, pristine, and doped NDI-G and NDI-EtHx PSCs (Lines represent to fitting curves of each J-V curves) and b) JV curves showing forward (dashed line) and

reverse (solid line) curves for devices incorporating PCBM, pristine and doped of NDI-G and NDI-EtHx. Figure 5.10. SEM images of a) PCBM; b) pristine NDI-G; c) pristine NDI-EtHx, d) doped NDI-G and e) doped NDI-EtHx

- Figure 6.1. SEM morphology analysis of DC perovskite on a) 2PACz, b) Me-4PACz and c) MeO-2PACz, as well as MAPI on e) 2PACz, f) Me-4PACz and g) MeO-2PACz. XRD analysis of d) DC and h) MAPI on all SAMs
- Figure 6.2. JV curves of a) DC perovskite and b) MAPI devices with the forward scans (dashed lines) and the reverse scans (solid lines). Normalised TRPL measurements for c) DC perovskite and d) MAPI films, measured in configuration of ITO/NiOx/SAM/perovskite
- Figure 6.3. Statistical analysis of DC perovskite devices for different SAMs under simulated solar illumination for forward scan; a) Jsc; b) Voc; c) FF and d) PCE. (10 devices for each condition)
- Figure 6.4. Statistical analysis of MAPI devices for different SAMs under simulated solar illumination for forward scan; a) Jsc; b) Voc; c) FF and d) PCE. (10 devices for each condition)
- Figure 6.5. AFM (left) and KPFM images of DC perovskite films in dark (middle) and under illumination (right) on different SAMs: a-c) 2PACz; d-f) Me-4PACz and g-i) MeO-2PACz with the partial device stack (ITO/NiOx NPs/SAMs/DC perovskite)
- Figure 6.6. JV curves from SaP measurements for a) MAPI and b) DC devices using different SAMs
- Figure 6.7. dJ/dV analysis of devices of a) MAPI and b) DC perovskite with different SAMs
- Figure 6.8. JV data from SaP measurement of MeO-2PACz on a) MAPI and b) DC perovskite with contrasting colours to highlight both scans taken during the measurement (reverse scans in black and forward scans in dashed red); Stabilisation data obtained during SaP measurement. Left: Full current density output obtained during each applied bias for MeO-2PACz on c) MAPI and e) DC perovskite. The red dashed lines indicate the final 30 seconds before pulsing for stability analysis. Right: the current minus

the average current during the final 30s before pulsing beginning for MeO-2PACz on d) MAPI and f) DC perovskite, confirming that the ionic configuration was stable before pulsing

- Figure 6.9. JV curves from SaP measurement utilising Cl-2PACz for a) MAPI and b) DC perovskite. dJ/dV analysis for Cl-2PACz-based devices for c) MAPI and d) DC
- Figure 6.10. Tauc analysis of a) DC perovskite and b) MAPI
- Figure 6.11. Energy level diagrams for inverted PSCs incorporating each SAM layer (HTL: NiOx/SAM and ETL: PCBM). The perovskite valence band edge is $5.4~{\rm eV}$ from literature.15 The electrostatic potential drop across the perovskite layer extracted from the SaP measurements is labelled as Vflat. The energetic offset from the valence band of the perovskite to the valence band of the HTL is labelled ΔE and is estimated from values obtained from the literature

Lists of Tables

- Table 4.1. Photovoltaic performance of PCBM, BF-based PSCs (10 devices for each condition)
- Table 5.1. Conductivity measurements for N-DMBI doped in NDI-G and NDI-EtHx at different mol%. Average of three samples with error for each data
- Table 5.2. Conductivity measurements for N-DMBI doped in NDI-G and NDI-EtHx at different reaction time. Average of three samples with error for each data
- Table 5.3. Photovoltaic performance of reference PCBM-based, pristine and doped NDI-G-based and NDI-EtHx-based PSCs (10 devices for each condition)
- Table 6.1. Average grain sizes of DC perovskite and MAPI on different SAMs, measured from approximately 120 grains for DC perovskite and 70 grains for MAPI. The values represent the mean grain size ± standard deviation
- Table 6.2. Extracted TRPL rate values of DC perovskite for different SAMs using the rate equation for the bimolecular-trapping model, obtained using the PEARs fitting tool. (k_1 = rate of monomolecular recombination, k_2 = rate of bimolecular recombination, n = photoexcited carrier concentration and t = time)
- Table 6.3. Extracted TRPL rate values for MAPI for different SAMs sing the rate equation for the bimolecular-trapping model, obtained using the PEARs fitting tool. (k_1 = rate of monomolecular recombination, k_2 = rate of bimolecular recombination, n = photoexcited carrier concentration and t = time)
- Table 6.4. Comparison of dipole moment and the flat ion potentials for the different SAMs on MAPI and DC

Lists of abbreviations

Atomic force microscopy

(4-(3,6-dimethyl-9H-carbazol-9-yl)butyl)phosphonic acid Me-4PACz [2-(3,6-dimethoxy9H-carbazol-9-yl)ethyl]phosphonic acid MeO-2PACz [2-(9H-carbazol9-yl)ethyl]phosphonic acid 2-PACz 4-(1,3-Dimethyl-2,3-dihydro-1H-benzoimidazol-2yl)phenyl)dimethylamine N-DMBI Absorbance Abs Acetamidinium Ace⁺ Activation energy E_a Amplitude modulation AM

Bathocuproine BCP
Bisflavin BF

Cadmium sulfide CdS

Cadmium telluride CdTe

Caesium iodide Csl

Charge transfer complex CTC

Charge transport layers CTLs

Chlorobenzene CB

Contact potential difference CPD

Contact potential difference V_{CPD}

Copper indium gallium selenide CIGS

Cross-sectional area of the thin film A

Current

Current at maximum power J_{max}

Cyclic voltammetry CV

Density functional theory DFT

Dimethyl sulfoxide DMSO

Dimethylformamide DMF

Distance between atomic planes d

Dye-sensitized solar cells DSSCs

AFM

Electron affinity EA

Electron paramagnetic resonance EPR

Electron transport layer ETL

ETM

Electronic charge e

Electron transport material

Electrostatic potentials ESPs

Energy dispersive X-ray spectroscopy EDX

Ethyl acetate EAce

External bias V_{DC}

Fill factor FF

Flat ion potential V_{flat}

Formamidinium iodide FAI

Frequency modulation FM

Fundamental gap E_{fund}

Gallium arsenide GaAs

Hole transport layer HTL

Hole transport material HTM

Incident power P_{in}

Indacenodithiophene

Indium-doped tin oxide ITO

Intensity of incident source

Intensity of light after absorption I_{Abs}

Intensity of light after reflection I_{Ref}

Intensity of light after transmission I_{Trans}

In pair formation

Ionization potential IP

Isopropanol

Kelvin probe force microscopy KPFM

Lead (II) bromide PbBr₂

Lead (II) chloride PbCl₂

Lead (II) iodide Pbl₂

Length of thin film L

Light emitting diodes LEDs

Magnetic field B

Maximum power P_{max}

Mean current J_{mean}

Methylammonium MA+

Methylammonium iodide MAI

Methylammonium lead iodide MAPI

Naphthalenediimide NDI

Nickel (II) nitrate hexahydrate NiNO₃·6H₂O

Nickel oxide nanoparticles NiOx NPs

Open-circuit voltage Voc

Optical band gap between HOMO and LUMO E_{opt}

Organic light emitting diodes OLEDs

Organic solar cells OSCs

Organic thermoelectrics OTEs

Path length L_{PL}

Perovskite solar cells PSCs

Perylenediimides PDI

Phenethylammonium iodide PEAI

Phenyl-C61-butyric acid methyl ester PCBM

Photoexcited carrier concentration n

Poly(2,5-bis(3-alkylthiophen-2-yl)thieno[3,2-b]thiophene) PBTTT

Polyisobutylene PIB

Power conversion efficiency PCE

quasi-Fermi level splitting QFLS

Resistance

Scanning electron microscopy SEM

Self-assembled monolayers SAMs

Short-circuit current density Jsc

Silicon

Silver	Ag
Singly occupied molecular orbital	SOMO
Sodium hydroxide	NaOH
Solution concentration	C_{soln}
Stabilise and Pulse	SaP
Temperature	Т
Time	t
Time-resolved photoluminescence	TRPL
Tin oxide	SnO_2
Titanium dioxide	TiO_2
Transmittance	Tran
Transparent conductive oxide	TCO
Ultraviolet photoelectron spectroscopy	UPS
Voltage	V
Voltage at maximum power	V_{max}
Wavelength	λ
Work function of electron transport layer	W_{ETL}
Work function of hole transport layer	W_{HTL}
X-ray diffraction	XRD
X-ray photoelectron spectroscopy	XPS

Lists of symbols

Absorption coefficient	3
Conductivity	σ
Constant of Auger recombination rate	\mathbf{k}_{A}
Constant of bimolecular rate	k_{B}
Constant of monomolecular trapping rate	k_{T}
Diffraction angle	Θ
Microseconds	μs
Migration rate	rm
Monomolecular trapping rate constant	\mathbf{k}_{T}
Nanoseconds	ns
Rate of bimolecular recombination	k_2
Rate of monomolecular recombination	k_1
Resistivity	ρ
Work functions of sample	$\phi_{\it sampl}$
Work functions of tip	$oldsymbol{\phi}_{tip}$

Chapter 1. Introduction

1.1. Overview of Solar Cells

Nowadays, global electricity generation has been heavily reliant on fossil fuels to meet increasing energy demands. However, greenhouse gases are produced by burning fossil fuels into the atmosphere, resulting in environmental challenges such as global warming and climate change. As a result, renewable energy technologies are becoming increasingly important as sustainable alternatives to conventional energy sources, offering potential solutions to the environmental crisis. 4,5

The sun is an abundant and inexhaustible source of energy, emitting approximately 4.3x10²⁰ J/hour on the Earth, far exceeding the total anneal energy demand.⁶ Because of its sustainability and eco-friendliness, solar energy has become a key focus in renewable energy sources. It can be converted into electricity through the photovoltaic effect in solar cells, a phenomenon discovered by Edmond Becquerel in 1800s.⁷ The creation of the first photovoltaic cell in 1883 marked the beginning of continuous advancements in solar energy technology.⁸

Solar cells have evolved significantly over the decades and are broadly categorised into three generations. First-generation technologies primarily include monocrystalline and polycrystalline silicon (Si), and gallium arsenide (GaAs).9 Second-generation cells features thin film technologies, such as amorphous silicon (a-Si), crystalline silicon (c-Si), copper indium gallium selenide (CIGS), cadmium telluride (CdTe), and cadmium sulfide (CdS).10 Third-generation, including perovskite solar cells (PSCs), organic solar cells (OSCs), and dye-sensitized solar cells (DSSCs) first reported in 2012,11 197712 and 199113 respectively, emerged later with significant innovations in thin film deposition and the incorporation of nanomaterials.14 Despite these advancements, the silicon-based solar cells continues to dominate the market, comprising ~ 90 % of the solar cell industry.15 The widespread adoption of third-generation solar technologies remains constrained by their performance stability.16 Overcoming these barriers requires focused research to improve photovoltaic efficiency, simplify production techniques, and reduce associated costs.17

1.2. The Emergence of Perovskite Solar Cells

Perovskite was first discovered by Gustav Rose in 1939 and named after Alekseevich Perovski. ¹⁸ In the 1990s, Mitzi and collaborators explored the optoelectronic properties of organic-inorganic perovskites, emphasising their strong excitonic behaviour and potential for optoelectronic applications. ^{19,20} Hybrid organic-inorganic perovskites have a crystal structure represented by ABX₃, as shown in Figure 1.1 (A: monovalent cation such as CH₃NH₃⁺, MA⁺, FA⁺ or Cs⁺; B: divalent cation such as Pb²⁺ or Sn²⁺ and X: halide anion such as I⁻, Br⁻ and Cl⁻. ²¹ These materials possess unique electronic properties. ^{21,22} These characteristics have positioned perovskites highly for high-efficiency solar cells. Since their breakthrough development in 2013, PSCs have demonstrated remarkable progress, making them comparable to traditional silicon-based solar cells, reaching power conversion efficiency (PCE) of 26.0 %. ^{23,24}

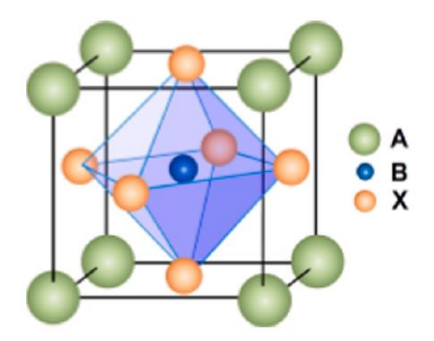


Figure 1.1. Structure of ABX₃ perovskites²⁵

1.3. Challenge of Perovskite Solar Cells

The development of inverted PSCs has been closely tied to advancements in electron acceptor materials. Traditionally, fullerene derivatives have been the preferred choices as electron transport material (ETM) due to their electron transport capabilities and compatibility with various organic solvents. However, their low intrinsic conductivity and complex synthesis have driven research into non-fullerene alternatives. Despite their versatility, organic semiconductors generally exhibit lower conductivity than inorganic materials due to inefficient charge transport mechanisms. Structural disorder in organic semiconductors further hinder performance. To address these challenges, molecular doping has been developed as a strategy to boost the conductivity of organic materials, improving their effectiveness in optoelectronic applications.

Beyond material selection, interfacial engineering is crucial for PSC performance. Self-assembled monolayers (SAMs) have been used as hole transport materials (HTMs) to improve charge extraction. Due to their dipole moment, SAMs can modify the structural energy level, enhancing charge collection and transport. However, the relationship between SAMs, energy level alignment, and overall PSC efficiency remains incompletely understood, requiring extensive studies of interfacial energy alignment in fully functional devices

1.4. Thesis Outline

This thesis investigates inverted PSCs, focusing on doping strategies and advanced charge transport materials:

- Chapter 2 introduces the foundational principles of PSCs, including their structure, operational mechanisms, and role of charge transport layers.
- Chapter 3 outlines the experimental sections in material and device analysis.
- Chapter 4 and 5 explore n-type doping of bisflavin and NDI derivatives as ETMs, examining how variation in side-chains influence doping reactions, doping mechanism, charge transfer, and conductivity.
- Chapter 6 focuses on the effect of SAMs on the performance of inverted PSCs, analysing how interfacial energetic influence device efficiency.
- Chapter 7 summarises the findings and suggests future direction for the study.

1.5. References

- 1 F. Rizzi, N. J. van Eck and M. Frey, *Renew Energy*, 2014, **62**, 657–671.
- 2 S. Manish, I. R. Pillai and R. Banerjee, *Energy for Sustainable Development*, 2006, **10**, 25–36.
- 3 E. Vine, *Energy Effic*, 2008, **1**, 49–63.
- 4 W. G. Santika, M. Anisuzzaman, P. A. Bahri, G. M. Shafiullah, G. V. Rupf and T. Urmee, Energy Res Soc Sci, 2019, **50**, 201–214.
- N. A. Ludin, N. I. Mustafa, M. M. Hanafiah, M. A. Ibrahim, M. Asri Mat Teridi, S. Sepeai, A. Zaharim and K. Sopian, *Renewable and Sustainable Energy Reviews*, 2018, **96**, 11–28.
- 6 N. S. Lewis and D. G. Nocera, *Proc Natl Acad Sci U S A*, 2006, **103**, 15729–15735.
- 7 E. Becquerel, Comptes Rendus, 1839, **9**, 561–567.
- 8 C. E. Fritts, *Am J Sci*, 1883, **s3-26**, 465–472.
- 9 J. Pastuszak and P. Węgierek, *Materials, Vol. 15, Page 5542*, 2022, **15**, 5542.
- 10 K. D. G. I. Jayawardena, L. J. Rozanski, C. A. Mills, M. J. Beliatis, N. A. Nismy and S. R. P. Silva, *Nanoscale*, 2013, **5**, 8411–8427.
- M. M. Lee, J. Teuscher, T. Miyasaka, T. N. Murakami and H. J. Snaith, *Science*, 2012,
 338, 643–647.
- 12 C. K. Chiang, C. R. Fincher, Y. W. Park, A. J. Heeger, H. Shirakawa, E. J. Louis, S. C. Gau and A. G. MacDiarmid, *Phys Rev Lett*, 1977, **39**, 1098–1101.
- 13 B. O'Regan and M. Grätzel, *Nature*, 1991, **353**, 737–740.
- 14 G. Conibeer, *Materials Today*, 2007, **10**, 42–50.
- 15 P. G. V. Sampaio and M. O. A. González, *Renewable and Sustainable Energy Reviews*, 2017, **74**, 590–601.
- 16 N. Shah, A. A. Shah, P. K. Leung, S. Khan, K. Sun, X. Zhu and Q. Liao, *Processes 2023, Vol. 11, Page 1852*, 2023, **11**, 1852.
- 17 N. Shah, A. A. Shah, P. K. Leung, S. Khan, K. Sun, X. Zhu, Q. A. Liao, N. Shah, A. A. Shah, P. K. Leung, S. Khan, K. Sun, X. Zhu and Q. Liao, *Processes 2023, Vol. 11, Page 1852*, 2023, **11**, 1852.
- 18 A. Miyata, A. Mitioglu, P. Plochocka, O. Portugall, J. T. W. Wang, S. D. Stranks, H. J. Snaith and R. J. Nicholas, *Nat Phys*, 2015, **11**, 582–587.
- 19 D. B. Mitzi, S. Wang, C. A. Feild, C. A. Chess and A. M. Guloy, *Science*, 1995, **267**,

- 1473–1476.
- 20 D. B. Mitzi, K. Chondroudis and C. R. Kagan, *IBM J Res Dev*, 2001, **45**, 29–45.
- 21 X. Yin, Z. Song, Z. Li and W. Tang, *Energy Environ Sci*, 2020, **13**, 4057–4086.
- 22 P. Roy, N. Kumar Sinha, S. Tiwari and A. Khare, *Solar Energy*, 2020, **198**, 665–688.
- 23 J. Park, J. Kim, H. S. Yun, M. J. Paik, E. Noh, H. J. Mun, M. G. Kim, T. J. Shin and S. Il Seok, *Nature*, 2023, **616**, 724–730.
- 24 Y. Zhao, F. Ma, Z. Qu, S. Yu, T. Shen, H. X. Deng, X. Chu, X. Peng, Y. Yuan, X. Zhang and J. You, *Science*, 2022, **377**, 531–534.
- 25 H. S. Kim, S. H. Im and N. G. Park, *J. Phys. Chem. C*, 2014, **118**, 5615–5625.
- 26 R. Sandoval-Torrientes, J. Pascual, I. García-Benito, S. Collavini, I. Kosta, T.-Z. Ramón,
 N. Martín and J. Luis Delgado, *Chem Sus Chem*, 2017, **10**, 2023–2029.
- 27 F. Zhang, W. Shi, J. Luo, N. Pellet, C. Yi, X. Li, X. Zhao, T. J. S. Dennis, X. Li, S. Wang, Y. Xiao, S. M. Zakeeruddin, D. Bi and M. Grätzel, *Adv. Mater.*, 2017, **29**, 1606806.
- 28 D. Wang, T. Ye and Y. Zhang, *J. Mater. Chem. A*, 2020, **8**, 20819–20848.
- 29 Y. C. Wang, X. Li, L. Zhu, X. Liu, W. Zhang and J. Fang, *Adv Energy Mater*, 2017, **7**, 1701144.
- 30 L. Hu, T. Liu, J. Duan, X. Ma, C. Ge, Y. Jiang, F. Qin, S. Xiong, F. Jiang, B. Hu, X. Gao, Y. Yi, Y. Zhou, L. Hu, T. F. Liu, J. S. Duan, Y. Y. Jiang, F. Qin, S. X. Xiong, F. Y. Jiang, B. Hu, Y. H. Zhou, X. Y. Ma, Y. P. Yi, C. W. Ge and X. K. Gao, *Adv Funct Mater*, 2017, 27, 1703254.
- Z. Wang, D. P. McMeekin, N. Sakai, S. van Reenen, K. Wojciechowski, J. B. Patel, M. B. Johnston, H. J. Snaith, Z. Wang, D. P. McMeekin, N. Sakai, S. van Reenen, K. Wojciechowski, J. B. Patel, M. B. Johnston and H. J. Snaith, *Adv. Mater.*, 2017, 29, 1604186.
- 32 I. E. Jacobs and A. J. Moulé, *Adv. Mater.*, 2017, **29**, 1703063.

Chapter 2. Technical Background

2.1. Perovskite Solar Cell Structure and Operation

Perovskite solar cells (PSCs) consist of following components: i) a transparent conductive oxide (TCO); ii) charge transport layers); iii) a perovskite layer and iv) a metal electrode. The charge transport layers, including electron and hole transport layers (ETL and HTL), are essential for efficiency of the devices. The ETL and HTL collect and transfer electrons and holes from the perovskite layer to the anode and cathode, respectively.

PSCs are generally fabricated in two distinct configurations, as shown in Figure 2.1: the regular and inverted PSCs structures. The regular architecture has achieved impressive power conversion efficiencies (PCEs), with reported values as high as to 25.7%.^{2,3} Titanium dioxide (TiO₂) or tin oxide (SnO₂) are commonly ETLs in this design, while spiro-OMeTAD is often employed as the HTL. However, the hygroscopic nature of ionically doped spiro-OMeTAD accelerates device degradation in humid environments. 43 Additionally, high temperature sintering is required to prepare metal oxide, which limits the use of polymer and flexible substrates, posing a challenge for the broader commercialization of PSC technology.4

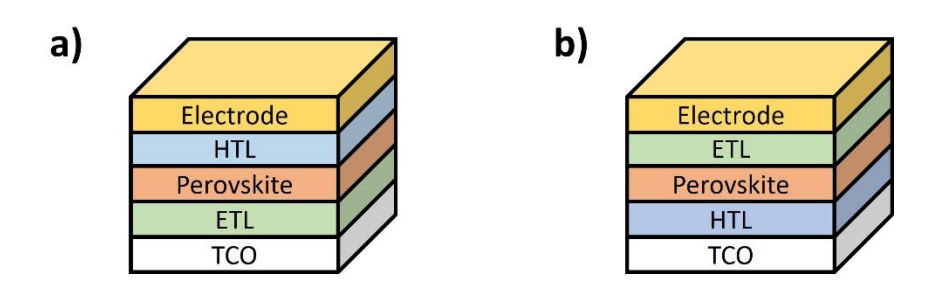
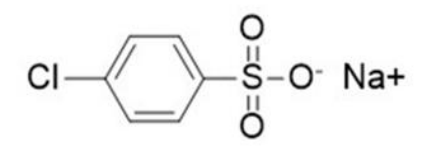


Figure 2.1. The architecture of a) regular and b) inverted PSCs

In 2024, inverted PSCs achieved a PCE of 26.15%, surpassing the performance of regular PSCs for the first time. 5 This breakthrough was driven by optimisation through the use of 4Cl-BZS ligands (Figure 2.2a) between the perovskite and the ETL (C_{60}). These ligands aligned in a planar orientation relative to the perovskite surface, effectively reducing surface defect density and minimising the energy misalignment at the interface. This strategy enhanced device performance to level comparable to regular PSCs.

a)



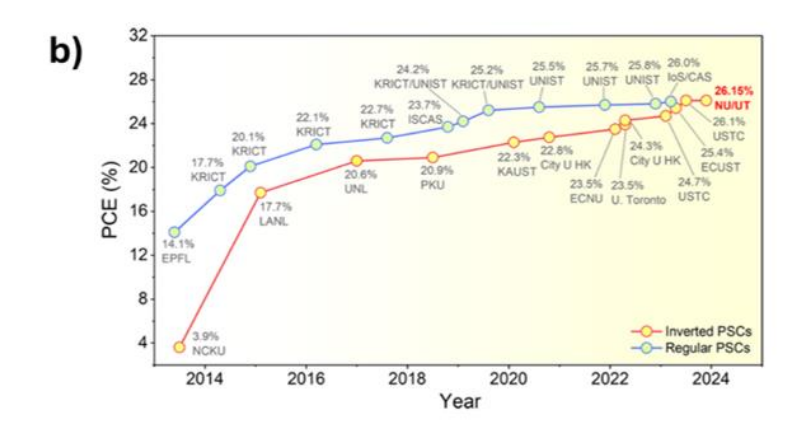


Figure 2.2. a) Structure of 4Cl-BZS ligand and b) Record of PCEs of inverted and regular PSCs⁶

The working principles of PSCs are illustrated in Figure 2.3. When a PSC absorbs photons from incident light, excited electrons in the perovskite layer are transferred from the valence band to the conduction band, resulting in the generation of excitons. Due to the material's high exciton diffusion length and low binding energy, these excitons can dissociate into free charge carriers. The electrons and holes are transported through the ETL and HTL to the anode and cathode, respectively. This charge separation generates an electric current, ultimately producing electricity.^{7,8}

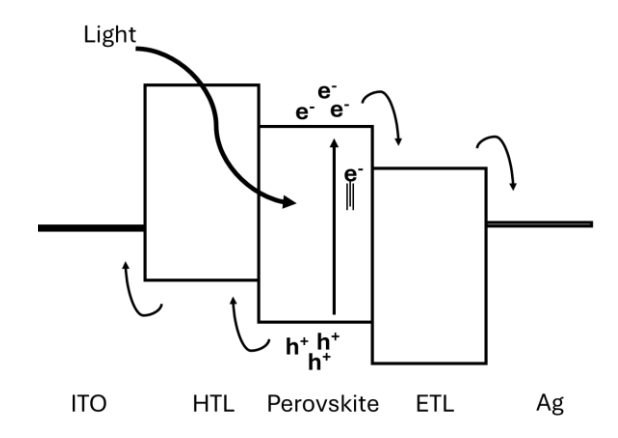


Figure 2.3. Working principle of in inverted PSC

The performance of PSCs is primarily evaluated by three key parameters: open-circuit voltage (Voc), short-circuit current density (Jsc), and fill factor (FF). These parameters are used to calculate the PCE, which measures the effectiveness of the solar cell. Figure 2.4 depicts typical current-voltage (J-V) characteristic for solar cells.

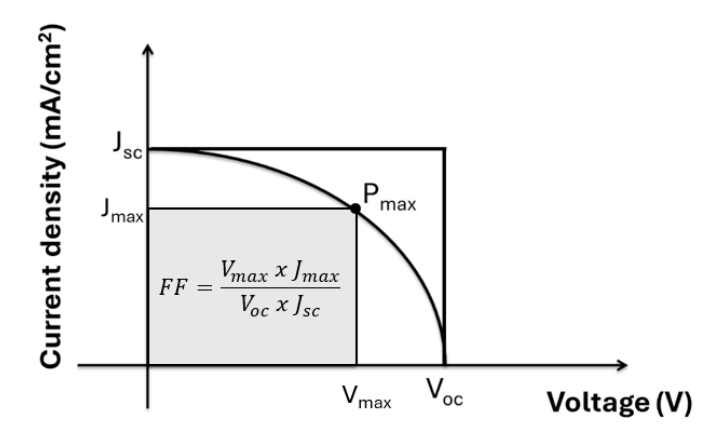


Figure 2.4. Typical J-V characteristic of photovoltaic device

The Voc represents the maximum voltage that a solar cell can deliver when no current flows through the external circuit. In PSCs, Voc is influenced by the level of non-radiative recombination within the device. It is determined by the quasi-Fermi level splitting (QFLS) divided by the elementary charge of devices. The Jsc corresponds to the current density at zero voltage when the external circuit is short. Jsc is primarily dictated by the optical properties of the solar cells, including light absorption and reflection characteristics of the material. The FF is the ratio of the maximum power output to the product of Voc and Jsc. It measures the efficiency of charge transport and recombination, providing insight into performance losses. It reflects the "squareness" of the J-V curve and is calculated as following equation. The theoretical upper limit for FF is approximately 90%.

$$FF = \frac{P_{max}}{V_{oc} \times J_{sc}} = \frac{V_{max} \times J_{max}}{V_{oc} \times J_{sc}}$$

Where:

P_{max} is the maximum output power.

 J_{max} and V_{max} are the current and voltage at maximum power, respectively.

The PCE represents the overall performance of the solar cell. It is defined as the ratio of the maximum power to the input power from the solar simulation.¹¹

$$PCE = \frac{P_{max}}{P_{in}} = \frac{V_{max} \times J_{max}}{P_{in}} = \frac{V_{oc} \times J_{sc} \times FF}{P_{in}}$$

Where:

P_{in} is the incident power.

In general, the presence of mobile ions in hybrid perovskite semiconductors causes the performance of PSCs to fluctuate over time in response to changes in operating conditions. This phenomenon, known as hysteresis, implies that the conventional diode equivalent circuit model, widely used to describe other solar cell applications, is not suitable to applied for PSCs. D. Moia *et al.* proposed that the interfaces in PSCs behave similarly to bipolar transistors, where electronic energy barriers for charge injection and recombination are dynamically modulated by the accumulation or depletion of ionic charge at the interfaces, as illustrated in Figure 2.5. In this model, R_{ion} represents an equivalent series resistance associated with ion migration, further influencing charge transport and recombination dynamics in PSCs.¹²

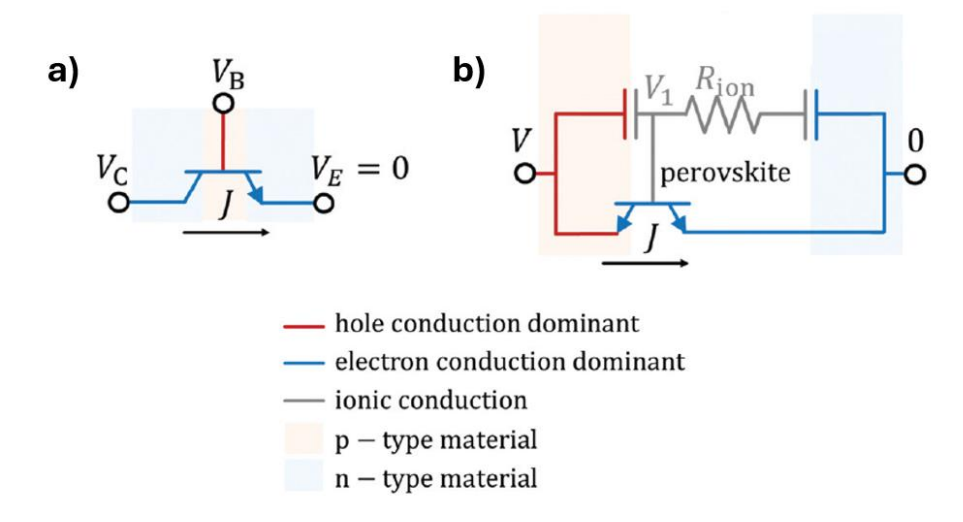


Figure 2.5. Device circuit models of a) bipolar transistor, V_c , V_B and V_E represent to the electrical potentials on collector, base and emitter terminals, respectively; and b) perovskite solar cell¹²

2.2. Compositional Flexibility of Perovskite Materials

The compositional modification of perovskite materials enables the fabrication of stable devices with enhanced optoelectronic properties. 13 Mono-cation perovskite composition currently exhibited thermal and structural instability to motivate the development of multiple halide composition to achieve excellent performance. 13 The energy levels of perovskite materials depend mainly on the cation B and the anion X. 13 The bandgap and optoelectronic properties of the perovskite depend on the valence band edge, which originates from the anti-bonding coupling between the Pb 6s orbital and the I 5p orbital, while the conduction band edge arises from the bonding orbitals of Pb 6p and I 5p, 14 as illustrated in Figure 2.6. Moreover, cation A play an indirect role by influencing the bandgap and the bond angles between cation B and anion X. This effect alters the arrangement of the surrounding BX_6^{4+} , promoting a more uniform orbital distribution and improved crystal symmetry. 15 For example, studies have shown the FAPbI $_3$ has a bandgap of 1.45 eV, while MAPbI $_3$ exhibits a slightly larger bandgap of at 1.52 eV, which is attributed to the smaller size of MA $^+$ cation. 16 In contrast, replacing MA $^+$ with Cs $^+$ increases the bandgap to 1.73 eV. 17

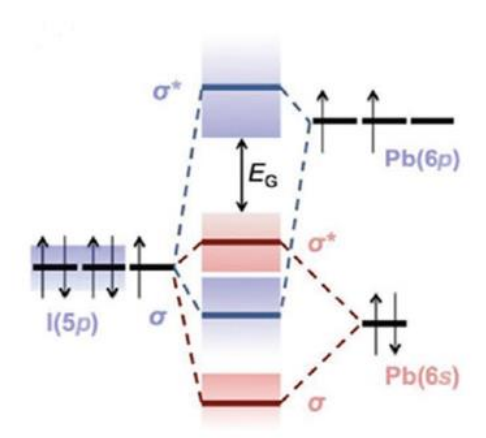


Figure 2.6. Schematic diagram of the formation of bonding and anti-bonding orbitals in perovskite due to hybridization of Pb and I atomic orbitals¹⁸

Under the light illumination and an applied E-field, mobile charged ions in the perovskite can generate vacancies or defects in the crystal structure, leading to hysteresis in JV characteristic curves and device degradation. Its migration rate (r_m) can be evaluated by the equation:¹⁵

$$r_m \propto exp \frac{E_a}{k_B T}$$

Where:

E_a is the activation energy

k_B is the Boltzmann constant

T is the temperature

The migration energy of ionic vacancies depends on the Coulomb interactions of the crystal lattice. By introducing cations of varying sizes, the Ea of ion migration can be adjusted, which suppresses ionic motion and enhances device stability.

The size mismatch of monovalent cations A introduces localised lattice distortions that act as a steric impediment effect to inhibit the ion migration. This effect improves device stability by increasing the energy barrier for ion movement. Tan *et al.* investigated the effect of replacing MA⁺ with acetamidinium (Ace⁺) and performed DFT calculations to simulate iodide ion migration pathways and activation energies within the perovskite lattice, as depicted in Figure 2.7.¹⁹ The Ea for ion migration in MAPbl₃ is 0.40 V, while it increases to 0.63 V in Ace_{0.25}MA_{0.75}Pbl₃. This increase is attributed to the steric hindrance induced by the size mismatch between Ace⁺ (ionic radius: 0.277 nm) and MA⁺ (ionic radius: 0.217 nm), which cause lattice distortions. Their DFT results demonstrated that iodide ions follow a more complex, roundabout migration path in Ace_{0.25}MA_{0.75}Pbl₃ compared to the straightforward path observed in MAPbl₃, as illustrated in Figure 2.7b and 2.7d.

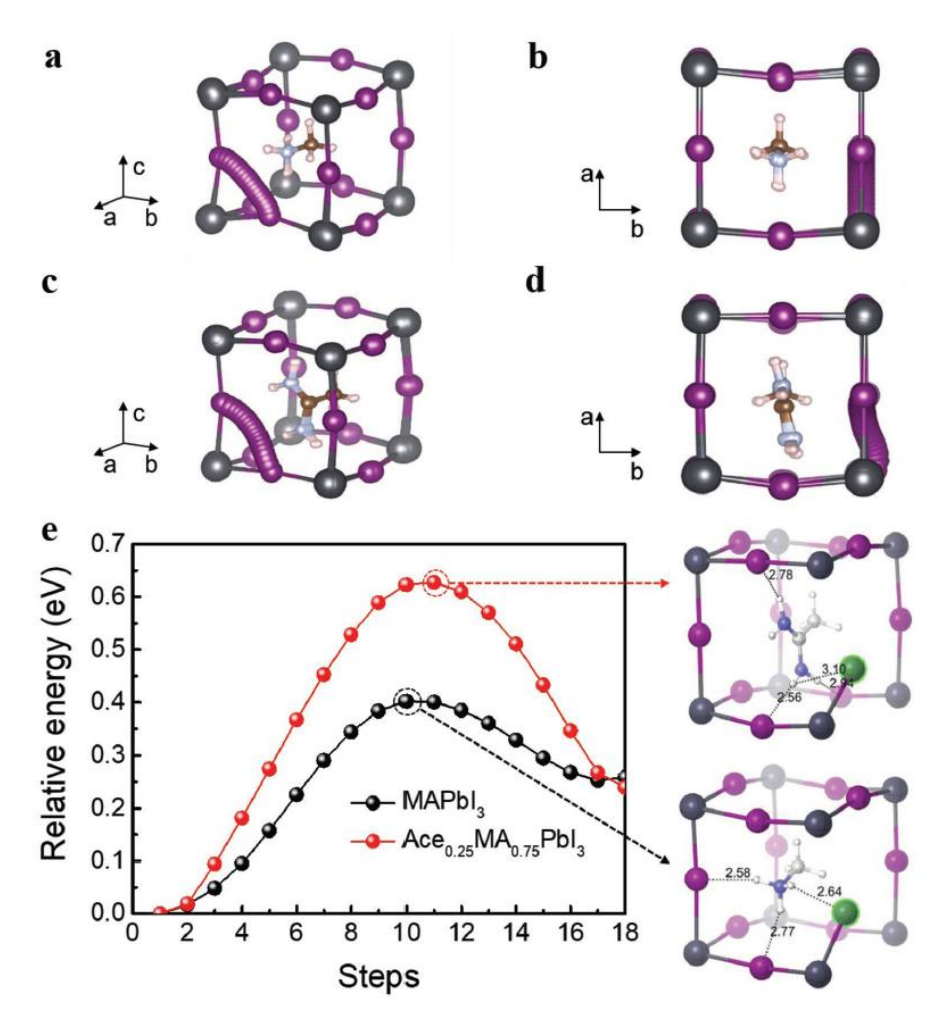


Figure 2.7. a) Side view and b) top view of the I⁻ migration path for MAPbI₃; c) side view and d) top view for Ace_{0.25}MA_{0.75}PbI₃ perovskite and e) activation energies for iodide ion migration in MAPbI₃ and Ace_{0.25}MA_{0.75}PbI₃ systems, showing the maximum energy states associated with the hydrogen bond length between the migrating iodide ion and the nearest neighboring hydrogen atom¹⁹

To further validate these findings, temperature dependent conductivity measurements were conducted on MAPbI₃ and Ace_{0.25}MA_{0.75}PbI₃ to obtain the ion migration activation energy. ¹⁹ Activation energy (Ea) can be determined by the equation:

$$\sigma(T) = \frac{\sigma_0}{T} \exp\left(\frac{-E_a}{k_b T}\right)$$

Where:

 $\sigma(T)$ is the conductivity as a function of temperature $\sigma_{\scriptscriptstyle 0}$ is a constant

It found out that Ea proportional to the mismatch in size of A site cation, showing increased energy barrier for ion migration of mixed cation perovskites compared to single cation perovskite in Figure 2.8.

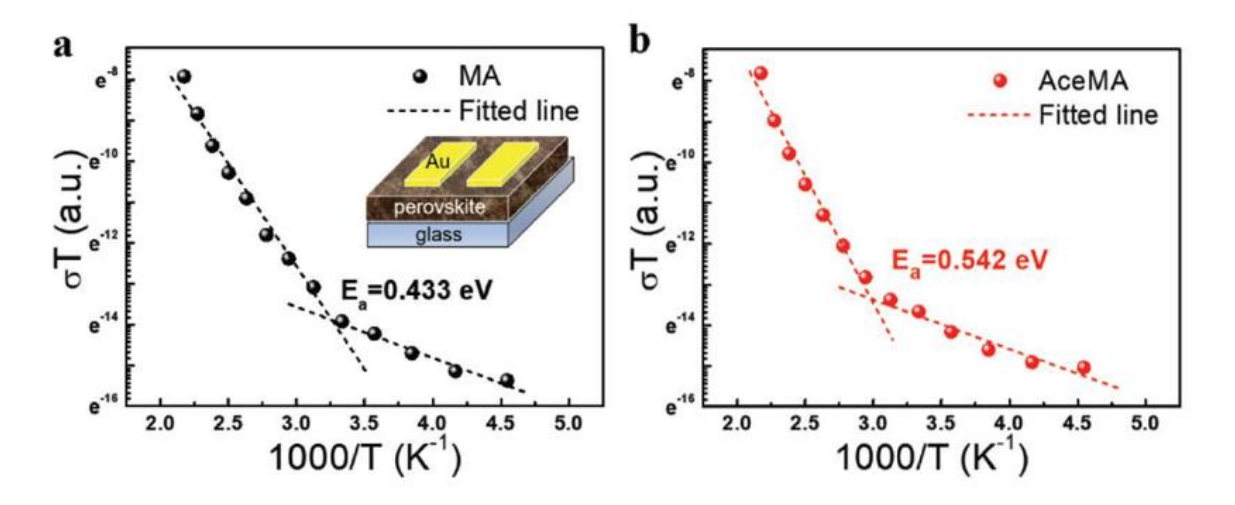


Figure 2.8. Temperature dependent conductivity measurements of the a) MAPbI₃ and b) $Ace_{0.25}MA_{0.75}PbI_3 \ devices^{19}$

2.3. Determination of Device Energetics

To assess the energetic alignment with a device, various characterization techniques are employed, including X-ray photoelectron spectroscopy (XPS), ultraviolet photoelectron spectroscopy (UPS) and kelvin probe force microscopy (KPFM). XPS and UPS involve the irradiation of material with photons, leading to the ejection of photoelectrons *via* X-rays and ultraviolet light, respectively. While XPS primarily examines core level electrons, UPS focuses on valence band electrons. Both methods are instrumental in determining the material's work function. However, these techniques are typically applied to single layers in vacuum conditions, making them highly surface sensitive and less representative of the actual conditions within device structure.^{20,21} KPFM measures the contact potential difference (CPD) between a sample surface and a tip. However, it is surface sensitive and can be influenced by contaminants or surface molecules, potentially reducing both accuracy and reproducibility.²² Due to these limitations, alternative methods are explored for device energetics analysis.

Due to these measurements being so sensitive they are often done on single layers and therefore are not representative of a full working device. To fully probe device energetics a recently developed method coined the Stabilise and Pulse (SaP) technique can be employed. The SaP utilises rapid voltage pulses to determine the built-in potential within a working device. This method is effective for studying band offsets in PSCs, which directly influence charge extraction efficiency and the electrostatic potential drop within the device. The electrostatic potential drop, $\Delta \varphi_{PVK}$, is calculated as:²³

$$\Delta \varphi_{PVK} = W_{HTL} - W_{ETL}$$

Where:

W_{HTL} is the work function of HTL

W_{ETL} is the work function of ETL

This technique utilises the accumulation of ionic charge at device interfaces to extract flat band condition of the perovskite (V_{flat}).²⁴ At the equilibrium of short circuit conditions (Figure 2.9a), the Fermi level of the ETL, perovskite and HTL are aligned, generating an internal electric field within the perovskite layer. Anions and cations drift along this electric field, resulting in the accumulation of anions at the ETL/perovskite interface and cations at the perovskite/HTL interface (Figure 2.9b). Upon light illumination, holes and electrons are generated within the perovskite layer and transported to ETL and HTL due to energy alignment. Consequently, the ETL and HTL become filled with electrons and holes, respectively. This alters the direction of internal electric field in the perovskite layer, causing anions to migrate from ETL/perovskite interface to perovskite/HTL interface, and cations to move in opposite side (Figure 2.9c). Under open circuit condition with light illumination, the accumulation of anions and cations is observed at the interface of perovskite/HTL and ETL/perovskite (Figure 2.9d). The V_{flat} refers to the state at which ions are uniformly distributed throughout the perovskite layer during illumination. This is related to the Fermi level difference between charge transport layers (HTL and ETL) and is critical for achieving the highest Jsc. This approach is particularly valuable for understanding how ion accumulation at the interface affects charge extraction and recombination processes.²⁹ A simulation of iodide vacancy cation distribution is illustrated in Figure 2.10,23 showing the distribution of cations under different stabilising voltages, simulating at short circuit (low stabilisation

voltages) and open circuit conditions (high stabilisation voltages). It demonstrates that the cations accumulate at the perovskite/HTL interface under short circuit condition, and drift toward the ETL/perovskite interface under open circuit conditions upon light illumination.

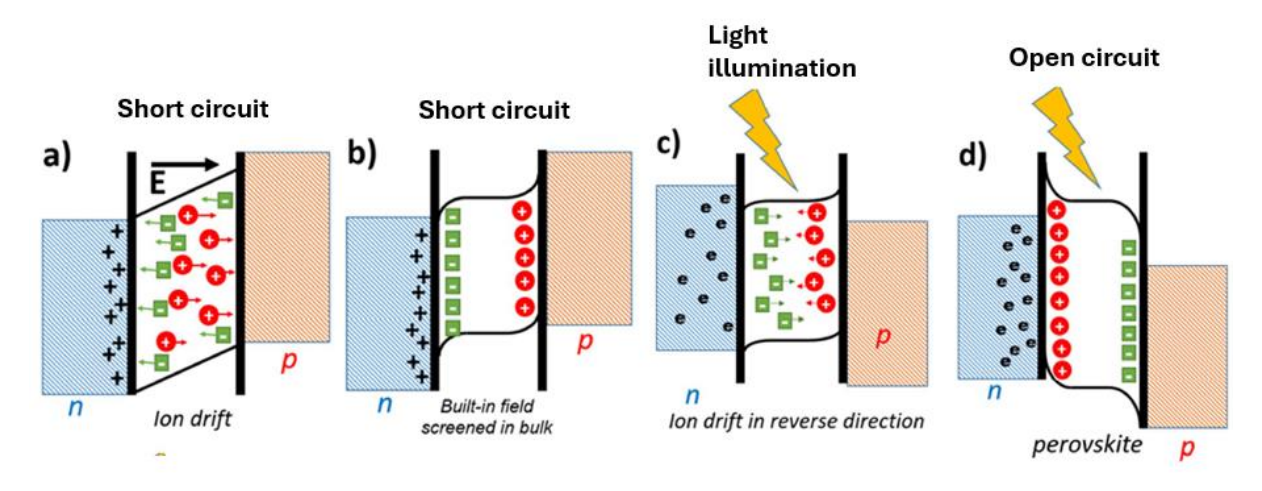


Figure 2.9. Band diagrams of mobile ions of solar cell at a) after contact; b) in equilibrium in dark condition; c) after light illumination and d) in equilibrium under light illumination²⁵

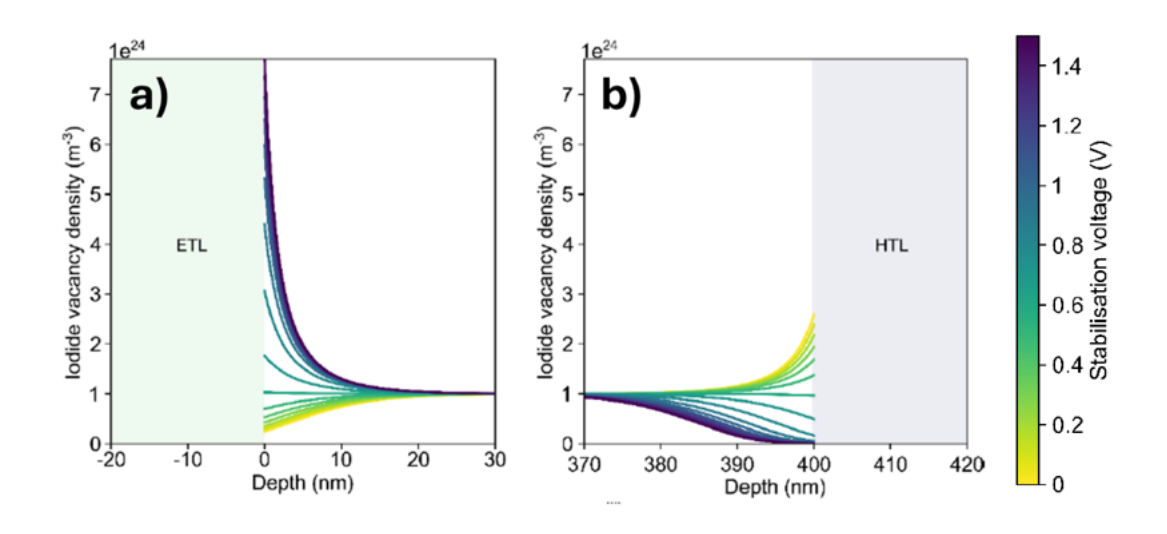


Figure 2.10. Simulation for vacancy density distribution of iodide at the interface between a) ETL/perovskite and b) perovskite/HTL (stabilisation voltages between 0 and $1.5\,\rm V)^{23}$

A major challenge in studying PSC energetics is decoupling ionic and electronic effects. Iodide vacancies, with their relatively low activation energy, migrate under an applied electric field and alter the devices' internal electric field distribution. ²⁶ Other ionic species, such as MA+, typically exhibit slower migration rates ^{26,27} and minimal impact due to their lower concentration. ²⁸ To isolate ionic effects, SaP measurements involve preconditioning the device at a stabilization voltage for a specific duration, allowing ionic vacancies to reach a steady-state distribution. A short voltage pulse is then applied, enabling charge extraction without significant ionic movement. ^{23,27} This approach ensures that ionic positions remain static during the measurement, while electronic effects are captured.

2.4. Advancements in Non-Fullerene Organic Electron Transport Materials

In PSC architecture, the perovskite absorber is typically placed between HTL and ETL. The perovskite layer generates charge carriers upon absorbing light, and HTL and ETL are responsible for transporting and collecting these carriers at the electrodes. ²⁹ Efficient transport and extraction are essential for achieving high PCE, making the development of suitable charge transport materials for PSCs critical. The goal is to enhance charge extraction and minimise recombination losses. ^{30,31}

A variety of HTL materials have been reported in PSCs including Spiro-OMeTAD,³² PTAA,³³ PEDOT:PSS³⁴ and SAMs^{35,36} on their evolution and superior photovoltaic performances. However, compared with HTMs, the development of ETMs is still not mature enough. Fullerene materials, such as C₆₀ and PCBM, are commonly used as organic ETLs in PSCs due to their electron conductivity and solubility in organic solvents compatible with solution processing,^{37–39} reaching up a PCE of 26.15% in 2024.⁵ Compared to inorganic ETMs (such as TiO₂), fullerene ETMs can be processed using low-temperature solution method, and exhibit faster photoluminescence decay than TiO₂ between perovskite layer and ETLs, indicating faster charge transfer rate.^{40,41}

Despite being widely explored, fullerene-based ETLs have limitations for long term stability. Photo-induced dimerization can occur in fullerene film upon exposure to light ⁴²⁻ resulting in in reduced charge collection efficiency, lower carrier mobility due to

energetic traps^{46–48} and losses in Jsc and FF.⁴⁹ Fullerene-based ETLs also face challenges related to the formation of undesired isomers during synthesis,⁵⁰ which necessitates purification procedures and increases production costs.^{51–53} For the optoelectronic properties, fullerene materials exhibit relatively low conductivity in their pristine form (10⁻⁸ S/cm), which remains less competitive compared to inorganic ETMs such as TiO₂ and SnO₂ (10⁻³ to 10⁻⁴S/cm).⁵⁴ These challenges have spurred research into non-fullerene-based organic electron transport materials in photovoltaic aspects.

In the quest for alternatives to fullerene based ETMs, researchers have explored a diverse range of non-fullerene-organic ETMs. To design an efficient new type ETMs, the materials should meet the requirements as follows: i) high solubility in an orthogonal solvent, which is different solvent with the solvent of perovskite fabrication; ii) good mobility and conductivity to improve the charge transport and lower Rs; iii) easy to deposit on the perovskite layer *via* simple method eg spin-coating, avoiding shunt path formation between the electrode and perovskite layer; and iv) optimal energy levels with perovskite layer. The LUMO/HOMO of an ETL should be lower/higher than the conduction/valence bands of perovskite layer, aiming to reduce the Voc loss and enhancing electron extraction. 55 Non-fullerene ETLs are promising alternatives due to their tuneable electronic and optical properties, 56,57 simpler synthesis. 58-61



Figure 2.11. Structures of a) PCBM; b) flavin and c) naphthalene diimide (NDI)

Researchers have increasingly focused on green chemistry, aiming to develop cleaner synthetic procedures that are less harmful to human and the environment. ⁶² One promising approach involves utilising biological inspired systems and materials as an

alternatives for solar cell applications, emphasising the use of relatively non-toxic chemicals and naturally derived precursors. Flavins, a class of biological electron-transporting molecules, are particularly well-studied for this purpose. Flavins are naturally occurring redox-active compounds, and their synthetic analogues offer exciting potential as new ETMs for photovoltaics. These molecules can be conveniently synthesised from inexpensive precursors, exhibit inherent stability, and allow for straightforward electronic tuning through synthetic manipulation. He altering the phenyl ring at position C(6)-C(9) and functionalising the N(3) and N(10) positions, flavin derivatives can be tailored for specific optical, redox, and solubility properties. Due to their versatility, flavin derivatives have found applications in fluorescent probes hotocatalysts and energy storage devices such as batteries. Photocatalysts and energy storage devices such as batteries. Despite the ease with which flavin properties can be precisely tuned, it is surprising that their potential in photovoltaics has received relatively little attention. Given their favorable electron characteristics and structural adaptability, flavin derivatives represent a promising yet underexplored class of materials for the efficient, sustainable solar energy technologies.

Molecules featuring naphthalene diimide (NDI) core are one of the most promising candidates for non-fullerene ETMs in optoelectronic applications⁷²⁻⁷⁴ due to simple synthesis and tuneable energy levels. 75,76 These features reduce chemical use, energy consumption, cost, and production time. However, NDIs-based materials face challenges with poor solubility in organic solvents, resulting in poor film morphology and an increased density of defects. 76,77 These defects can cause the trapping sites for charge carriers, hindering efficient charge transport. 78,79 The solubility issue of NDI-based molecules can be addressed by synthetically modifying the imide or naphthalene unit side-chains, which do not require complicated synthesis procedures. 75,80 NDI derivatives benefit from side-chain modifications to reduce stacking issues. For examples, the Nsubstituted phenylmethyl derivative NDI-PM improved electron mobility, solubility, and thermal stability, achieving PCEs competitive with PCBM-based devices due to stronger hydrogen bonding.81 Further, adding asymmetric groups chiral (R)-1-phenylethyl (PhE) in NDI-PM to form NDI-PhE, enhanced solubility and film formation, resulting in PCEs up to 20.5 %, offering competitive photovoltaic performance compared to PCBM-based PSCs.⁸² Side-substituted NDIs, like those with thiophene groups (DS1 and DS2), have

been effective in passivating surface traps on the perovskite layer, further enhancing device performance.^{83–86} With continued advancements and design modifications, NDI derivatives hold great potential as viable alternative to traditional inorganic metal oxides and fullerene derivatives in optoelectronic applications.

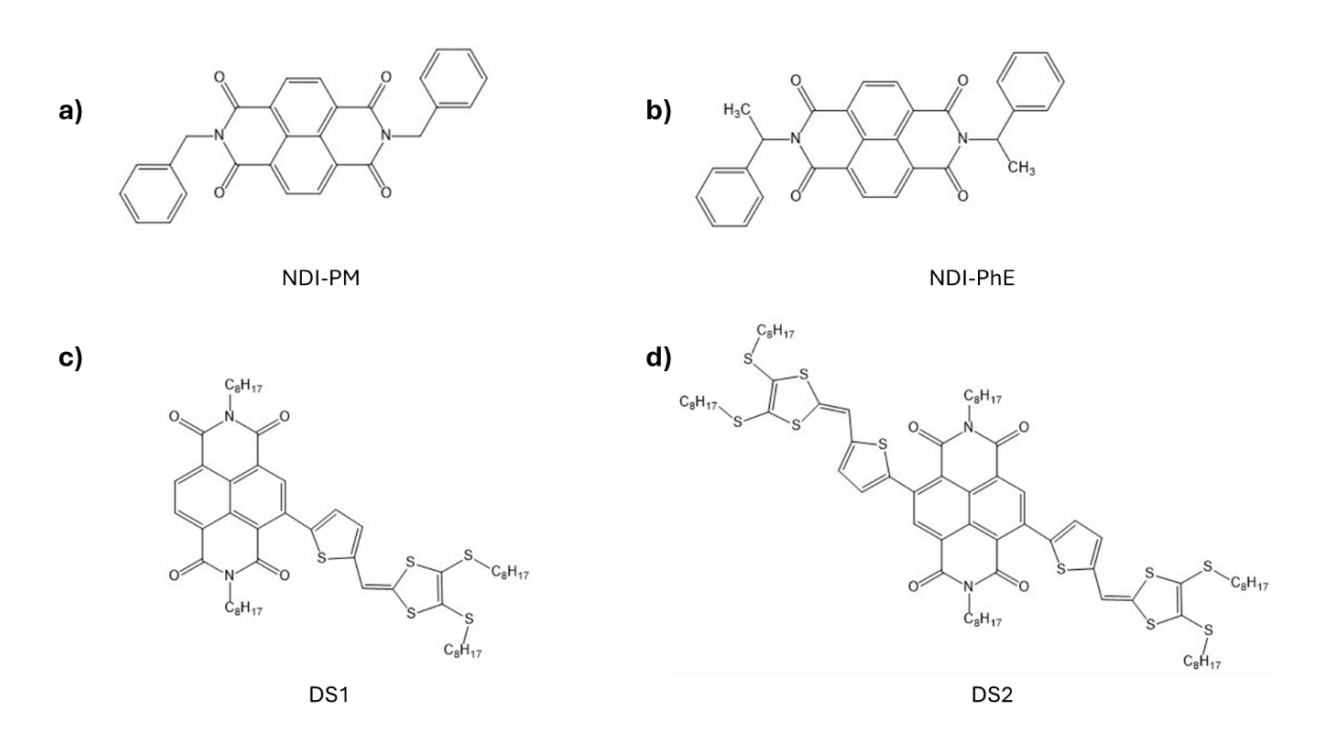


Figure 2.12. Structures of a) NDI-PM; b) NDI-PhE; c) DS1 and d) DS2

2.5. Enhancing Properties in Organic Electron Transport Materials Through n-type Doping

Due to the hopping charge transfer mechanism and trap site formation by disorder and impurities, most organic ETMs exhibit relatively low conductivity, (e.g. 10⁻⁸ S/cm for PCBM,⁸⁷ 10⁻⁴ S/cm for PDI⁸⁸ and 10⁻⁵ S/cm for NDI ⁷⁵) compared to inorganic ETMs. To address this, there has been increasing interest in doping organic semiconductor *via* the addition of dopants to enhance the material's properties. Doping involves the incorporation of external dopant into the host semiconductor to induce charge transfer between the dopant and host. The doping of organic semiconductors was started at 1970s,⁸⁹ and it is a strategy to enhance the conductivity of organic semiconductors by generating free charges through the charge transfer between the dopant and the host.⁹⁰ This process can modulate the charge transport characteristics of organic solar cells

(OSCs)^{91,92}, organic light emitting diodes (OLEDs)^{93,94} and organic thermoelectrics (OTEs).^{95,96}

In n-type doping of ETMs, molecular dopants donate electrons from their HOMO to the LUMO of the host materials. This process causes an upward shift in the Fermi level of the host materials. To optimise doping efficiency and facilitate charge transfer, the HOMO of n-type dopants must be shallower than the LUMO of the organic semiconductor (Figure 2.13).89 The electron transfer process during doping can occur through two primary mechanisms: (i) ion pair (IP) formation and (ii) charge transfer complex (CTC) formation.⁹⁷ In IP formation of n-type doping, an electron from the dopant is transferred to the organic semiconductors, resulting in the formation of a dopant cation and an organic semiconductor anion. 97,98 In contrast, CTC is formed through the hybridization of the molecular orbitals of the dopant and the organic semiconductor. 99 This hybridization generates a new set of occupied bonding orbitals from a donor and unoccupied antibonding orbitals from an acceptor. 97 Charge transfer occurs through the hybridized orbital to or from the host materials. However, due to strong binding energy, addition energy is required to overcome this binding energy to generate free charges. 97 Furthermore, free charge generation in CTC is less efficient due to energy level mismatch, causing low doping efficiency and conductivity.97

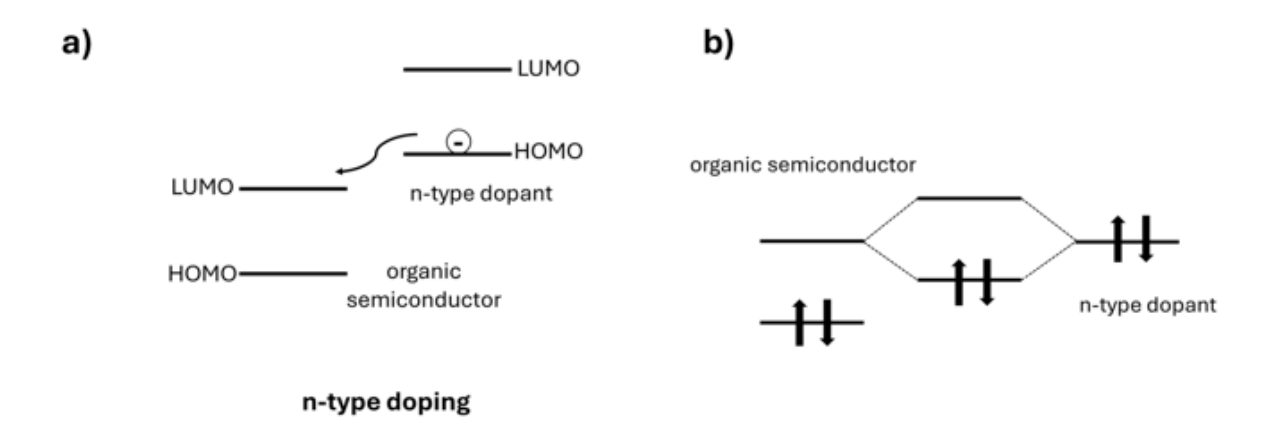


Figure 2.13. Doping mechanism of a) ion pair formation of n-type doping and b) CTC formation

Despite the promise of doping, its practical application in organic semiconductor is hindered by low doping efficiency, which arises from factors such as charge trap states, mismatched energy level alignment, strong Coulombic interactions within ion pairs, CTC formation, and dopant aggregation and degradation. Improving the electrical performance of doped organic semiconductors is crucial for enhancing their conductivity and mobility, which are essential for their advancement towards commercial applications.

2.6. References

- S. Bhattarai, A. Mhamdi, I. Hossain, Y. Raoui, R. Pandey, J. Madan, A. Bouazizi, M. Maiti, D. Gogoi and A. Sharma, *Micro and Nanostructures*, 2022, **172**, 207450.
- 2 Q. Wali, F. J. Iftikhar, M. E. Khan, A. Balilonda, M. Aamir, W. Fan and S. Yang, *J Mater Chem C*, 2022, **10**, 12908–12928.
- Z. Liang, Y. Zhang, H. Xu, W. Chen, B. Liu, J. Zhang, H. Zhang, Z. Wang, D. H. Kang, J. Zeng, X. Gao, Q. Wang, H. Hu, H. Zhou, X. Cai, X. Tian, P. Reiss, B. Xu, T. Kirchartz, Z. Xiao, S. Dai, N. G. Park, J. Ye and X. Pan, *Nature*, 2023, **624**, 557–563.
- 4 T. Leijtens, G. E. Eperon, S. Pathak, A. Abate, M. M. Lee and H. J. Snaith, *Nat Commun*, 2013, **4**, 2885.
- H. Chen, C. Liu, J. Xu, A. Maxwell, W. Zhou, Y. Yang, Q. Zhou, A. S. R. Bati, H. Wan, Z. Wang, L. Zeng, J. Wang, P. Serles, Y. Liu, S. Teale, Y. Liu, M. I. Saidaminov, M. Li, N. Rolston, S. Hoogland, T. Filleter, M. G. Kanatzidis, B. Chen, Z. Ning and E. H. Sargent, Science, 2024, 384, 189–193.
- 6 P. Chen, Y. Xiao, S. Li, X. Jia, D. Luo, W. Zhang, H. J. Snaith, Q. Gong and R. Zhu, *Chem Rev*, 2024, **124**, 10623–10700.
- P. Ghosh, S. Sundaram, T. P. Nixon and S. Krishnamurthy, *Encyclopedia of Smart Materials*, 2022, **2**, 646–660.
- 8 B. G. Krishna, D. S. Ghosh and S. Tiwari, *Chemistry of Inorganic Materials*, 2023, **1**, 100026.
- J. Warby, S. Shah, J. Thiesbrummel, E. Gutierrez-Partida, H. Lai, B. Alebachew, M. Grischek, F. Yang, F. Lang, S. Albrecht, F. Fu, D. Neher and M. Stolterfoht, *Adv Energy Mater*, 2023, **13**, 2303135.
- 10 S. Zouhair, B. Luo, D. Bogachuk, D. Martineau, L. Wagner, A. Chahboun, S. W. Glunz and A. Hinsch, *Solar RRL*, 2022, **6**, 2100745.
- 11 A. S. Al-Ezzi and M. N. M. Ansari, Applied System Innovation, 2022, 5, 67.
- D. Moia, I. Gelmetti, P. Calado, W. Fisher, M. Stringer, O. Game, Y. Hu, P. Docampo, D. Lidzey, E. Palomares, J. Nelson and P. R. F. Barnes, *Energy Environ Sci*, 2019, **12**, 1296–1308.
- 13 Q. Lin, D. J. Kubicki, M. K. Omrani, F. Alam and M. Abdi-Jalebi, *J. Mater. Chem. C*, 2023, **11**, 2449–2468.
- 14 J. Y. Kim, J. W. Lee, H. S. Jung, H. Shin and N. G. Park, *Chem Rev*, 2020, **120**, 7867–

7918.

- 15 J. W. Lee, S. Tan, S. Il Seok, Y. Yang and N. G. Park, *Science*, 2022, **375**, 6583
- 16 A. Mishra, M. A. Hope, M. Almalki, L. Pfeifer, S. M. Zakeeruddin, M. Grätzel and L. Emsley, J. Am. Chem. Soc., 2022, 144, 15175–15184.
- 17 Z. Liu, P. Liu, M. Li, T. He, T. Liu, L. Yu and M. Yuan, *Adv. Energy Mater.*, 2022, **12**, 2200111.
- 18 M. M. Byranvand, C. Otero-Martínez, J. Ye, W. Zuo, L. Manna, M. Saliba, R. L. Z. Hoye and L. Polavarapu, *Adv. Opt. Mater.*, 2022, **10**, 2200423.
- 19 S. Tan, I. Yavuz, N. De Marco, T. Huang, S. J. Lee, C. S. Choi, M. Wang, S. Nuryyeva, R. Wang, Y. Zhao, H. C. Wang, T. H. Han, B. Dunn, Y. Huang, J. W. Lee and Y. Yang, *Adv. Mater.*, 2020, 32, 1906995.
- 20 J. Endres, D. A. Egger, M. Kulbak, R. A. Kerner, L. Zhao, S. H. Silver, G. Hodes, B. P. Rand, D. Cahen, L. Kronik and A. Kahn, *J. Phys. Chem.Lett.*, 2016, **7**, 2722–2729.
- 21 T. S. Sherkar, C. Momblona, L. Gil-Escrig, J. Ávila, M. Sessolo, H. J. Bolink and L. J. A. Koster, *ACS Energy Lett*, 2017, **2**, 1214–1222.
- 22 C. S. Jiang, M. Yang, Y. Zhou, B. To, S. U. Nanayakkara, J. M. Luther, W. Zhou, J. J. Berry, J. Van De Lagemaat, N. P. Padture, K. Zhu and M. M. Al-Jassim, *Nat Commun*, 2015, 6, 8397.
- 23 N. S. Hill, M. V. Cowley, N. Gluck, M. H. Fsadni, W. Clarke, Y. Hu, M. J. Wolf, N. Healy, M. Freitag, T. J. Penfold, G. Richardson, A. B. Walker, P. J. Cameron and P. Docampo, *Adv Mater*, 2023, 35, 2302146.
- F. J. Angus, W. K. Yiu, H. Mo, T. L. Leung, M. U. Ali, Y. Li, J. Wang, Anita. W. Y. Ho-Baillie,
 G. Cooke, A. B. Djurišić and P. Docampo, *J Phys Chem Lett*, 2024, 15, 10686–10695.
- 25 F. Ebadi, M. Aryanpour, R. Mohammadpour and N. Taghavinia, *Sci Rep.*, 2019, **9**, 1–9.
- 26 C. Eames, J. M. Frost, P. R. F. Barnes, B. C. O'Regan, A. Walsh and M. S. Islam, *Nat Commun*, 2015, **6**, 7497.
- 27 K. Domanski, B. Roose, T. Matsui, M. Saliba, S. H. Turren-Cruz, J. P. Correa-Baena, C. R. Carmona, G. Richardson, J. M. Foster, F. De Angelis, J. M. Ball, A. Petrozza, N. Mine, M. K. Nazeeruddin, W. Tress, M. Grätzel, U. Steiner, A. Hagfeldt and A. Abate, *Energy Environ Sci*, 2017, **10**, 604–613.
- 28 C. Ding, R. Huang, C. Ahläng, J. Lin, L. Zhang, D. Zhang, Q. Luo, F. Li, R. Österbacka and C. Q. Ma, *J Mater Chem A*, 2021, **9**, 7575–7585.

- 29 H. S. Jung and N. G. Park, *Small*, 2015, **11**, 10–25.
- 30 B. G. Krishna, D. S. Ghosh and S. Tiwari, *Chemistry of Inorganic Materials*, 2023, **1**, 100026.
- 31 M. Cheng, C. Zuo, Y. Wu, Z. Li, B. Xu, Y. Hua and L. Ding, *Sci Bull (Beijing)*, 2020, **65**, 1237–1241.
- 32 U. Bach, D. Lupo, P. Comte, J. E. Moser, F. Weissörtel, J. Salbeck, H. Spreitzer and M. Grätzel, *Nature*, 1998, **395**, 583–585.
- 33 Q. Wang, C. Bi and J. Huang, *Nano Energy*, 2015, **15**, 275–280.
- 34 Y. Xia and S. Dai, *Journal of Materials Science: Materials in Electronics*, 2021, **32**, 12746–12757.
- S. Zhang, F. Ye, X. Wang, R. Chen, H. Zhang, L. Zhan, X. Jiang, Y. Li, X. Ji, S. Liu, M. Yu, F. Yu, Y. Zhang, R. Wu, Z. Liu, Z. Ning, D. Neher, L. Han, Y. Lin, H. Tian, W. Chen, M. Stolterfoht, L. Zhang, W. H. Zhu and Y. Wu, Science, 2023, 380, 404–409.
- 36 Z. R. Lan, J. Y. Shao and Y. W. Zhong, *Mol Syst Des Eng*, 2023, **8**, 1440–1455.
- 37 Y. C. Wang, X. Li, L. Zhu, X. Liu, W. Zhang and J. Fang, *Adv Energy Mater*, 2017, **7**, 1701144.
- 38 R. Sandoval-Torrientes, J. Pascual, I. García-Benito, S. Collavini, I. Kosta, R. Tena-Zaera, N. Martín and J. L. Delgado, *ChemSusChem*, 2017, **10**, 2023–2029.
- 39 F. Zhang, W. Shi, J. Luo, N. Pellet, C. Yi, X. Li, X. Zhao, T. J. S. Dennis, X. Li, S. Wang, Y. Xiao, S. M. Zakeeruddin, D. Bi and M. Grätzel, *Adv. Mater.*, 2017, **29**, 1606806.
- 40 J. H. Heo, H. J. Han, D. Kim, T. K. Ahn and S. H. Im, *Energy Environ Sci*, 2015, **8**, 1602–1608.
- 41 C. Tao, S. Neutzner, L. Colella, S. Marras, A. R. Srimath Kandada, M. Gandini, M. De Bastiani, G. Pace, L. Manna, M. Caironi, C. Bertarelli and A. Petrozza, *Energy Environ Sci*, 2015, **8**, 2365–2370.
- 42 P. C. Eklund, A. M. Rao, P. Zhou, Y. Wang and J. M. Holden, *Thin Solid Films*, 1995, **257**, 185–203.
- 43 A. Dzwilewski, T. Wågberg and L. Edman, *J Am Chem Soc*, 2009, **131**, 4006–4011.
- 44 B. C. Schroeder, Z. Li, M. A. Brady, G. C. Faria, R. S. Ashraf, C. J. Takacs, J. S. Cowart, D. T. Duong, K. H. Chiu, C. H. Tan, J. T. Cabral, A. Salleo, M. L. Chabinyc, J. R. Durrant and I. McCulloch, *Angewandte Chem Int Ed*, 2014, 53, 12870–12875.
- 45 A. M. Rao, P. Zhou, K. A. Wang, G. T. Hager, J. M. Holden, Y. Wang, W. T. Lee, X. X. Bi, P.

- C. Eklund, D. S. Cornett, M. A. Duncan and I. J. Amster, Science, 1993, 259, 955–957.
- 46 Q. Burlingame, X. Tong, J. Hankett, M. Slootsky, Z. Chen and S. R. Forrest, *Energy Environ Sci*, 2015, **8**, 1005–1010.
- 47 T. M. Clarke, C. Lungenschmied, J. Peet, N. Drolet, K. Sunahara, A. Furube and A. J. Mozer, *Adv Energy Mater*, 2013, **3**, 1473–1483.
- 48 T. Heumueller, W. R. Mateker, A. Distler, U. F. Fritze, R. Cheacharoen, W. H. Nguyen, M. Biele, M. Salvador, M. Von Delius, H. J. Egelhaaf, M. D. McGehee and C. J. Brabec, Energy Environ Sci, 2016, 9, 247–256.
- 49 A. Distler, T. Sauermann, H. J. Egelhaaf, S. Rodman, D. Waller, K. S. Cheon, M. Lee and D. M. Guldi, *Adv Energy Mater*, 2014, **4**, 1300693.
- 50 S. K. Jung, J. H. Heo, D. W. Lee, S. C. Lee, S. H. Lee, W. Yoon, H. Yun, S. H. Im, J. H. Kim and O. P. Kwon, *Adv Funct Mater*, 2018, **28**, 1800346.
- 51 C. Cui, Y. Li and Y. Li, *Adv Energy Mater*, 2017, **7**, 1601251.
- 52 Z. Xiao, X. Geng, D. He, X. Jia and L. Ding, *Energy Environ Sci*, 2016, **9**, 2114–2121.
- 53 S. T. Kim, S. Y. Cho, C. Lee, N. S. Baek, K. S. Lee and T. D. Kim, *Thin Solid Films*, 2010, **519**, 690–693.
- 54 L. Qiu, Z. Liu, L. K. Ono, Y. Jiang, D. Y. Son, Z. Hawash, S. He and Y. Qi, *Adv Funct Mater*, 2019, **29**, 1806779.
- 55 M. A. Jameel, T. C. J. Yang, G. J. Wilson, R. A. Evans, A. Gupta and S. J. Langford, *J. Mater Chem A*, 2021, **9**, 27170–27192.
- 56 S. Molesky, Z. Lin, A. Y. Piggott, W. Jin, J. Vucković and A. W. Rodriguez, *Nat Photonics*, 2018, **12**, 659–670.
- 57 C. Yan, S. Barlow, Z. Wang, H. Yan, A. K. Y. Jen, S. R. Marder and X. Zhan, *Nat Rev Mater*, 2018, **3**, 1–19.
- 58 Y. Guo, J. Ma, H. Lei, F. Yao, B. Li, L. Xiong and G. Fang, *J Mater Chem A*, 2018, **6**, 5919–5925.
- 59 S. Li, Z. Zhang, M. Shi, C. Z. Li and H. Chen, *Phys. Chem. Chem. Phys*, 2017, **19**, 3440–3458.
- 60 D. Wang, T. Ye and Y. Zhang, *J Mater Chem A*, 2020, **8**, 20819–20848.
- 61 S. K. Jung, D. S. Lee, M. H. Ann, S. H. Im, J. H. Kim and O. P. Kwon, *ChemSusChem*, 2018, **11**, 3882–3892.
- 62 O. V Kharissova, B. I. Kharisov, C. Máximo, O. González, Y. Peña Méndez and I. López,

- R Soc Open Sci, 2019, 6, 191378.
- 63 P. Pimviriyakul and P. Chaiyen, *Enzymes*, 2020, **47**, 1–36.
- 64 E. C. Breinlinger, C. J. Keenan and V. M. Rotello, *J Am Chem Soc*, 1998, **120**, 8606–8609.
- 65 Y. M. Legrand, M. Gray, G. Cooke and V. M. Rotello, *J Am Chem Soc*, 2003, **125**, 15789–15795.
- 66 A. M. Edwards, Flavins and Flavoproteins: Methods and Protocols, 2014.
- 67 C. Dalal and N. R. Jana, *Langmuir*, 2019, **35**, 11380–11388.
- 68 S. Feng, F. Pei, Y. Wu, J. Lv, Q. Hao, T. Yang, Z. Tong and W. Lei, *Spectrochim Acta A Mol Biomol Spectrosc*, 2021, **246**, 119004.
- 69 S. Alonso-de Castro, A. Terenzi, S. Hager, B. Englinger, A. Faraone, C. Martínez, K. Keppler, W. Berger, L. Salassa and M. Sophia, *Sci Rep*, 2018, **8**, 17198.
- 70 T. Morack, J. B. Metternich and R. Gilmour, *Org Lett*, 2018, **20**, 1316–1319.
- 71 X. Yu, S. Eymur, V. Singh, B. Yang, M. Tonga, A. Bheemaraju, G. Cooke, C. Subramani, D. Venkataraman, R. J. Stanley and V. M. Rotello, *Phys. Chem. Chem. Phys.*, 2012, **14**, 6749–6754.
- 72 S. K. Jung, J. H. Heo, D. W. Lee, S. C. Lee, S. H. Lee, W. Yoon, H. Yun, S. H. Im, J. H. Kim and O. P. Kwon, *Adv Funct Mater*, 2018, **28**, 1800346.
- 73 M. Korzec, S. Kotowicz, K. Łaba, M. Łapkowski, J. G. Małecki, K. Smolarek, S. Maćkowski and E. Schab-Balcerzak, *European J Org Chem*, 2018, **2018**, 1756–1760.
- 74 D. Zhao, Q. Jiang, Y. Jia, J. Zhou, N. Zheng, D. Hu and Y. Ma, *Mater Today Energy*, 2021, 21, 100710.
- J. Hyuck Heo, S.-C. Lee, S.-K. Jung, O.-P. Kwon and S. H. Im, *J Mater Chem A*, 2017,13, 20615–20622.
- 76 D. Wang, T. Ye and Y. Zhang, *J Mater Chem A*, 2020, **8**, 20819–20848.
- 77 S. K. Jung, J. H. Heo, D. W. Lee, S. H. Lee, S. C. Lee, W. Yoon, H. Yun, D. Kim, J. H. Kim, S. H. Im and O. P. Kwon, *ChemSusChem*, 2019, **12**, 224–230.
- 78 J. L. Wu, W. K. Huang, Y. C. Chang, B. C. Tsai, Y. C. Hsiao, C. Y. Chang, C. T. Chen and C. T. Chen, *J Mater Chem A*, 2017, 5, 12811–12821.
- 79 P. Karuppuswamy, C. hanmandlu, K. Moorthy Boopathi, P. Perumal, C. ching Liu, Y. F. Chen, Y. C. Chang, P. C. Wang, C. S. Lai and C. W. Chu, *Solar Energy Materials and Solar Cells*, 2017, **169**, 78–85.

- 80 L. M. Svirskaite, S. Mandati, N. Spalatu, V. Malinauskiene, S. Karazhanov, V. Getautis and T. Malinauskas, *Synth Met*, 2022, **291**, 117214.
- 81 J. H. Heo, S. C. Lee, S. K. Jung, O. P. Kwon and S. H. Im, *J Mater Chem A*, 2017, **5**, 20615–20622.
- S. K. Jung, J. H. Heo, D. W. Lee, S. H. Lee, S. C. Lee, W. Yoon, H. Yun, D. Kim, J. H. Kim,
 S. H. Im and O. P. Kwon, *ChemSusChem*, 2019, **12**, 224–230.
- 83 T. Nakamura, N. Shioya, T. Shimoaka, R. Nishikubo, T. Hasegawa, A. Saeki, Y. Murata, R. Murdey and A. Wakamiya, *Chemistry of Materials*, 2019, **31**, 1729–1737.
- Bhosale and Q. Zhang, Asian J Org Chem, 2018, **7**, 2294–2301.
- 85 D. B. Shaikh, A. Ali Said, Z. Wang, P. Srinivasa Rao, R. S. Bhosale, A. M. Mak, K. Zhao, Y. Zhou, W. Liu, W. Gao, J. Xie, S. V. Bhosale, S. V. Bhosale and Q. Zhang, ACS Appl Mater Interfaces, 2019, 11, 44487–44500.
- W. Liu, D. B. Shaikh, P. S. Rao, R. S. Bhosale, A. A. Said, A. M. Mak, Z. Wang, M. Zhao,
 W. Gao, B. Chen, Y. M. Lam, W. Fan, S. V. Bhosale, S. V. Bhosale and Q. Zhang, *Chem Asian J*, 2020, **15**, 112–121.
- 87 S. Sung Kim, S. Bae and W. Ho Jo, *Chem. Commun*, 2015, **51**, 17413.
- 88 C. Chen, M. Cheng, H. Li, F. Qiao, P. Liu, H. Li, L. Kloo and L. Sun, *Materials Today*, 2018, **6**, 264–270.
- 89 I. E. Jacobs and A. J. Moulé, *Advanced Materials*, 2017, **29**, 1703063.
- 90 T. H. Kim, J. H. Kim and K. Kang, *Jpn J Appl Phys*, 2023, **62**, SE0803.
- 91 Z. C. Wen, H. Yin and X. T. Hao, *Surfaces and Interfaces*, 2021, **23**, 100921.
- 92 H. T. Chien, M. Pölzl, G. Koller, S. Challinger, C. Fairbairn, I. Baikie, M. Kratzer, C. Teichert and B. Friedel, *Surfaces and Interfaces*, 2017, **6**, 72–80.
- 93 Y. Liu, B. Nell, K. Ortstein, Z. Wu, Y. Karpov, T. Beryozkina, S. Lenk, A. Kiriy, K. Leo and S. Reineke, *ACS Appl Mater Interfaces*, 2019, **11**, 11660–11666.
- 94 X. Lin, B. Wegner, K. M. Lee, M. A. Fusella, F. Zhang, K. Moudgil, B. P. Rand, S. Barlow, S. R. Marder, N. Koch and A. Kahn, *Nat Mater*, 2017, **16**, 1209–1215.
- 95 E. H. Suh, Y. J. Jeong, J. G. Oh, K. Lee, J. Jung, Y. S. Kang and J. Jang, *Nano Energy*, 2019, **58**, 585–595.
- 96 W. Zhao, J. Ding, Y. Zou, C. A. Di and D. Zhu, *Chem Soc Rev*, 2020, **49**, 7210–7228.
- 97 T. Hoon Kim, J. Hwan Kim and K. Kang, *Jpn J Appl Phys*, 2023, **62**, SE0803.

- 98 K. Pei, Surfaces and Interfaces, 2022, **30**, 101887.
- 99 A. Panda, K. Ding, X. Liu and S. R. Forrest, *Phys Rev B*, 2016, **94**, 125429.
- 100 B. Lüssem, C. M. Keum, D. Kasemann, B. Naab, Z. Bao and K. Leo, *Chem Rev*, 2016,116, 13714–13751.
- 101 S. Olthof, S. Mehraeen, S. K. Mohapatra, S. Barlow, V. Coropceanu, J. L. Brédas, S. R. Marder and A. Kahn, *Phys Rev Lett*, 2012, **109**, 176601.
- 102 A. D. Scaccabarozzi, A. Basu, F. Aniés, J. Liu, O. Zapata-Arteaga, R. Warren, Y. Firdaus, M. I. Nugraha, Y. Lin, M. Campoy-Quiles, N. Koch, C. Müller, L. Tsetseris, M. Heeney and T. D. Anthopoulos, *Chem Rev*, 2022, **122**, 4420–4492.
- 103 M. L. Tietze, K. Leo and B. Lüssem, *Org Electron*, 2013, **14**, 2348–2352.
- 104 I. Salzmann, G. Heimel, M. Oehzelt, S. Winkler and N. Koch, *Acc Chem Res*, 2016, **49**, 370–378.
- 105 S. Hamwi, J. Meyer, T. Winkler, T. Riedl and W. Kowalsky, *Appl Phys Lett*, 2009, **94**, 253307.

Chapter 3. Experimental Methods

3.1. Nickel Oxide Nanoparticles Synthesis

6 g of nickel (II) nitrate hexahydrate (NiNO₃·6H₂O) was dissolved in 80 ml DI water and stirred until fully dissolved. Next, 80 ml of sodium hydroxide (NaOH) (0.001 mol/ml in DI water) was added dropwise to NiNO₃ solution at a controlled rate to ensure uniform droplet formation. The mixture was stirred for 5 minutes before being centrifugated at 10000 rpm for several cycles. The precipitate was then washed and dispersed in DI water. A light green product was obtained, which was freeze-dried for 48 hours. Finally, the product was annealed at 270 °C for 120 minutes, resulting in the formation of nickel oxide nanoparticles (NiOx NPs) in powder form.

3.2. Inverted Perovskite Solar Cells Fabrication and Measurements

3.2.1. Precursor Preparation

MAPbl₃ (MAPI) Solution 750 mg of lead (II) iodide (Pbl₂) and 240 mg methylammonium iodide (MAI) was dissolved in 1 ml of dimethylformamide/dimethyl sulfoxide (DMF/DMSO) mixture (4:1 volume ratio). The solution was heated overnight at 60°C. The MAPI solution was filtered before use.

Double-cation (DC) Perovskite Solution 433 mg of PbI2, 155 mg of formamidinium iodide (FAI), 26 mg of caesium iodide (CsI) and 22 mg of lead (II) bromide (PbBr₂) was dissolved in 571uL of DMF and 143 uL of DMSO and heated at 60°C for overnight. The DC solution was filtered before use.

Triple-cation (TC) Perovskite Solution It was prepared by dissolving 726 mg of PbI₂, 208 mg of FAI, 33 mg of MAI, 19 mg of CsI and 14 mg of lead (II) chloride (PbCl₂) in 1 ml DMF/DMSO mixture (4:1 volume ratio) and heated overnight at 70°C. The TC solution was filtered before use.

Layered Perovskite Solution 1 mg/ml of phenethylammonium iodide (PEAI) was dissolved in isopropanol (IPA) and heated overnight at 60°C

HTL Solution (*MAPI- and DC-based devices*) 0.5 mg/ml in IPA of MeO-2PACz, 2PACz, or Me-4PACz was heated overnight at 60 °C. (*TC based devices*) 3 mg/ml in ethanol of MeO-2PACz was heated overnight at 70 °C.

ETL Solution 20 mg/ml in chlorobenzene (CB) of PCBM was heated at 60 °C (*MAPI-and DC-based devices*) or 70 °C (*TC-based devices*) overnight with stirring. For nonfullerene ETL solutions, 15 mg of NDI/BF derivatives were dissolved in 1 ml CB at 70°C. Undoped solutions were heated overnight, while doped species were heated for optimized times (doped NDI-G for 2 hours, doped NDI-EtHx for 16 hours, doped BFG for 3 hours and doped BFA for 6 hours). All solutions were filtered before use.

Hole blocking layer (*MAPI- and DC-based devices*) 0.5 mg of bathocuproine (BCP) in 1 ml of IPA was heated overnight at 60 °C. (*TC based devices*) 1 mg of BCP in 1 ml of IPA was heated overnight at 70 °C.

3.2.2. MAPbl₃ and Double-cation Perovskite Based Device

The fabrication of these devices was carried out at University of Hong Kong. The device structure is ITO/NiOx NPs/SAMs/perovskite/PEAI/BCP/Ag, and the device pattern is shown in Figure 3.1.

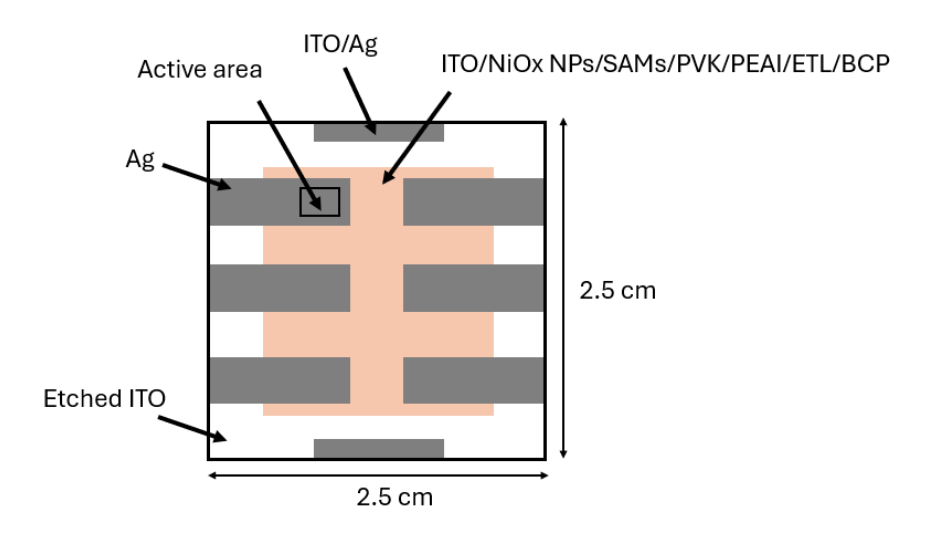


Figure 3.1 Device pattern of MAPbI₃ and DC perovskite based device

The 2.5 cm x 2.5 cm pattern ITO substrates were sonicated sequentially in detergent (1% Decon 90 in DI water), DI water, acetone and ethanol by 15 minutes in each solvent and dried with nitrogen flow. The substrates were carried out oxygen plasma at 10 V for 10 seconds. A 20 mg/ml solution of NiOx NPs in DI water was spin-coated onto ITO substrates at 4000 rpm for 30 seconds, followed by annealing at 110 °C for 10 minutes in ambient conditions. The samples were then transferred into a glovebox. MeO-2PACz, 2PACz and Me-4PACz were deposited *via* spin-coating at 4000 rpm for 30 seconds, and the samples were annealed at 100°C for 10 minutes and cooled down to room temperature.

The MAPI film was deposited using a two-step spin coating process. First, the substrate was spun at 1000 rpm for 5 seconds, followed by the addition of 50 uL of MAPI solution. Then, the substrate was started at 5000 rpm for 25 seconds, during which 300 uL of CB was dropped onto the film after 5 seconds. Once deposited, the MAPI film was dried for 15 minutes, annealed at 100°C for another 15 minutes, and subsequently cooled down to room temperature.

The DC perovskite film was also prepared *via* a two-step spin coating process. The substrate was first spun at 2000 rpm for 10 seconds, followed by 4000 rpm for 30 seconds. Before starting the process, DC precursor was dropped onto the substrate and during the last 10 seconds of the 2nd step, 250 uL of CB was added to the film. The perovskite film was annealed at 100°C for 30 minutes. After annealing and cooling to room temperature, the PEAI was deposited onto the DC perovskite layer at 5000 rpm for 30 seconds, followed by 100 °C for 3 minutes.

The PCBM ETL was deposited by spin coating at 1200 rpm for 30 seconds, followed by an annealing at 100 °C for 10 minutes. After cooling to the room temperature, the BCP layer was spin-coated at 4000 rpm for 30 seconds. A 100 nm silver (Ag) was prepared using thermal evaporator through a shadow mask with an electrode area of 0.09 cm². The completed devices were encapsulated using microscope glass and polyisobutylene tape, with edges sealed using UV-cured epoxy. To measure the performance of the devices, J-V measurements were performed using a Keithley 2400 source measure unit at 100

mW/cm² under AM1.5G spectrum solar simulator (ABET Sun 2000) and calibrated using an Enli PVM silicon standard reference cell. The aperture area of metal masks was 0.04 cm².

3.2.3. Triple-cation Perovskite Based Device

The fabrication of these devices was carried out at University of Glasglow. The device structure is ITO/SAMs/Al₂O₃ NPs/perovskite/BCP/Ag, and the device pattern is shown in Figure 3.2.

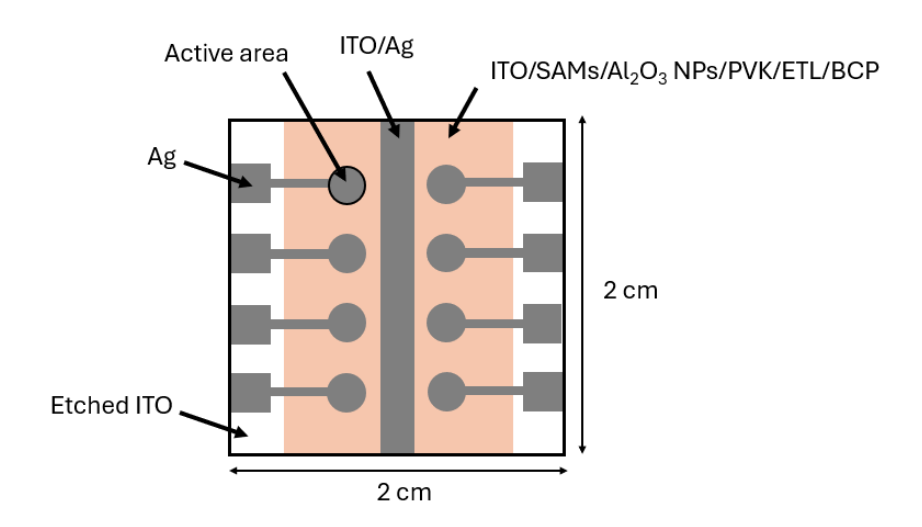


Figure 3.2 Device pattern of TC perovskite based device

The 2 cm x 2 cm pattern ITO substrates were initially cleaned by sequentially treating them with 8% Decon-90 solution, DI water, acetone, ethanol and a final rise with DI water. The substrates were dried with nitrogen flow and exposed to UV ozone for 20 minutes. The samples were then transferred into a glovebox. The MeO-2PACz was prepared by spin coating at 4000 rpm for 30 seconds, followed by annealing at 100° C for 15 minutes. Subsequently, a 0.2 wt% of Al_2O_3 NPs in IPA was spin coated onto SAMs at 2000 rpm for 30 seconds and dried at 100° C for 5 minutes and cooled down to room temperature. The TC perovskite precursor solution was deposited on the substrates using a one-step spin coating at 4000 rpm for 40 seconds. During the last 15 seconds of the spin coating, 200 uL of ethyl acetate was added. After deposition, the perovskite layer was annealed at 100° C for 30 minutes. The ETL was formed by spin coating a PCBM solution onto the perovskite layer at 3000 rpm for 20 seconds, followed by annealing at 100° C for 15

minutes and subsequently cooling to room temperature. For non-fullerene-based devices, ETLs were prepared at 2000 rpm for 30 seconds. Next, the BCP layer was prepared by spin coating onto ETL at 5000 rpm for 30 seconds. Finally, a 100 nm thick layer of Ag was thermally evaporated to create the top electrode. The devices were then encapsulated using microscope glass and sealed with epoxy. Device performance was evaluated under AM1.5G simulated sunlight, provided by WaveLabs SIN-US70 solar simulator equipped with UV and UR range extenders. The aperture area of metal masks and active area were 0.098 cm².

3.3. Characterization

3.3.1. Conductivity Measurement

For the conductivity measurements, 2 cm x 2 cm ITO substrates were patterned by etching a channel into the substrate, as illustrated in Figure 3.1a. The material of interest was prepared *via* spin coating under the same conditions as the TC perovskite devices, the conductivity of the materials was measured across the channel, as shown in Figure 3.3. The samples were encapsuled using microscope glass and Parafilm. Conductivity reflects the charge transport of material in the presence of an electric field. It can be analysed by the I-V characteristics of thin films measured by two-point probe method. The conductivity (σ) of thin film, expressed in siemens per meter (S/cm), can be calculated using the following relationships

$$\rho = \frac{AR}{L}$$

$$\sigma = \frac{1}{\rho} = \frac{L}{A} \cdot \frac{1}{R}$$

Where:

 ρ is the resistivity

A is the cross-sectional area of the thin film (width x thickness)

L is the length of thin film

R is the resistance of given thin film

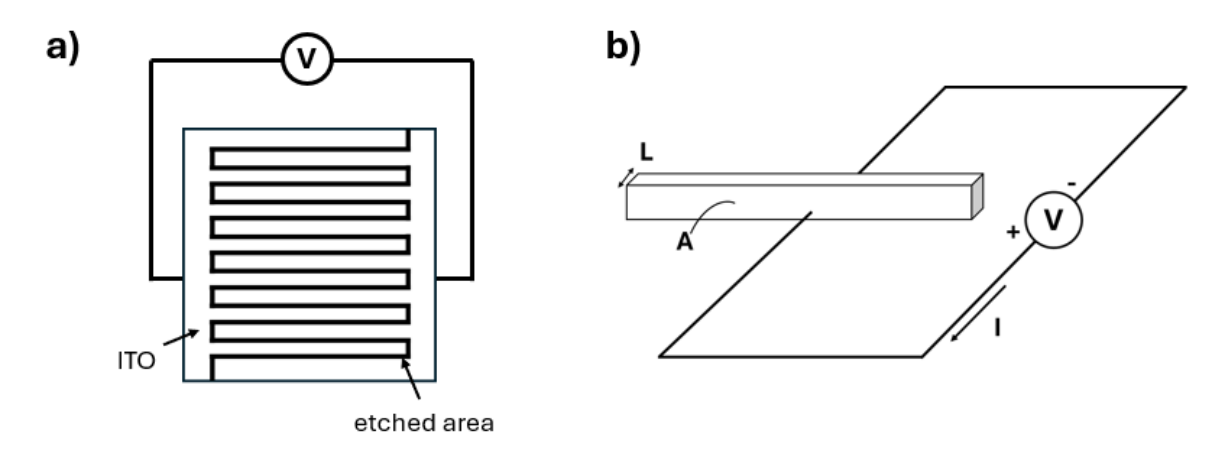


Figure 3.3. a) Pattern of etched ITO and b) conductivity measurement of the etched area

3.3.2. Electron Paramagnetic Resonance Spectroscopy

The measurements were conducted by Dr Stephen Sproules at University of Glasgow, United Kingdom.

Electron paramagnetic resonance (EPR) spectra were measured using Bruker ELEXSYS E500 spectrometer. The sample was irradiated at 450 nm during data acquisition. For BF, the concentration of pristine and 20mol% N-DMBI addition with BFG and BFA were 1.76 x10⁻² M and 1.97 x10⁻² M in CB, respectively. For NDI, the concentration of undoped and doped NDI-G and NDI-EtHx were 3.57x10⁻² M and 4.08x10⁻² M in CB, respectively. The mixtures were heated at 70°C for optimised times (3 hours for BFG, 6 hours for BFA, 2 hours for NDI-G and 16 hours for NDI-EtHx). The samples were then transferred into soda glass capillary tubes of 2 mm diameter, sealed at one end, and filled to a height of 20 mm.

EPR spectroscopy is used to study the chemical species with unpaired electrons. In EPR, the sample is placed at the centre of a microwave cavity within the magnetic field produced by electromagnets, as depicted in Figure 3.4. EPR operated by generating microwave from a source (typically a klystron), which are directed at the sample in the microwave cavity. These microwaves are reflected to the detector, and the resulting signal is detected as a decrease in current, analogous to microwave absorption by the sample. When an electron is located within an applied magnetic field (*B*), its two possible

spin states correspond to different energies. The lower or higher energy state occurs when the magnetic moment of the electron is aligned with or against the magnetic field, respectively. When the energy difference between these two states matches the photon energy of the microwaves, the electron absorbs energy and transitions from the lower to the higher energy state.

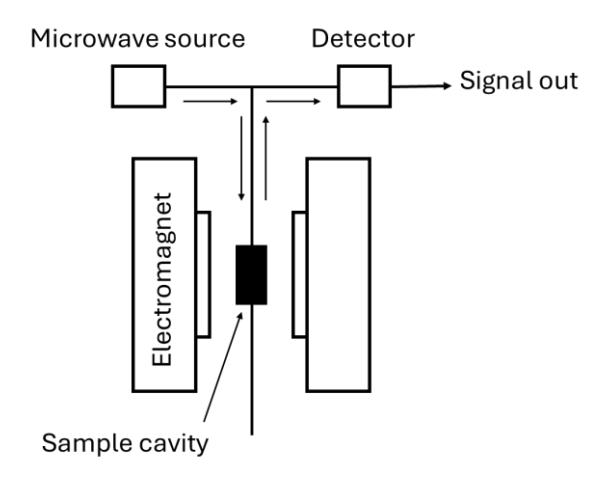


Figure 3.4. Schematic diagram of an EPR spectrometer

The EPR spectrum typically exhibits an absorption profile (Figure 3.5a), with its first derivative (Figure 3.5b). The maximum absorption point, represented as the zero crossing in the first derivative, is used to determine the centre of signal, expressed as the g-factor¹, which reflects how strongly an electron's magnetic moment interacts with the external magnetic field. For organic radicals, the g-factor generally between from 1.99 to 2.01, close to that of a free electron.²

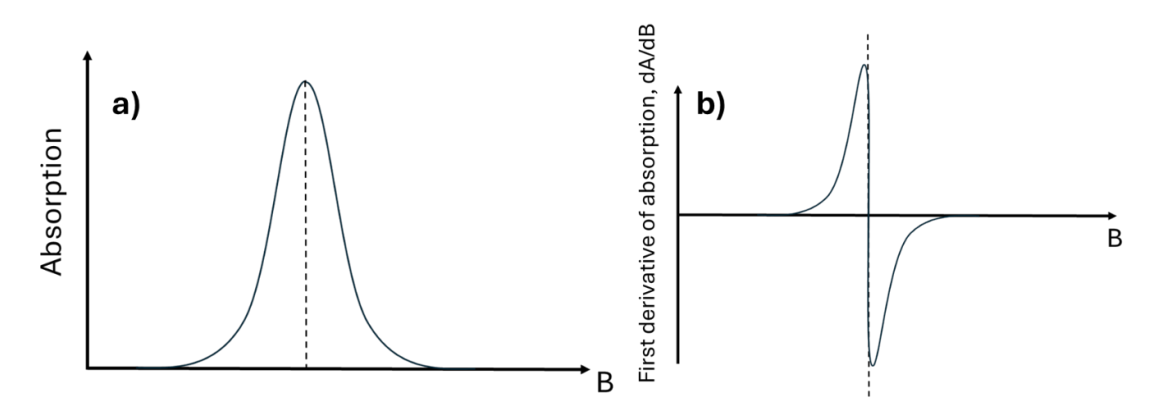


Figure 3.5. Comparison of a) absorption spectrum and b) ESR spectrum (first derivative)

3.3.3. Scanning Electron Microscopy

In chapter 4 and 5, scanning electron microscopy (SEM) measurements were conducted by TESCAN CLARA S8152, with an acceleration voltage of 15kV and a beam current of 300 pA. The samples used for SEM analysis had the structure ITO/MeO-2PACz/Al₂O₃ NPs/PVK/ETL, prepared using the spin coating method under the same conditions as those employed for fabricating the TC PSCs. Samples were electrically grounded to the mounting stub using silver paint to minimise charge buildup during the measurement. In chapter 6, SEM was measured by Hitachi S-4800, with an acceleration voltage of 5000 V and a beam current of 9800 nA. The samples used for SEM analysis had the structure ITO/NiOx NPs/SAMs/PVK, prepared using the spin coating method under the same conditions as those employed for fabricating the MAPI and DC PSCs. Samples were electrically grounded to the mounting stub using gold sputtering to minimise charge buildup.

SEM is used to analyse the surface morphology of a specimen using an electron beam. In Figure 3.6, the electron beam, emitted from an electron gun, passes through a series of the lenses before interacting with the samples. The interaction generates various signals, including secondary electrons, backscattered electrons, and characteristic X-rays. Secondary electrons resulted from inelastic collisions between sample and primary electrons, providing topography information. On the other hand, backscattered electrons arise from elastic collisions and relate to the atomic number from the sample, allowing for contrast imaging based on atomic number differences. Additionally, characteristic X-rays are produced by electron transitions between atomic orbitals, allowing for elemental composition analysis through energy dispersive X-ray spectroscopy (EDX).^{3,4}

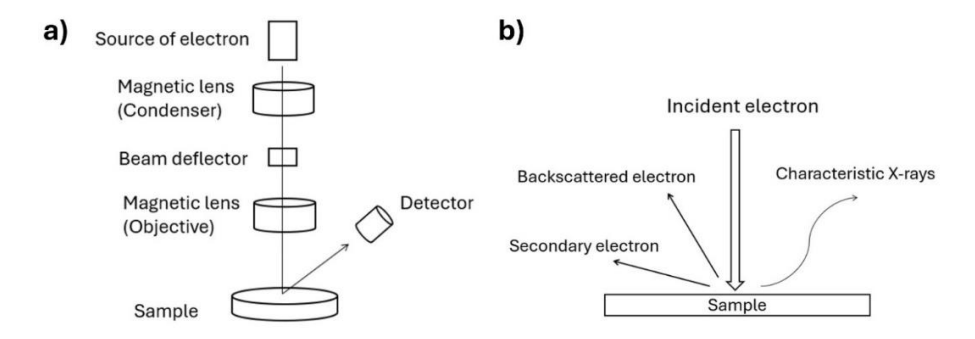


Figure 3.6. Schematic diagram of a) SEM components and b) operational principles

3.3.4. X-Ray Diffraction

X-ray diffraction (XRD) patterns were measured using a Rigaku MiniFlex600 with Cu K α X-ray source in θ –2 θ scan mode with steps of 0.01° from 5° to 50°. The samples used for XRD had the structure ITO/NiOx NPs/SAMs/PVK, prepared using the spin coating method under the same conditions as those employed for fabricating the MAPI and DC PSCs. XRD is used to analyse the composition, crystallinity and phase purity of a sample. 5 X-ray pass through the sample, scattering off atoms and creating diffraction patterns based on atomic spacing. Constructive interference between diffracted beams leads to stronger signals at certain angles, which are analysed using Bragg's law. 5,6

$$sin\theta = \frac{n\lambda}{2d}$$

Where:

 λ is the wavelength

 Θ is the diffraction angle

d is the distance between atomic planes

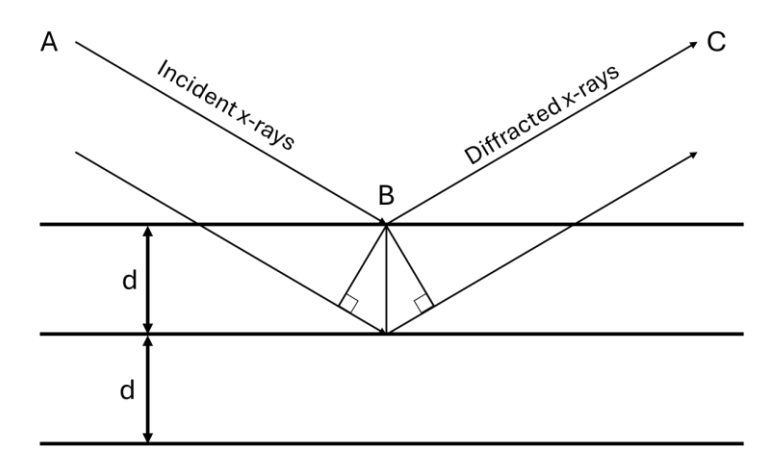


Figure 3.7. Schematic diagram of X-rays incident on a crystal structure

3.3.5. UV-Vis Absorption Spectroscopy

UV-Vis absorption spectra were measured using Shimadzu UV 3600 UV/visible/IR spectrometer. For the solution state measurement, the concentration of solutions was kept at 10⁻⁵ M in CB. N-DMBI were added to the solution for the doping with specific mole percentage or certain reaction times, and these samples were used for the UV-Vis absorption measurement. For the solid-state measurement, it prepared using the spin

coating method under the same conditions as those employed for fabricating the solar cell devices, and encapsuled using microscope glass and Parafilm.

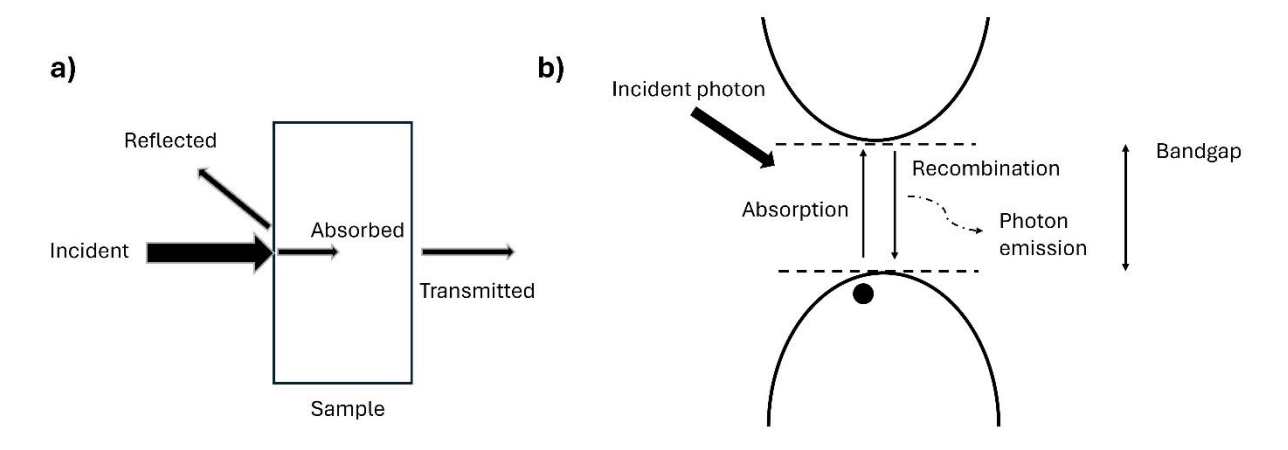


Figure 3.8. a) UV-vis absorption measurement and b) working principle

UV-Vis absorption spectroscopy measures the optical properties of materials by determining the absorption of ultraviolet and visible region. It can be used to analyse the transitions of molecules when excited by UV and visible light. When the photon energy is equal to or larger than the bandgap of the material. An electron in the lower energy level absorbs an incident photon and excites into an available state in the higher energy level, as shown in Figure X.⁷ In a UV-Vis absorption spectrometer, the sample is placed between the light source and the detector.⁸ Incident light can be transmitted, absorbed or reflected.

$$I_0 = I_T + I_A + I_R$$

Where:

I₀ is the intensity of incident light

I_{Tr} is the intensity of after transmission

 I_A is the intensity of light after absorption

I_R Is the intensity of light after reflection

Transmittance (Trans) is the ratio of intensity of light passing through the solution (I) to intensity of incident light (I_0).

$$Trans = \frac{I}{I_0}$$

Absorbance (*Abs*) is governed by the Beer-Lambert, describing the amount of light absorbed by the solution, which is proportional to the concentration of solution.

$$Abs = \varepsilon C_{soln} L_{PL} = -log \frac{I}{I_0}$$

Where:

 ε is the absorption coefficient

 C_{soln} is the solution concentration

 L_{PL} is the path length

3.3.6. Cyclic Voltammetry

Cyclic voltammetry (CV) was performed using a CH Instruments Electrochemical Workstation (CHI 440a), Austin, TX, USA. Samples were in solution of electrolyte (tetrabutylammonium hexafluorophosphate) with a scan rate of 0.1 V/s. A glassy carbon working electrode, a Pt wire reference electrode and a coiled Ag wire counter electrode were used. All solutions were purged with N_2 prior to use. The concentration of BF and NDI samples were $8 \times 10^{-4} \, \text{M}$ and $1 \times 10^{-4} \, \text{M}$ in CH_2Cl_2 , respectively.

CV analyses the chemical reactivity of molecular species through oxidation and reduction process. Figure 3.9 illustrates that ionization potential (IP) is the energy required to take away an electron from the molecule (oxidation), and electron affinity (EA) is the energy required to add an electron to the molecule (reduction), can be estimated using CV measuremenst.⁹ These values provide an approximation of the HOMO and LUMO level.¹⁰ The redox potentials of E_{ox} and E_{red} are determined by CV and referenced against ferrocene. The IP and EA are calculated using:

$$E(IP) = -(E_{ox}^{onset} + 4.78)eV$$

$$E(EA) = -(E_{red}^{onset} + 4.78)eV$$

Where:

4.78 is the correction factor for the unit conversion from V to eV11

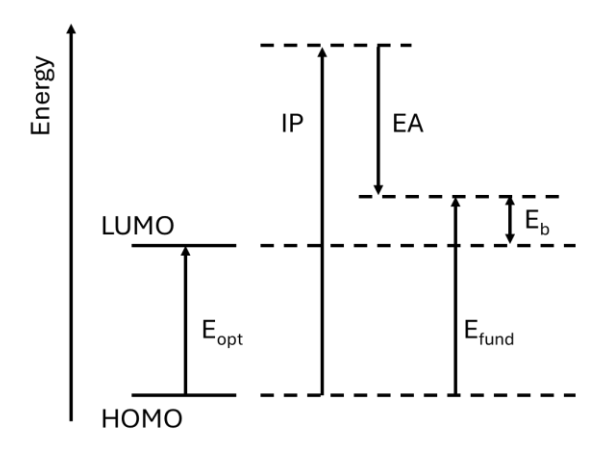


Figure 3.9. Schematic diagram of energy level. E_{opt} represents the optical band gap between HOMO and LUMO. E_{fund} is a fundamental gap, representing the energy difference between the IP and EA. E_b is the electron-hole pair binding energy. The E_{opt} is generally lower than E_{fund} because the electron and hole remain electrostatically bound to another in the excited state 10

3.3.7. Time-Resolved Photoluminescence Spectroscopy

The measurements were performed by Dr Mohammad Umair Ali at the University of Hong Kong, Hong Kong.

The excitation source for Time-resolved photoluminescence (TRPL) measurement was at 375 nm 200 ns laser diode (Edinburgh FLS1000 Photoluminescence Spectrometer) with switchable repetition rates operating at 1 MHz and 200 kHz. The samples used for TRPL analysis had the structure ITO/NiOx NPs/SAMs/PVK, prepared using the spin coating method under the same conditions as those employed for fabricating the MAPI and DC PSCs. TRPL studies direct recombination of charge carrier in perovskite. 12-15 The recombination mechanisms include bimolecular recombination, recombination and Auger recombination processes, as shown in Figure 3.10. At low excitation densities, charge carriers recombine primarily via trapping recombination, caused by traps and impurities within perovskite material. Once these trap states are saturated, bimolecular recombination begins to occur, where free electrons in the conduction band recombine with holes in the valence band, accompanied by the photon emission. Augur recombination involves energy transfer to another charge carrier during the recombination process.16

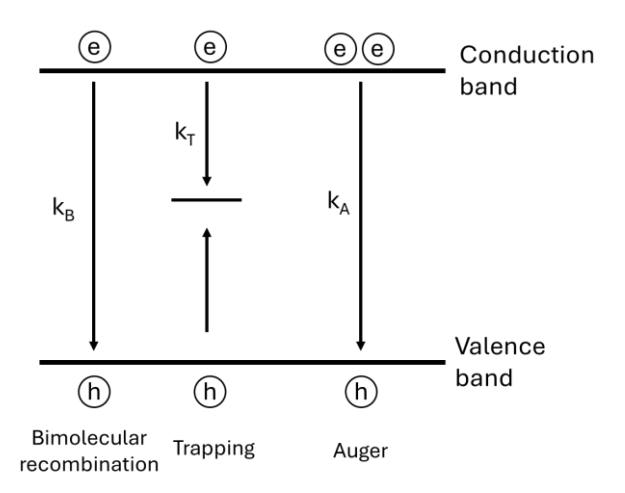


Figure 3.10. Schematic diagram of charge carrier recombination process (Bimolecular-Trapping-Auger model)¹⁷

During radiative recombination, photon emission occurs, generating a PL signal that can be measured using the PL spectroscopy. The recombination lifetime of charge carries typically ranges from nanoseconds (ns) to microseconds (µs). Po-22 Additionally, non-radiative recombination and Auger recombination can influence the overall recombination dynamics. By applying theoretical fitting to the experimental TRPL data, these dynamic processes can be quantitatively analysed to link the physical mechanisms and the observed results.

For the TRPL data, we used the web-based TRPL fitting tool PErovskite cArrier Recombination Simulator (PEARS), which enables effortless and rapid fitting of TRPL measurements for perovskite materials. The tool incorporates advanced charge carrier recombination modes, allowing for the extraction of recombination rate constants and trap state concentration.¹⁷ The bimolecular-trapping-auger model assumes that the trap states remain mostly empty, thus allowing trapping and de-trapping to be considered monomolecular processes. The model gives the rate equation for the carrier concentration in a short period of time as:¹⁷

$$\frac{dn}{dt} = -k_T n(t) - k_B n^2(t) - k_A n^3(t)$$

Where:

 k_T is the constant of monomolecular trapping rate

k_B is the constant of bimolecular rate

 k_A is the constant of Auger recombination rate

3.3.8. Kelvin Probe Force Microscopy

The measurements were performed by Mr. Tik Lun Leung at University of New South Wales, Australia.

Atomic force microscopy (AFM) and Kelvin probe force microscopy (KPFM) images of different samples were obtained from a Neaspec s-SNOM system with a PtIr5 coated AFM probe (Arror EFM, Nanoworld). Illumination on the sample was done with the lighting LED in the sample compartment. The work function of the sample was obtained by subtracting the surface potential of a sample from the tip's work function, which was calibrated with a gold film. All samples were prepared with the structure of ITO/NiOx NPs/SAMs/DC/PEAI using the spin coating, under the same conditions as the MAPI and DC PSCs.

KPFM is an extension of the AFM, capable of operating in contact, tapping and non-contact modes. In the contact mode, the AFM tip touches the sample surface, and the repulsive forces between the sample and tip cause cantilever deflection. This deflection is detected, producing a signal. In tapping mode, also known as amplitude modulation (AM), and non-contact mode, also referred to as frequency modulation (FM), the interaction between the sample and tip depends on changes in sample-tip distance. This interaction leads to variation in either the oscillation amplitude in AM mode or the resonance frequency in FM mode. The signals obtained from these two modes provide topography information about the sample surface.²³

In both tapping and non-contact modes AFM, the interaction between sample and tip is influenced by attractive and repulsive forces, resulting in amplitude or frequency of the AFM tip's oscillation, as shown in Figure 3.11. For the AM mode AFM, a decrease of sample-tip interaction causes an increase in distance between them, resulting in a higher oscillation amplitude. The variation in amplitude is detected and the feedback system maintains a constant sample-tip distance. For the FM mode AFM, change in oscillation

frequency due to varying sample-tip distance are monitored, with the feedback system maintaining a constant frequency.²³

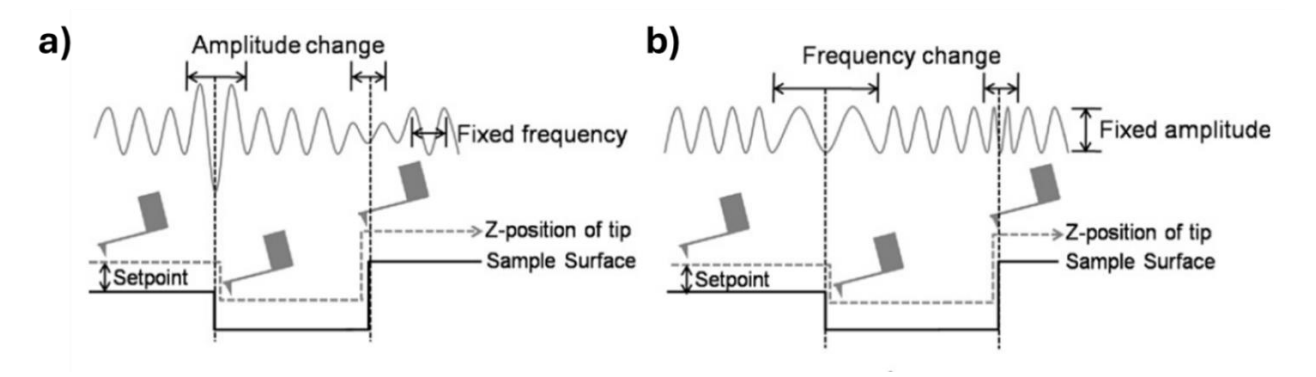


Figure 3.11. Illustration diagram of a) AM mode and b) FM mode²³

KPFM measures the contact potential difference (CPD) between a sample and an AFM tip. The CPD (V_{CPD}) is defined as:

$$V_{CPD} = \frac{\varphi_{tip} - \varphi_{sample}}{-e}$$

Where:

 $\phi_{\it tip}$ and $\phi_{\it sample}$ are the work functions of tip and sample e is the electronic charge

Due to the Fermi energy difference between the sample and the tip, an electrical force is generated when the tip is brought close to the sample surface. Initially, when the tip and sample are separated by distance d, there is no electrical contact and their Fermi levels differ, although their vacuum levels are aligned, as depicted in Figure 3.12a. However, when they come into electrical contact (when the tip is sufficiently close), electron flow causes their Fermi levels to align, creating a voltage difference known as V_{CPD} (Figure 3.12b). This electrical force can be nullified by applying an external bias (V_{DC}) equal to the V_{CPD} , allowing the work function of the sample to be calculated if the work function of the tip is known.²³

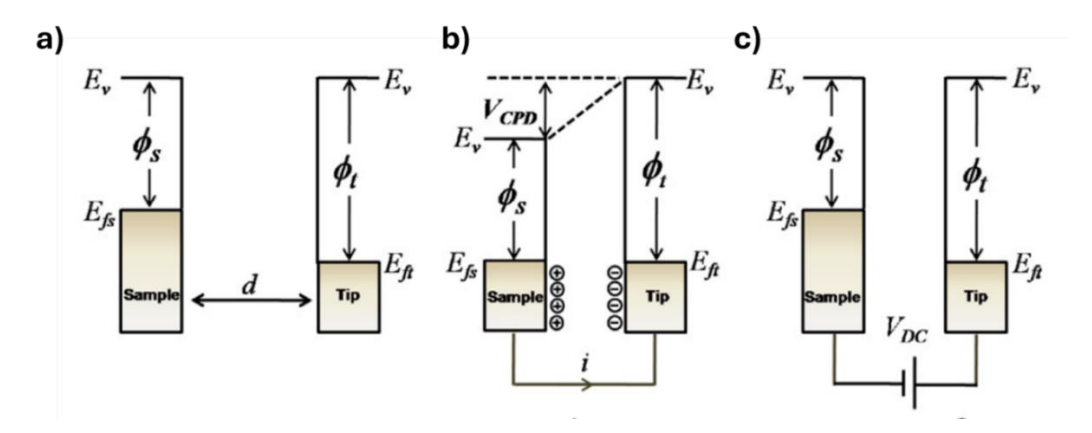


Figure 3.12. Energy level diagram of sample and AFM tip: a) sample and tip are separated by distance, d with no electrical contact; b) sample and tip are electrical contact and c) external bias is applied to nullify the CPD. (E_v : vacuum energy level. E_{fs} and E_{ft} : Fermi energy levels of the sample and tip, respectively.)²³

3.3.9. Stabilize and Pulse Measurements

The measurements were performed by Mr. Fraser. J. Angus at University of Glasgow, United Kingdom.

Stabilize and pulse (SaP) measurements determines the interfacial energy level offsets in a device stack. ^{24,25} At lower scan rate (below 500 mV/s), ionic vacancies within the perovskite can migrate with the applied voltage, resulting in JV hysteresis. The scan rate at which hysteresis is most pronounced correlates with the activation energy of the mobile ions in perovskite. ²⁶ By tailoring the material to modify the ion motion activation energy, it is possible to achieve hysteresis-free operation between 10 to 200 mV/s scan rates. However, if the perovskite contains a significant number of mobile vacancies or recombination sites, hysteresis may still be observed over a broad range of scan rates. ^{27,28} The absence of hysteresis in a JV measurement does not indicated the absence of mobile ions but instead suggests that ionic distribution during the measurement was either negligible or effectively mitigated by interfacial energy offsets introduced by the extraction layer.

For SaP analysis, JV curves were initially recorded for each device under an AM 1.5M solar simulator before transferring them to the SaP setup for further evaluation. A Cree

High Power white LED was used as the light source and calibrated to match the measured Jsc of each device. Voltage pulses were applied using an Ossila Source Meter Unit, with each pulse lasting approximately 40 ms and a 1 s stabilization period between pulses. 1 ms was used for the source delay. Bias voltages were incremented in 50 mV steps, with a stabilization interval of at least 120 s before each adjustment. In certain case, the stabilisation period was extended to ensure a consistent current response. To minimise device degradation, measurements were performed under reduced illumination intensity, approximately equivalent to 0.5 suns.²⁹

JV curves were reconstructed using the stabilise-and-pulse approach, as depicted in Figure 3.13a. To extract the electrostatic potential drop, 5 points were taken at Voc and a third order polynomial fit. The slope of JV curves represents the series resistance, and it exhibits the enhancement during ion migration (iodide vacancies) from HTL/perovskite interface to perovskite/ETL interface, which exhibits significantly improved when the mobile ions evenly distributed in the light illumination as discussed in section 2.3, giving a steeper slope. The gradient was analysed giving dJ/dV, as illustrated in Figure 3.13b. The second derivative (d²J/dV²) of the smoothed data identified the inflection point corresponding to the steepest gradient (Figure 3.13c). A range of data points in this region was selected for multiple linear fits, with their intersection determining the midpoint between the sigmoid's maxima and minima in Figure 3.10d.²⁹

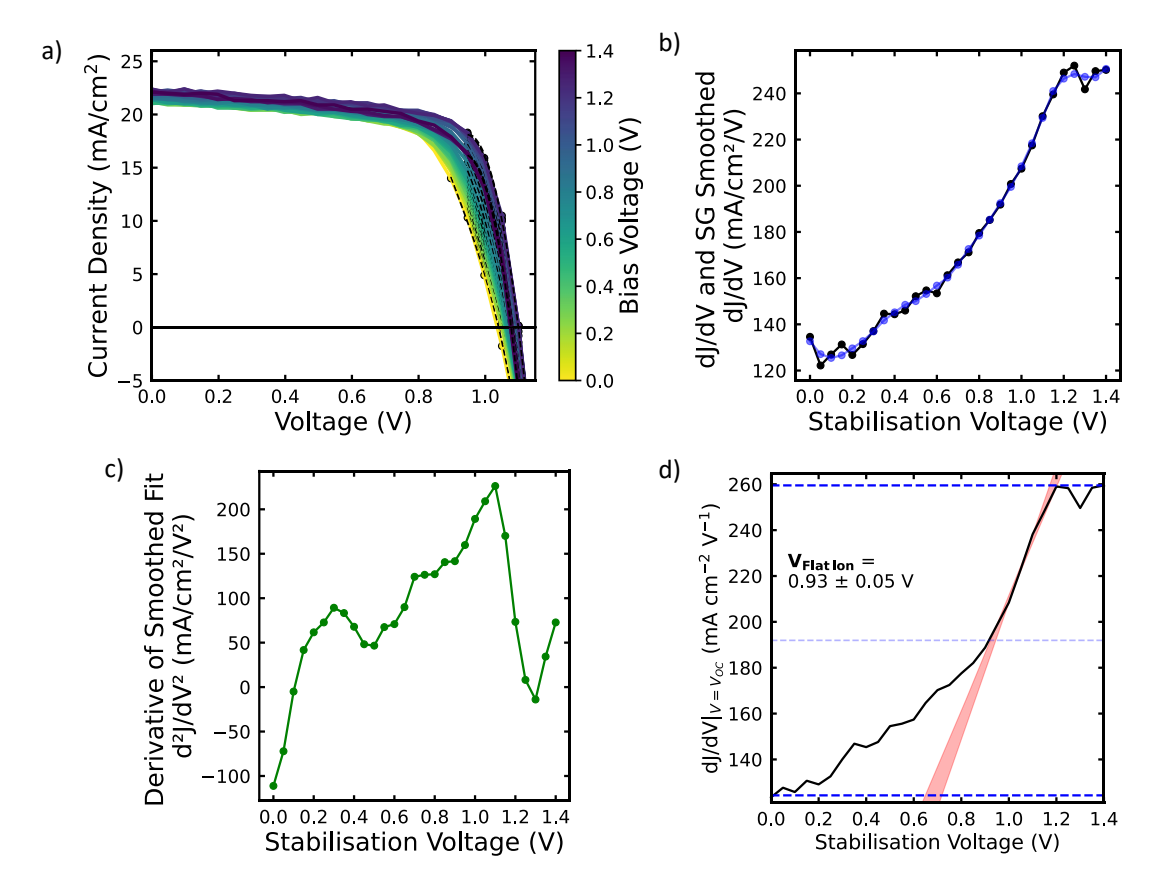


Figure 3.13. a) JV curves obtained from SaP measurements; b) Calculated gradient around Voc, with a 7-point 3rd order Savitzky-Golay filter applied to smooth the data; c) Second derivative of dJ/dV data, indicating the location of the steepest gradient and d) Final analysis of the electrostatic potential drop across the perovskite layer with shaded red region representing the range of linear fits²⁹

3.3.10. Density Functional Theory

The measurements were performed by Dr Dylan Wilkinson and Dr Lewis Mackenzie at University of Glasgow, United Kingdom.

Density functional theory (DFT) was employed to optimise the structural geometry and calculate molecular energy levels. The calculations used Gaussian 09 program. The geometries of BFA and BGF were optimized at the B3LYP level of DFT with the 6-311G(2df2p) basis set, and the geometry of the radical anions were optimised, and the corresponding spin density distributions were calculated at the spin-unrestricted B3LYP level of DFT with the 6-311G(2df2p) basis set. The fully optimized structures were confirmed to be true minima by vibrational analysis, which showed no imaginary

frequency. Excitation energies and oscillator strengths for the optimized structures were calculated with the TD-DFT method at the B3LYP/6-311G(2df2p) level. To facilitate convergence, the side-chain of each derivative were truncated to methyl groups.³⁰

3.4. References

- 1 L. Zhuang and J. Lu, In-situ ESR for Studies of Paramagnetic Species on Electrode Surfaces and Electron Spins Inside Electrode Materials, Elsevier Science B.V., 2007.
- 2 C. K. Borrowman, S. Zhou, T. E. Burrow and J. P. D. Abbatt, Physical Chemistry Chemical Physics, 2015, 18, 205–212.
- 3 A. Ul-Hamid, A Beginners' Guide to Scanning Electron Microscopy, Springer International Publishing, 2018.
- 4 W. Zhou, R. Apkarian, Z. L. Wang and D. Joy, in Scanning Microscopy for Nanotechnology: Techniques and Applications, Springer, New York, NY, 2006, pp. 1–40.
- 5 S. Fatimah, R. Ragadhita, D. F. Al Husaeni and A. B. D. Nandiyanto, ASEAN Journal of Science and Engineering, 2022, 2, 65–76.
- 6 A. A. Bunaciu, E. gabriela Udriştioiu and H. Y. Aboul-Enein, Crit Rev Anal Chem, 2015, 45, 289–299.
- 7 N. Shanker and S. L. Bane, Methods Cell Biol, 2008, 84, 213–242.
- 8 G. L. Hornyak, J. Dutta, H. F. Tibbals and A. Rao, Introduction to Nanoscience, CRC Press, 2008.
- 9 S. Pluczyk, M. Vasylieva and P. Data, J Vis Exp, 2018, e56656.
- 10 J. L. Bredas, Mater Horiz, 2013, 1, 17–19.
- 11 S. Hasiah, A. Nora'aini, C. C. Yap, M. S. Azhar, I. Nurhayati, K. Nurul Huda, M. G. Salmah and N. A. Nik Aziz, Solid State Phenomena, 2020, 307, 207–216.
- 12 U. Noomnarm and R. M. Clegg, Photosynth Res, 2009, 101, 181–194.
- 13 T. Kirchartz, J. A. Márquez, M. Stolterfoht and T. Unold, Adv Energy Mater, 2020, 10, 1904134.
- 14 E. Ugur, E. Alarousu, J. I. Khan, A. Vlk, E. Aydin, M. De Bastiani, A. H. Balawi, S. P. Gonzalez Lopez, M. Ledinský, S. De Wolf and F. Laquai, Solar RRL, 2020, 4, 2000382.
- 15 Y. Zhu, Q. Cui, J. Chen, F. Chen, Z. Shi, X. Zhao and C. Xu, ACS Appl Mater Interfaces, 2021, 13, 6820–6829.
- 16 J. Chen, J. Lv, X. Liu, J. Lin and X. Chen, Physical Chemistry Chemical Physics, 2023, 25, 7574–7588.
- 17 E. V. Péan and M. L. Davies, J Chem Inf Model, 2023, 63, 4477–4482.
- 18 C. Li, A. Wang, X. Deng, S. Wang, Y. Yuan, L. Ding and F. Hao, ACS Photonics, 2020, 7,

- 1893–1907.
- 19 I. A. Alfurayj, Z. Li and C. Burda, Journal of Physical Chemistry C, 2021, 125, 15113–15124.
- 20 S. Makuta, M. Liu, M. Endo, H. Nishimura, A. Wakamiya and Y. Tachibana, Chemical Communications, 2015, 52, 673–676.
- 21 S. Song, G. Kang, L. Pyeon, C. Lim, G. Y. Lee, T. Park and J. Choi, ACS Energy Lett, 2017, 2, 2667–2673.
- 22 M. Maiberg and R. Scheer, J Appl Phys, 2014, 116, 123710.
- 23 W. Melitz, J. Shen, A. C. Kummel and S. Lee, Surf Sci Rep, 2011, 66, 1–27.
- 24 N. S. Hill, M. V. Cowley, N. Gluck, M. H. Fsadni, W. Clarke, Y. Hu, M. J. Wolf, N. Healy, M. Freitag, T. J. Penfold, G. Richardson, A. B. Walker, P. J. Cameron and P. Docampo, Advanced Materials, 2023, 35, 2302146.
- 25 L. J. F. Hart, F. J. Angus, Y. Li, A. Khaleed, P. Calado, J. R. Durrant, A. B. Djurišić, P. Docampo and P. R. F. Barnes, Energy Environ Sci, DOI:10.1039/D4EE02669A.
- 26 N. E. Courtier, J. M. Cave, J. M. Foster, A. B. Walker and G. Richardson, Energy Environ Sci, 2019, 12, 396–409.
- 27 P. Calado, A. M. Telford, D. Bryant, X. Li, J. Nelson, B. C. O'Regan and P. R. F. Barnes, Nat Commun, 2016, 7, 1–10.
- 28 S. Van Reenen, M. Kemerink and H. J. Snaith, Journal of Physical Chemistry Letters, 2015, 6, 3808–3814.
- 29 F. J. Angus, W. K. Yiu, H. Mo, T. L. Leung, M. U. Ali, Y. Li, J. Wang, Anita. W. Y. Ho-Baillie, G. Cooke, A. B. Djurišić and P. Docampo, J Phys Chem Lett, 2024, 15, 10686–10695.
- 30 M. Khalid, M. Khan, K. Mahmood, M. Arshad, M. Imran, A. A. C. Braga and R. Hussain, Sci Rep, 2022, 12, 20220.

Chapter 4. n-Doping of Bio-Inspired Electron Transporting Materials: The Influence of Charge Transfer Complexation

This chapter has been adapted from *RSC Energy Adv.*, 2024, 3, 2939-2946. Acknowledge Dr. Dylan Wilkinson (University of Glasgow) and Dr. Michele Cariello (University of Glasgow) for materials synthesis and DFT calculations, Mr. Marcin Giza (University of Glasgow) for SEM measurements, as well as Dr. Stephen Sproules (University of Glasgow) for EPR measurements.

4.1. Introduction

This chapter explores the bio-inspired materials for PSCs, aiming to advance eco-friendly production methods and ensure biocompatibility. As part of this effort, this study investigates flavin-based derivatives as a bio-inspired electron transport material (ETM) in optoelectronic applications. Despite their potential, flavins often exhibit strong π – π stacking in solution, which can lead to aggregation. This behaviour negatively impacts film formation during solution deposition, resulting in poor film morphology and charge transport.¹. To address the aggregation problem, we have developed two bisfalvin (BF) analogues, one incorporating glycol (BFG) and the other alkyl side-chains (BFA), to improve their solubility in organic solvents.

However, organic semiconductors including these flavin derivatives face challenges of inherently lower conductivity due to their charge transport mechanism of hopping between localised molecular orbitals.² Meanwhile, due to structural disorder and impurities, organic semiconductors have the potential to form trap sites,3 which further hampers charge transport. These factors limit the development of novel organic semiconductors in optoelectronic applications. 4 Doping is a well-known approach to improve the performance of organic semiconductors. Molecular n-type dopants can significantly increase material conductivity, 5-8 improve film morphology, 9,10 and enhance the performance of electronic and optoelectronic devices. 11-18 For example, n-type doping has been used to increase the conductivity of PCBM derivatives from 10-8 S/cm to 10⁻³ S/cm by incorporating 4-(1,3-Dimethyl-2,3-dihydro-1H-benzoimidazol-2yl)phenyl)dimethylamine (N-DMBI), 19-21 further improving the performance of PSCs from

We explore two BF functionalised with glycol and alkyl side-chains, referred to as BFG and BFA, respectively (Figure 4.1), with an emphasis on understanding how glycol and alkyl side-chain influence doping kinetics and device performance. UV-vis spectroscopy, CV, and DFT modelling were used to investigate their optical and electronic properties. Conductivity measurements of the films with and without N-DMBI were performed, and PSCs incorporating BFG and BFA as ETMs were fabricated and characterised.

Figure 4.1. Structures of BFA and BFG

4.2. Results and Discussion

In Figure 4.2a, the optical properties of BFG and BFA exhibited similar UV-vis absorption spectra, indicating that the side-chains had no significant impact. CV measurements were used to investigate the redox properties of both BF derivatives (Figure 4.2b), as well as N-DMBI (Figure 4.2c). Both BF derivatives displayed two reduction waves, while N-DMBI was capable of oxidation to form a cation. These two redox waves correspond to sequential one-electron reductions, forming the radical anion (BF/ BF·⁻) and dianion states (BF·⁻/BF²⁻), respectively. The estimated electron affinities (EAs) of BF derivatives were determined to be at -4.17 eV (BFG) and -4.27 eV (BFA), indicating deeper energy levels compared to PCBM (-3.92 eV).²² DFT calculations were performed on simplified analogues of BFA and BFG, in which the alkyl groups were replaced with methyl units to facilitate the computational analysis. The calculated energy levels in gas phase were -6.70 eV (HOMO) and -4.07 eV (LUMO), respectively

(Figure 4.2d), aligning well with the CV measurements. These results confirm that BFG and BFA possess suitable energy levels to serve as effective electron acceptors for PSCs.^{23–25}

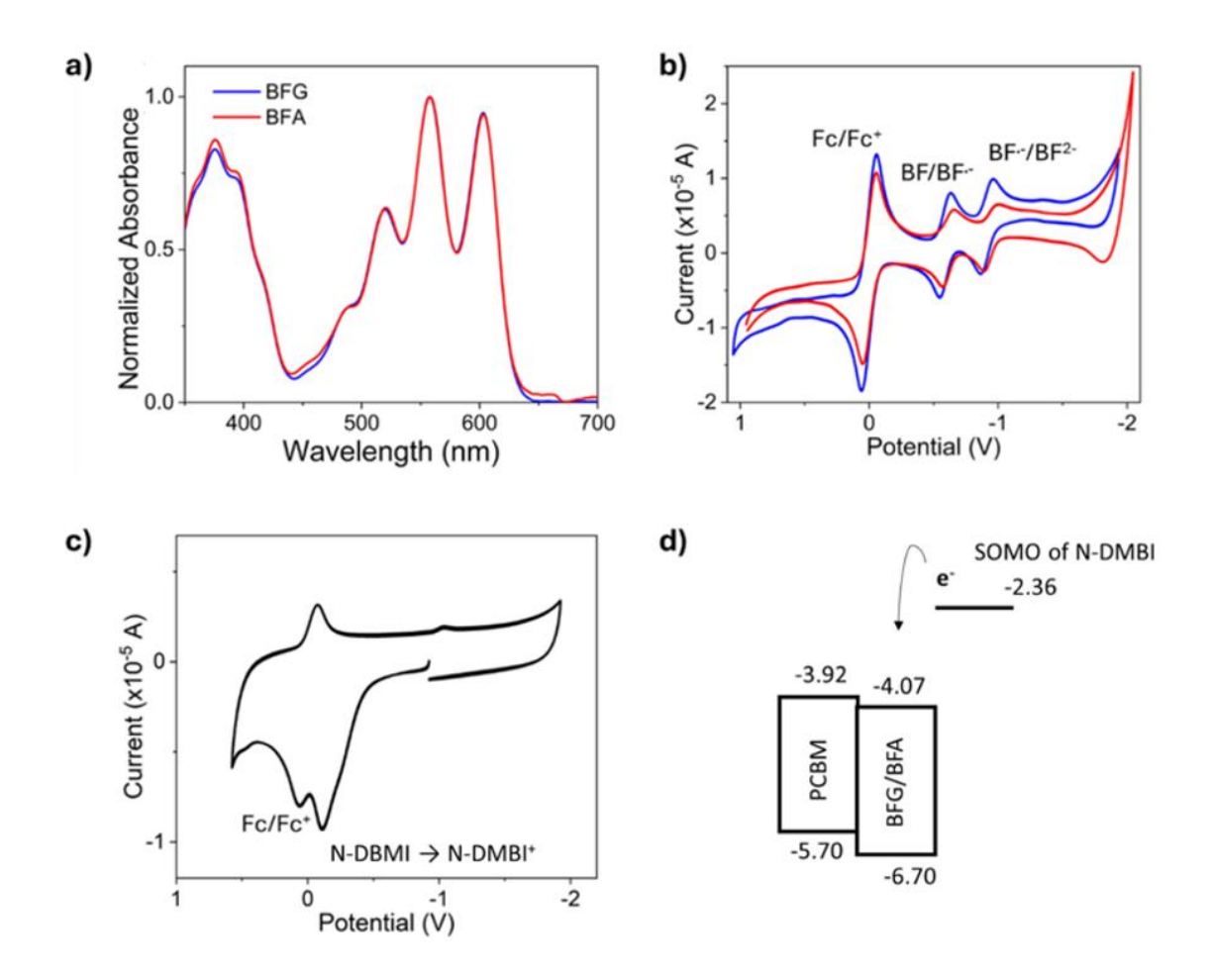


Figure 4.2. a) Solution state of UV-vis absorption spectra of BFG and BFA in solution (1 x 10⁻⁵ M in chlorobenzene); b) CV measurements of b) BFG and BFA, and c) N-DMBI (10⁻³ M in DMF, scan rate 100 mV/s) using ferrocene as the reference, a glassy carbon working electrode, a Pt wire reference electrode and a coiled Ag wire counter electrode. All redox processes are recorded by selecting a wide process window; and d) Energy levels of PCBM, BF derivatives and N-DMBI (HOMO/LUMO of BF derivatives calculated from DFT of BF)

N-DMBI was selected as the n-type dopant to enhance the conductivity of the BF derivatives. N-DMBI can effectively promote the reduction transformation of organic materials²⁶ and facilitating radical species formation.^{27,28} The HOMO level of N-DMBI is -

4.67 eV, lower than the LUMO levels of PCBM and BF derivatives. Consequently, direct electron transfer between N-DMBI and BF derivatives is not feasible due to energy level misalignment.^{26,29} However, a photochemical³⁰ or thermal processes^{30,31} is required to activate N-DMBI to form a radical with singly occupied molecular orbital (SOMO) of -2.36 eV,²⁶ thereby allowing the electron transfer to BF derivatives.

To better understand the effects of BF derivatives on N-DMBI addition, a series of UV-vis absorption measurements was used to analyse the effects on N-DMBI concentration and reaction kinetics in Figure 4.3. Upon introducing the N-DMBI and applying heat, both BF derivatives showed a new reduction peak at 675 nm, indicating the formation of charge species, as shown in Figure 4.3a and 4.3b.³² The intensity of this peak increased with higher N-DMBI concentration, suggesting a shift in equilibrium toward the product side and a more pronounced doping reaction at elevated dopant levels. This behaviour can be explained by Le Châtelier's principle: as the reactant concentration increases, more reactant molecules are available, leading to more frequent effective collisions between BF and N-DMBI. Consequently the forward reaction proceeds more rapidly, resulting in greater product formation.

To ensure complete reaction, a 100 mol% N-DMBI (1:1 ratio) was added on BFG and maintained at 70°C for 24 hours (Figure 4.3c and 4.3d). Heating was essential to activate the reaction for these molecules. ²⁶ The appearance of the 675 nm peak within 2 hours confirmed the charged species formation. Interestingly, the progression varied between BFG and BFA, with BFG reaching its peak intensity within 3 hours, whereas BFA required 6 hours. This difference suggests that the charged species of BFG glycol sidechain are formed faster than those of BFA alkyl side-chains. This acceleration is likely due to the glycol moiety creating a polar environment that enhances miscibility between the BFG and N-DMBI for further reaction. As a results, BFG exhibits better compatibility with N-DMBI molecules, facilitating a more efficient doping process than BFA.

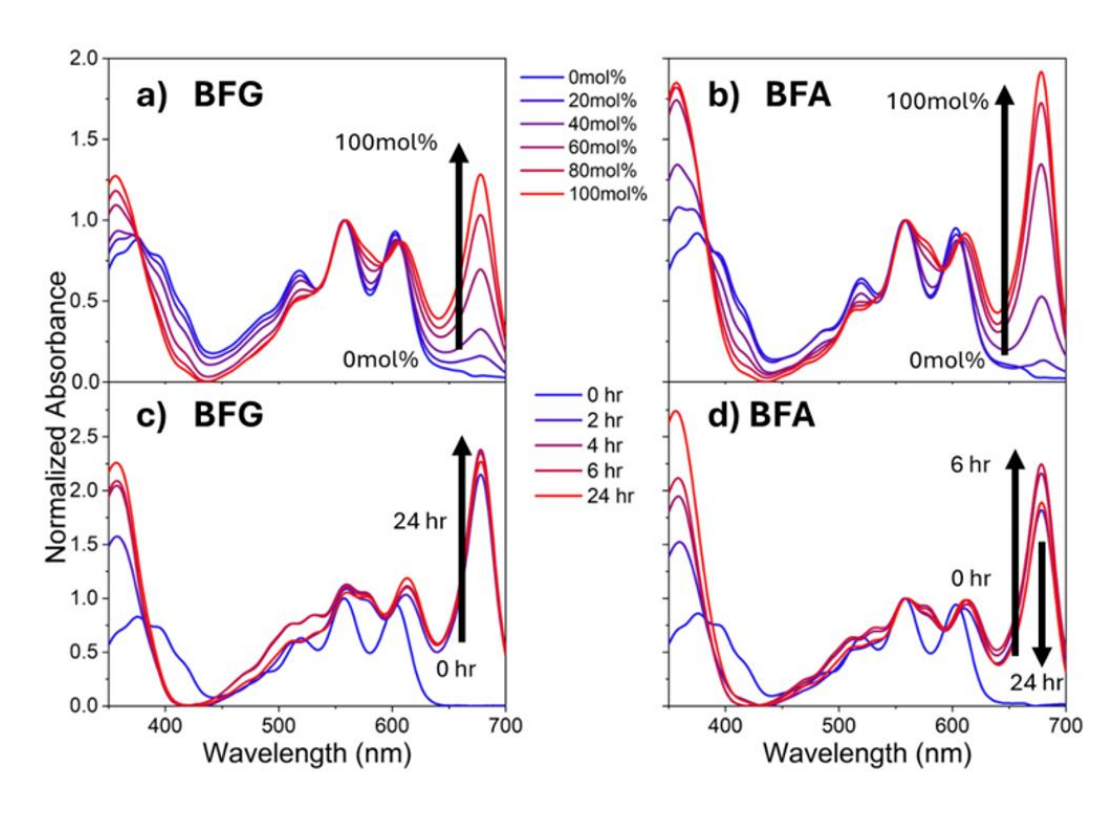


Figure 4.3. UV-vis absorption spectra of a) BFG and b) BFA in the presence of 0 mol% to 100 mol% N-DMBI; c) BFG and d) BFA with reaction times from 0 to 24 hours (Normalized at 558 nm, corresponding to one of the typical absorption peaks of pristine BF materials)

Electron paramagnetic resonance (EPR) measurements were performed to confirm the formation of radical species, as shown in Figure 4.4. Upon the addition of 20 mol% N-DMBI to both BF derivatives, a strong paramagnetic signal with a g value of 2.003 was observed, indicating the presence of radical anions. On the other hand, pristine BFG and BFA samples did not show the free radical signal (Figures 4.5a and b). The enhanced ESR signal in BFG and BFA with N-DMBI addition suggests a higher concentration of radical anions, resulting from electron transfer from N-DMBI to BF derivatives. This process generates an unpaired electron in BFG and BFA, forming a free radical anion detectable by ESR. However, UV-vis absorption measurement revealed that the radical anion of BFG is more stable than that of BFA. Over 24 hours, the intensity of the absorption peak at 675 nm for BFG remained unchanged, whereas the corresponding peak for BFA decreased significantly. These findings highlight the relationship between the molecular side chain, reaction kinetics, and stability, emphasising the importance of side chain choice in the doping process.

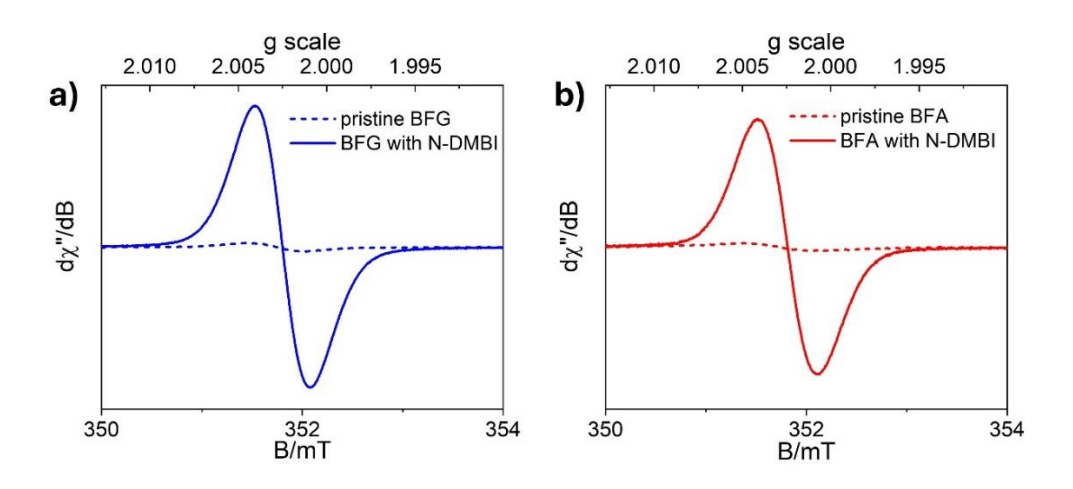


Figure 4.4. EPR spectrum of a) BFG and b) BFA with and without N-DMBI in chlorobenzene ($\sim 2 \times 10^{-2} \text{ M}$)

To assess their potential as ETM in solar cells, the conductivity measurements were performed by extracting values from resistance measurements using standard current–voltage (I-V) curves (Figure 4.5a). Both BF derivatives exhibited similar conductivity values of $\sim 5.6 \times 10^{-7}$ S/cm, which is slightly higher than PCBM ($\sim 6.75 \times 10^{-8}$ S/cm, measured in our laboratory and consistent with reported values^{5,19,33}). It suggests that BF derivatives are potential as ETLs in optoelectronic devices.

To further understand radical formation in thin films, we performed UV-vis absorption measurements on flavin derivatives with and without N-DMBI to investigate the impact on film structure. The films were prepared by spin coating under the same conditions used for fabricating the TC PSCs, as illustrated in Figure 4.5a. A 20 mol% N-DMBI concentration was chosen based on our solution-phase data (Figure 4.3) under annealing for 3 hours (BFG) and 6 hours (BFA), which indicated significant radical anion formation and prepared the film by the spin coating under the same conditions as the solar cell devices. The spin-coated thin films exhibited new absorption peaks at 690 nm for BF derivatives, consistent with the solution-phase findings. The broad nature of these peaks may be influenced by packing effects induced by the dopants. The variations in absorption intensity are attributed to differences in film quality resulting from the spin coating process. In particular, the high intensity observed around 700 nm for the BFA film with N-DMBI is likely due to increased film thickness. However, the radical peak position for BFA with N-DMBI remains the same as that for BFG with N-DMBI. The conductivity

measurements showed minimal improvement doping, increasing only slightly from 5.6 x 10^{-7} S/cm for the pristine BFG and BGA to 1.08×10^{-6} S/cm of BFG and 8.80×10^{-7} S/cm for BFA after N-DMBI addition. This limited increase in conductivity is unexpected, as addition of chemical dopants typically enhance conductivity by several orders of magnitude in state-of-the-art organic semiconductors. The results indicate that the BF radical anion formed in the films are unable to efficiently transfer electrons into the matrix.

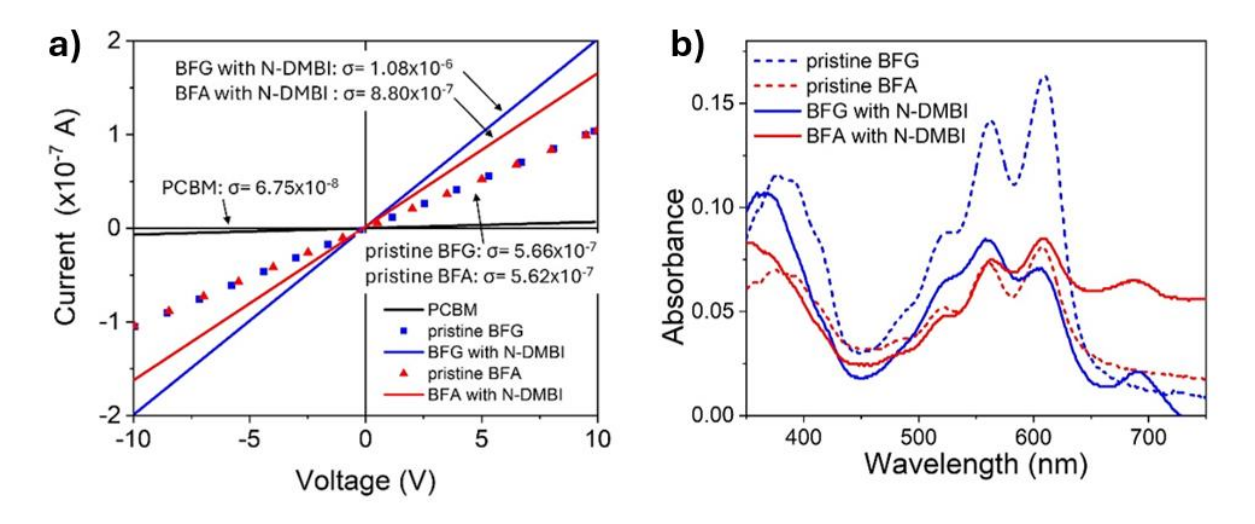


Figure 4.5. a) Conductivity measurement of BFG and BFA with and without N-DMBI on ITO substrates and b) Solid state UV-vis absorption spectra on glass

To assess the viability of BF derivatives as ETLs, we fabricated PSCs with glass/ITO/MeO-2PACz/Al $_2$ O $_3$ NPs/perovskite/ETL/BCP/Ag. Figure 4.6 compares the J-V characteristic of PCBM and BF-based devices, and photovoltaic parameters are summarised in Table 4.1. Pristine BF devices exhibited comparable Jsc and Voc to PCBM-based devices while the FF were lowered, ranging from 0.36 to 0.38 compared to 0.79 for PCBM-based devices.

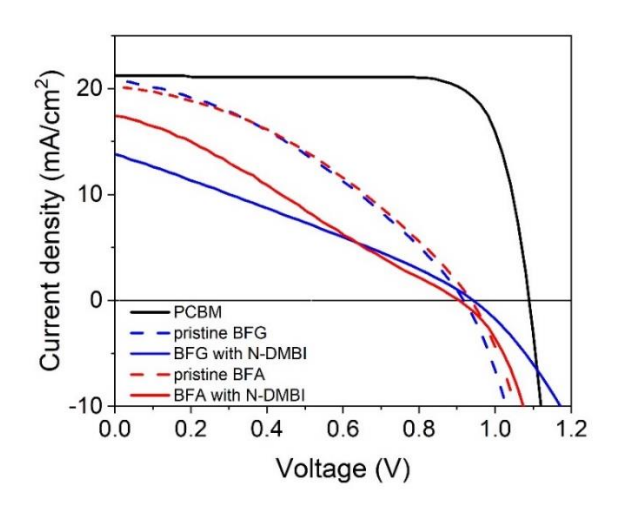


Figure 4.6. J-V characteristics curves of champion devices based on PCBM, BFG and BFA PSCs

Table 4.1. Photovoltaic performance of PCBM and BF-based PSCs (10 devices for each condition)

ETL	N-DMBI (mol%)	Jsc(mA/cm²)	Voc (V)	FF	PCE (%)
PCBM	/	21.19 ± 0.16	1.09 ± 0.00	0.79 ± 0.02	18.26 ± 0.45
BFG	0	20.81 ± 0.42	0.92 ± 0.03	0.36 ± 0.01	6.95 ± 0.48
	20	13.82 ± 1.08	0.94 ± 0.10	0.28 ± 0.00	3.69 ± 0.16
BFA	0	20.22 ± 0.58	0.94 ± 0.14	0.38 ± 0.02	7.11 ± 1.19
	20	17.45 ± 1.22	0.91 ± 0.07	0.28 ± 0.02	4.38 ± 0.34

The JV curve analysis indicates that pristine BF derivatives exhibit higher series resistance compared to PCBM, as evidenced by the steeper slop on the Voc side observed for PCBM relative to the BF derivatives, as shown in Figure 4.6. The increased resistance observed in BF-based devices is attributed to their intrinsically low conductivity rather than π - π stacking effects alone. While π - π stacking can enhance charge transport, as demonstrated by Ma *et al.*³⁷ and Zheng *et al.*³⁸, who demonstrated enhanced conductivity and PCE through stronger π - π stacking. In some cases, disorder may occur between domain, which may hinder charge transport. This could explain the low conductivity observed in the pristine form. We note the lower conductivity of the flavin derivatives reported here, especially in comparison to PCBM.

During fabrication, samples were taken out from a nitrogen-filled glovebox to the evaporator exposed to ambient conditions. While PCBM exhibits a significant increase in conductivity owing to self-doping upon air expose from 6.75×10^{-8} S/cm to 1.58×10^{-6} S/cm (Figure 4.7), the BF derivatives do not carry out dopant-based doping or self-doping. As a result, they exhibit higher resistance and lower photovoltaic performance. SEM analysis of PCBM and BF films (Figure 4.8) revealed no observable morphological differences between PCBM and pristine BF derivatives. This confirm that high resistance in BF devices stems from their intrinsic low conductivity rather than solely to their π - π stacking behaviour.

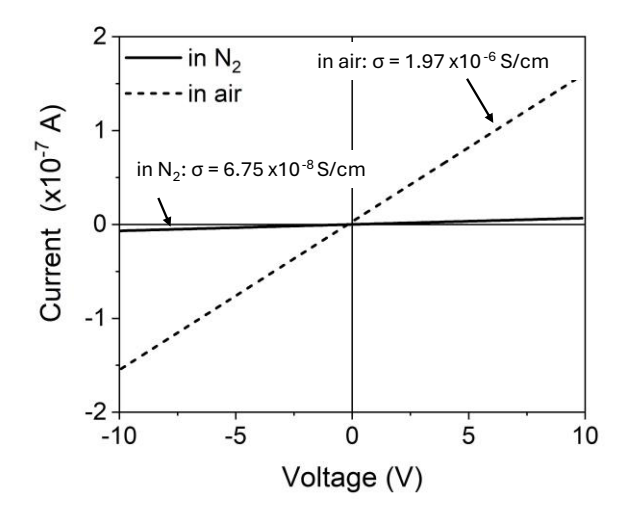


Figure 4.7. Conductivity measurements of pristine PCBM films exposed in N_2 and air on ITO substrates

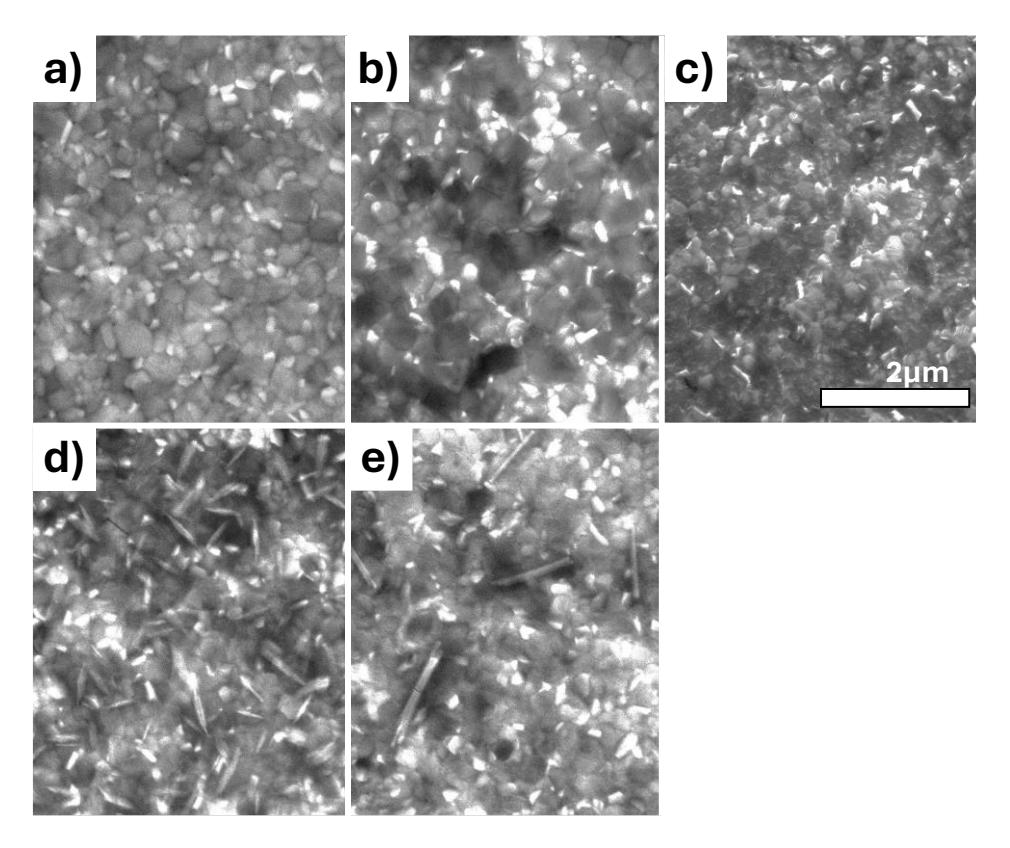


Figure 4.8. SEM images of a) PCBM, b) pristine BFG, c) pristine BFA, d) BFG and e) BFA with 20 mol% N-DMBI addition

Similarly to lack of charge transport enhancement extracted from the conductivity measurements, the addition of dopant also did not improve the performance of the fabricated solar cells. Indeed, devices incorporating both BFG and BFA that include the dopant did not increase the performance but rather led to reduction in the PCE, as compared to their pristine counterparts. While the Voc remained unchanged at 0.9 V for both BF devices, the Jsc of the devices reduced significantly from 20.81 mA/cm² for pristine BFG and 20.22 mA/cm² for pristine BFA to 13.82 mA/cm² for BFG with N-DMBI addition and 17.45 mA/cm² for BFA with N-DMBI addition, respectively. Additionally, the FF dropped from a range of 0.36-0.38 to 0.28 following N-DMBI addition. The reduced Jsc and FF is attributed to the influence of N-DMBI.^{26,35} The formation of needle shaped features in BF derivatives with N-DMBI, as observed in Figure 4.8, suggests that N-DMBI may affect the molecular packing or induce aggregation within the system, similar to behaviours observed in systems with PCBM ^{19,40}, where over doping of PCBM also reduces Jsc and FF, and naphthalenediimide⁴¹, leading to aggregation-related loss. Additionally, the presence of N-DMBI may introduce charge carrier traps, ⁴² increasing recombination

and further degrading device performance. This is supported by the increased series resistance observed in the JV curves of N-DMBI incorporated devices compared to their pristine counterparts (Figure 4.6).

Interestingly, despite the BF radical anion formation being proved by EPR measurements, the N-DMBI addition does not result in increased film conductivity. To investigate this unexpected result, we hypothesised that another charged species, a charge-transfer complex (CTC), was formed during the process instead of the formation free radical. If the electron remains bound within the CTC rather than being transferred to an adjacent neutral BF molecule, doping would be ineffective in enhancing the film's conductivity.

To examine this hypothesis, DFT model calculations were performed on the radical anion [BF \cdot] and [BF/N-DMBI] \cdot complex, as shown in Figure 4.9. The spin density map of the [BF \cdot] shows the presence of highly delocalised radical throughout the acceptor core, suggesting the formation of a stabilised radical. However, DFT calculations indicate that the LUMO level of BF is -4.07 eV, which is significantly shallower than that of [BF/N-DMBI] \cdot complex (-4.21 eV). This energy difference suggests that electron transfer from the CTC to neutral BF unit is energetically unfavourable.

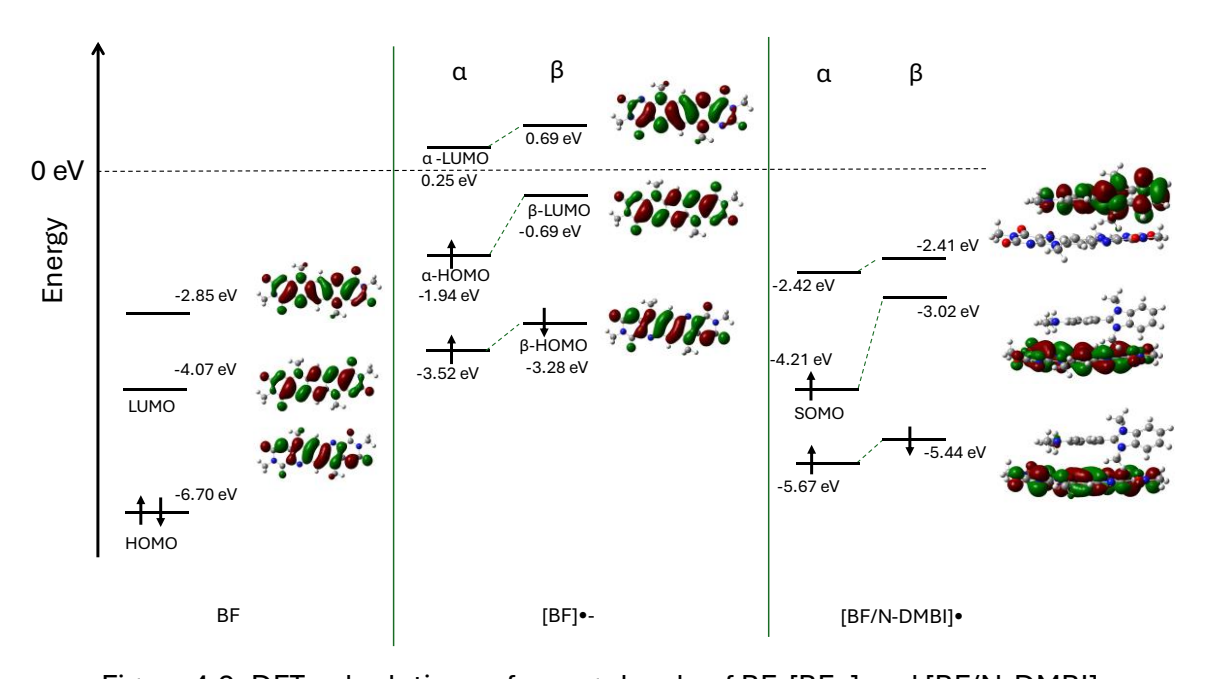


Figure 4.9. DFT calculations of energy levels of BF, [BF.] and [BF/N-DMBI].

Further evidence for CTC formation comes from TD-DFT of the predicted UV-vis absorption spectra of [BF/N-DMBI]· complex (Figure 4.10). A comparison with experimental spectra of CTC revealed similar spectral features, including a reduction peak at 675 nm, while the TD-DFT predicted peak was at 644 nm. The slight discrepancy can be attributed to gas-phase conditions in the calculations. Meanwhile, the absorption peaks at 350 nm, 550 nm and 600 nm observed for BF align with the simulated BF peak at 350 nm and the broad absorption feature around 550 nm.

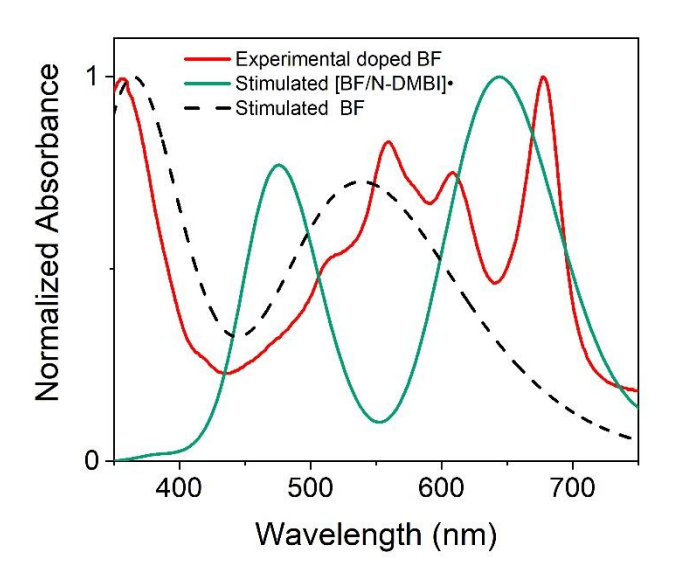


Figure 4.10. TD-DFT simulated UV-Vis spectra of neutral of BF and [BF/N-DMBI].

Additional support was provided by electrostatic potentials (ESPs) (Figure 4.11a), which shows that N-DMBI and BF derivatives have positive (light blue) and negative (red) potentials, respectively. The negative charge is located on the latter's more electronegative oxygen and nitrogen atoms. The spin density maps of the CTC (Figure 4.11b) shows highly delocalised radicals on the BF unit. Mulliken charge population analysis performed on [BF/N-DMBI]· indicated a high degree of charge transfer between the components of the complex (0.9 e). ²⁹ Lastly, the binding energies of [BF/N-DMBI]· (-53.1 kcal/mol) was substantially stronger than that of the π - π dimer of BF (-6.9 kcal/mol). The stronger binding in the CTC is expected to disrupt long-range π - π stacking, thereby significantly reducing electron mobility in the films (Figure 4.12).

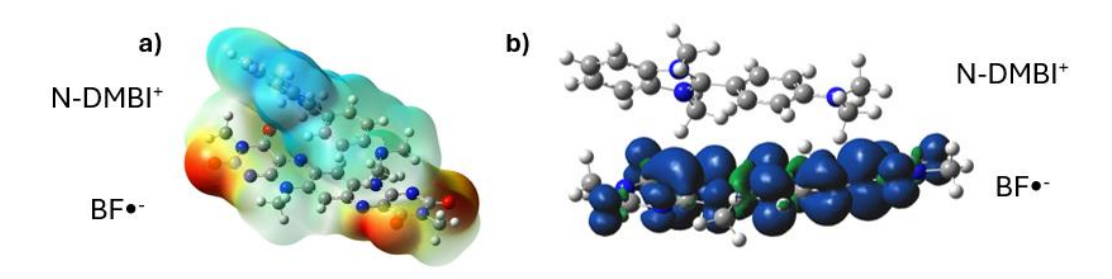


Figure 4.11. a) ESP and b) spin density maps of [BF/N-DMBI].

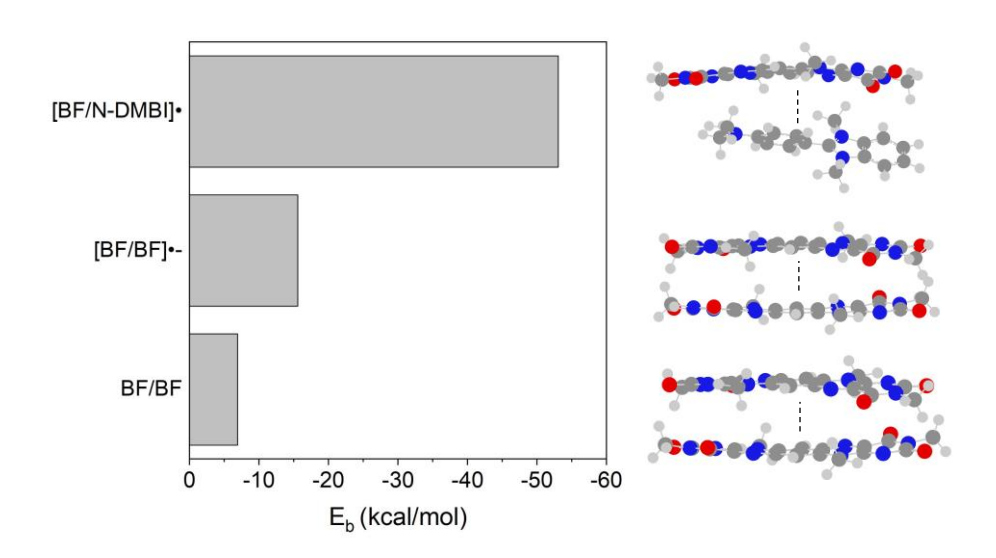


Figure 4.12. Calculated binding energies for [BF/N-DMBI], [BF/BF] and BF/BF

4.3. Conclusions

This study explored the bioinspired derivatives as ETMs for PSCs. In their pristine form, these materials exhibited the PCEs of 7% along with competitive Jsc and Voc values. We also investigated the feasibility of n-type doping for BFG and BFA. While ESR and UV-vis absorption measurements confirmed radical formation during the process, conductivity measurements revealed no significant enhancement in charge transport and indicated detrimental effects on photovoltaic performance. To understand this limitation, we employed DFT calculations, which provided insight into the mechanism, indicating that these materials form stable CTCs during the process. The calculations showed an energetic misalignment between the SOMO of the [BF/N-DMBI]· complex and the LUMO of pristine BF derivatives. Consequently, electron donation from complex to the pristine molecules is unlikely, consistent with conductivity measurements that showed no change, remaining at approximately 10-7 S/cm before and after N-DMBI

addition. Therefore, our finding suggests that addition with N-DMBI is not an effective strategy for the BF systems, as charge-transfer complexation may hinder the electron transport. This study underscores the importance of leveraging cost-effective DFT calculations early in the design process to evaluate new ETMs for doping behaviour and to optimise performance.

4.4. References

- 1 D. Wang, T. Ye and Y. Zhang, *J Mater Chem A Mater*, 2020, **8**, 20819–20848.
- 2 W. Brütting and C. Adachi, *Physics of Organic Semiconductors*, Wiley-VCH Verlag GmbH & Co. KGaA, 2005.
- 3 K. Pei, Surfaces and Interfaces, 2022, **30**, 101887.
- 4 J. Lian, B. Lu, F. Niu, P. Zeng and X. Zhan, *Small Methods*, 2018, **2**, 1800082.
- 5 L. Hu, T. Liu, J. Duan, X. Ma, C. Ge, Y. Jiang, F. Qin, S. Xiong, F. Jiang, B. Hu, X. Gao, Y. Yi and Y. Zhou, *Adv Funct Mater*, 2017, 27, 1703254.
- Z. Wang, D. P. McMeekin, N. Sakai, S. van Reenen, K. Wojciechowski, J. B. Patel, M. B. Johnston and H. J. Snaith, *Advanced Materials*, 2017, 29, 1604186.
- Q. Q. Ye, Z. K. Wang, M. Li, C. C. Zhang, K. H. Hu and L. S. Liao, ACS Energy Lett, 2018,
 3, 875–882.
- 8 X. Zhao, D. Madan, Y. Cheng, J. Zhou, H. Li, S. M. Thon, A. E. Bragg, M. E. DeCoster, P. E. Hopkins and H. E. Katz, *Advanced Materials*, 2017, **29**, 1606928.
- 9 I. E. Jacobs and A. J. Moulé, *Advanced Materials*, 2017, **29**, 1703063.
- 10 H. Xia, M. Zhang, H. Wang, Y. Sun, Z. Li, R. Ma, H. Liu, T. A. Dela Peña, H. T. Chandran, M. Li, J. Wu, X. Lu, W. Y. Wong and G. Li, Adv Funct Mater, 2024, 2411058.
- 11 Y. Xu, H. Sun, A. Liu, H. H. Zhu, W. Li, Y. F. Lin and Y. Y. Noh, *Advanced Materials*, 2018, **30**, 1801830.
- 12 K. Pei, A. Ho, Y. Lau, P. Kwok and L. Chan, *Phys. Chem. Chem. Phys*, 2020, **22**, 7100–7109.
- 13 Z.-C. Wen, H. Yin and X.-T. Hao, Surfaces and Interfaces, 2021, 23, 100921.
- 14 H.-T. Chien, M. Pölzl, G. Koller, S. Challinger, C. Fairbairn, I. Baikie, M. Kratzer, C. Teichert and B. Friedel, *Surfaces and Interfaces*, 2016, **6**, 72–80.
- 15 Y. Liu, B. Nell, K. Ortstein, Z. Wu, Y. Karpov, T. Beryozkina, S. Lenk, A. Kiriy, K. Leo and S. Reineke, *ACS Appl Mater Interfaces*, 2019, **11**, 11660–11666.
- 16 X. Lin, B. Wegner, K. M. Lee, M. A. Fusella, F. Zhang, K. Moudgil, B. P. Rand, S. Barlow, S. R. Marder, N. Koch and A. Kahn, *Nat Mater*, 2017, **16**, 1209–1215.
- 17 W. Zhao, J. Ding, Y. Zou, C. A. Di and D. Zhu, *Chem Soc Rev*, 2020, **49**, 7210–7228.
- 18 E. Hyun Suh, Y. Jin Jeong, J. Gyu Oh, K. Lee, J. Jung, Y. Soo Kang and J. Jang, *Nano Energy*, 2019, **58**, 585–595.
- 19 S. Kim, S. Bae and H. Jo, Chem. Commun, 2015, **51**, 17413.

- 20 Z. Bin, J. Li, L. Wang and L. Duan, *Energy Environ Sci*, 2016, **9**, 3424–3428.
- 21 F. Galatopoulos, S. Bitton, M. Tziampou, N. Tessler and S. A. Choulis, *ACS Appl Electron Mater*, 2023, **5**, 5580–5587.
- 22 P. Reiser, F. S. Benneckendorf, M. M. Barf, L. Müller, R. Bäuerle, S. Hillebrandt, S. Beck, R. Lovrincic, E. Mankel, J. Freudenberg, D. Jänsch, W. Kowalsky, A. Pucci, W. Jaegermann, U. H. F. Bunz and K. Müllen, *Chemistry of Materials*, 2019, 31, 4213–4221.
- 23 Y. Shao, Y. Yuan and J. Huang, *Nat Energy*, 2016, **1**, 15001.
- 24 J. Y. Jeng, Y. F. Chiang, M. H. Lee, S. R. Peng, T. F. Guo, P. Chen and T. C. Wen, *Advanced Materials*, 2013, **25**, 3727–3732.
- 25 L. Zhou, J. Chang, Z. Liu, X. Sun, Z. Lin, D. Chen, C. Zhang, J. Zhang and Y. Hao, Nanoscale, 2018, 10, 3053.
- 26 P. Wei, J. H. Oh, G. Dong and Z. Bao, *J Am Chem Soc*, 2010, **132**, 8852–8853.
- 27 D. D. Tanner, J. J. Chen, L. Chen and C. Luelo, *JAm Chem Soc*, 1991, **113**, 8074–8081.
- 28 D. D. Tanner and J. J. Chen, *Journal of Organic Chemistry*, 1989, **54**, 3842–3846.
- 29 Y. Zeng, W. Zheng, Y. Guo, G. Han and Y. Yi, *J. Mater. Chem .A*, 2020, **8**, 8323–8328.
- 30 O. Bardagot, C. Aumaître, A. Monmagnon, J. Pécaut, P. A. Bayle and R. Demadrille, *Appl Phys Lett*, 2021, **118**, 203904.
- 31 S. Riera-Galindo, A. Orbelli Biroli, A. Forni, Y. Puttisong, F. Tessore, M. Pizzotti, E. Pavlopoulou, E. Solano, S. Wang, G. Wang, T. P. Ruoko, W. M. Chen, M. Kemerink, M. Berggren, G. Di Carlo and S. Fabiano, ACS Appl Mater Interfaces, 2019, 11, 37981–37990.
- 32 Y. Yano, M. Nakazato, Kenzo Lizuka, T. Hoshino, K. Tanaka, M. Kogab and F. Yoneda, *J. Chem. Soc., Perkin Trans. 2*, 1990, **2**, 2179–2185.
- 33 J. Li, F. Qin, W. Zeng, L. Sun, W. Wang and Y. Zhou, *Sustain Energy Fuels*, 2020, **4**, 1984–1990.
- 34 Z. Wang, D. P. McMeekin, N. Sakai, S. van Reenen, K. Wojciechowski, J. B. Patel, M. B. Johnston and H. J. Snaith, *Advanced Materials*, 2017, **29**, 1604186.
- 35 X. Liu, P. Li, Y. Zhang, X. Hu, Y. Duan, F. Li, D. Li, G. Shao and Y. Song, *J Power Sources*, 2019, **413**, 459–466.
- 36 M. Koopmans, M. A. T. Leiviskä, J. Liu, J. Dong, L. Qiu, J. C. Hummelen, G. Portale, M.C. Heiber and L. J. A. Koster, ACS Appl Mater Interfaces, 2020, 12, 56222–56230.

- Q. Ma, J. Qiu, Y. Yang, F. Tang, Y. Zeng, N. Ma, B. Yu, F. Lu, C. Liu, A. Lambertz, W. Duan,K. Ding and Y. Mai, *Journal of Energy Chemistry*, 2023, 82, 25–30.
- 38 A. Zheng, J. Wang, N. Xu, R. Zhu, Y. Yuan, J. Zhang, J. Zhang, Z. Li and P. Wang, *ACS Photonics*, 2018, **5**, 4694–4701.
- 39 B. Vella, M. H. Fsadni, T. Pope, M. Giza, F. J. Angus, I. Shmarov, P. L. Lalaguna, M. Cariello, C. Wilson, M. Kadodwala, T. J. Penfold, P. Docampo and G. Cooke, *J Mater Chem A*, 2024, **12**, 22844–22858.
- 40 J. H. Bae, Y. J. Noh, M. Kang, D. Y. Kim, H. Bin Kim, S. H. Oh, J. M. Yun and S. I. Na, *RSC Adv*, 2016, **6**, 64962–64966.
- 41 D. Kiefer, A. Giovannitti, H. Sun, T. Biskup, A. Hofmann, M. Koopmans, C. Cendra, S. Weber, L. J. Anton Koster, E. Olsson, J. Rivnay, S. Fabiano, I. McCulloch and C. Müller, ACS Energy Lett, 2018, 3, 278–285.
- 42 M. N. Le, H. Kim, B. Yeo, K. Kang, Y. Song, X. Guo, Y.-G. Ha, C. Kim and M.-G. Kim, *J. Mater. Chem. C*, 2019, **7**, 10635–10641.

Chapter 5. Influence of Imide Side-chain Functionality in the Doping Characteristics of Naphthalenediimide Derivatives as Electron Transport Materials

This chapter has been accepted for publication in *Physical Chemistry Chemical Physics*. Acknowledge Dr. Lewis Mackenzie (University of Glasgow) and Dr. Dylan Wilkinson (University of Glasgow) for materials synthesis and DFT calculations, Mr. Marcin Giza (University of Glasgow) for SEM measurements, as well as Dr. Stephen Sproules (University of Glasgow) for performing EPR measurements.

5.1. Introduction

Doping is a proven strategy to improve the electrical properties of organic materials by generating free charges through interactions between dopant and the host materials. This approach has been particularly successful in fullerene-based electron transport materials (ETMs), such as C60 and phenyl-C61-butyric acid methyl ester (PCBM), where conductivities exceeding 10 S/cm have been achieved. In the meantime, there is growing interest in non-fullerene alternatives such as naphthalenediimide (NDI) derivatives due to their simpler synthesis route, tunable energy levels and potential for reducing chemical usage, energy consumption, and production costs. Although n-type doping has increased NDI conductivity up to 10-1 S/cm, the underlying mechanism of ion pair formation and charge transfer complexation remain poorly understood.

In this chapter, we introduced NDI as another class of non-fullerene ETMs. These molecules exhibit strong π – π stacking interactions, which often lead to aggregation issues. To mitigate this, functional groups have been incorporated into PDI and NDI derivatives to improve solubility and reduce aggregation. There have been studies exploring how side-chains influence doping reactions. For instance, Liu *et al.* demonstrated that the polarity and the length of glycol side-chain in fullerene derivatives impact performance in n-type organic thermoelectric materials, while Vijayakumar *et al.* studied the effect of alkyl side-chain length on doping kinetics and charge transport properties in poly(2,5-bis(3-alkylthiophen-2-yl)thieno[3,2-b]thiophene) (PBTTT) films. However, a systematic investigation of how different side-chains affect the reactivity between host molecules and molecular dopants is still lacking. Further research is

needed to understand how specific synthetic modifications, particularly the choice of side-chains, not only enhance solubility in solvent, but also influence the local doping environment and control the doping behaviour.

In this study, we have developed two NDI-based molecules functionalised with ethylene glycol (NDI-G) and ethylhexyl (NDI-EtHx) imide side-chains. While both improve solubility in organic solvents, they exhibit distinct reaction when addition of 4-(1,3-Dimethyl-2,3-dihydro-1H-benzoimidazol-2-yl)phenyl)dimethylamine (N-DMBI) as the n-type dopant. Using UV-vis absorption spectroscopy, CV measurements, and DFT calculations, we investigated the undoped and doped states of these NDI derivatives, along with their conductivities. Our findings reveal that NDI-G undergoes a more effective doping reaction with N-DMBI, resulting in faster doping reaction times and higher conductivity. We attribute this to the polar glycol side-chains, which facilitate charge-transfer complexation with N-DMBI. Lastly, we incorporate NDI-G and NDI-EtHx as ETLs in PSCs, demonstrating that the choice of side-chain significantly influences device performance, ultimately improving optoelectronic properties.

5.2. Results and Discussion

In this chapter, we explore how the electrostatic environment surrounding NDI derivatives affects doping efficiency when using with the N-DMBI. We hypothesise that manipulating the polarity of side-chains attached to the NDI core can modulate the distance between the N-DMBI and NDI derivatives, thereby influencing the doping reaction. To test this, we functionalised the NDI derivatives with two distinct side-chains: an ethylene glycol chain in NDI-G to create a more polar environment, and an ethylhexyl chain in NDI-EtHx to establish a less polar environment.

The chemical structures of NDI-G, NDI-EtHx, along with that of N-DMBI, are presented in Figure 5.1a. The optical properties of these derivatives were characterised using UV-vis absorption spectroscopy to assess how side-chain functionalisation affects their light absorption behaviour. As shown in Figure 5.1b, both compounds display nearly identical absorption spectra, indicating that the side-chain variations do not affect the optical performance of the molecules in their neutral state.

To further investigate their electronic behaviour, we used CV to determine the redox properties of NDI-G and NDI-EtHx in solution (Figure 5.1c). Both NDI derivatives show two pseudo-reversible reduction waves, benchmarked against ferrocene as internal reference. These redox transitions correspond to successive one-electron reductions, forming radical anion and dianion. The calculated electron affinities (EAs) of NDI-G and NDI-EtHx are -3.67 eV and -3.70 eV, respectively, which are shallower than that of PCBM (-3.92 eV).¹¹

To simplify the convergence of geometry optimisation, the alkyl group of NDI-G and NDI-EtHx were truncated to methyl group (methyl-NDI) in DFT calculations. This adjustment is justified by minimal influence side-chains generally exert on the electronic properties of the NDI core. 12 The gas phase energy levels for methyl-NDI were calculated to be -7.22 eV (HOMO) and -3.56 eV (LUMO) in Figure 5.1d. When compared with CV results, this confirms that NDIs possess energy levels similar to those of fullerenes derivatives, suggesting that NDI-G and NDI-EtHx could serve in similar range of optoelectronic applications due to favourable energy level alignment. Lastly, the conductivity of pristine NDI derivatives was measured using standard current-voltage measurements on patterned-ITO substrates, with the device structure (glass/ITO/NDI) and patterning shown in Figure 3.3a. The conductivity of both NDI derivatives is about 10⁻⁷ S/cm, which is lower than that of PCBM (1.58x10⁻⁶ S/cm), as shown in Figure 5.1e. These results highlight the need for effective doping strategies to boost the electrical properties of NDI-based materials for potential applications.

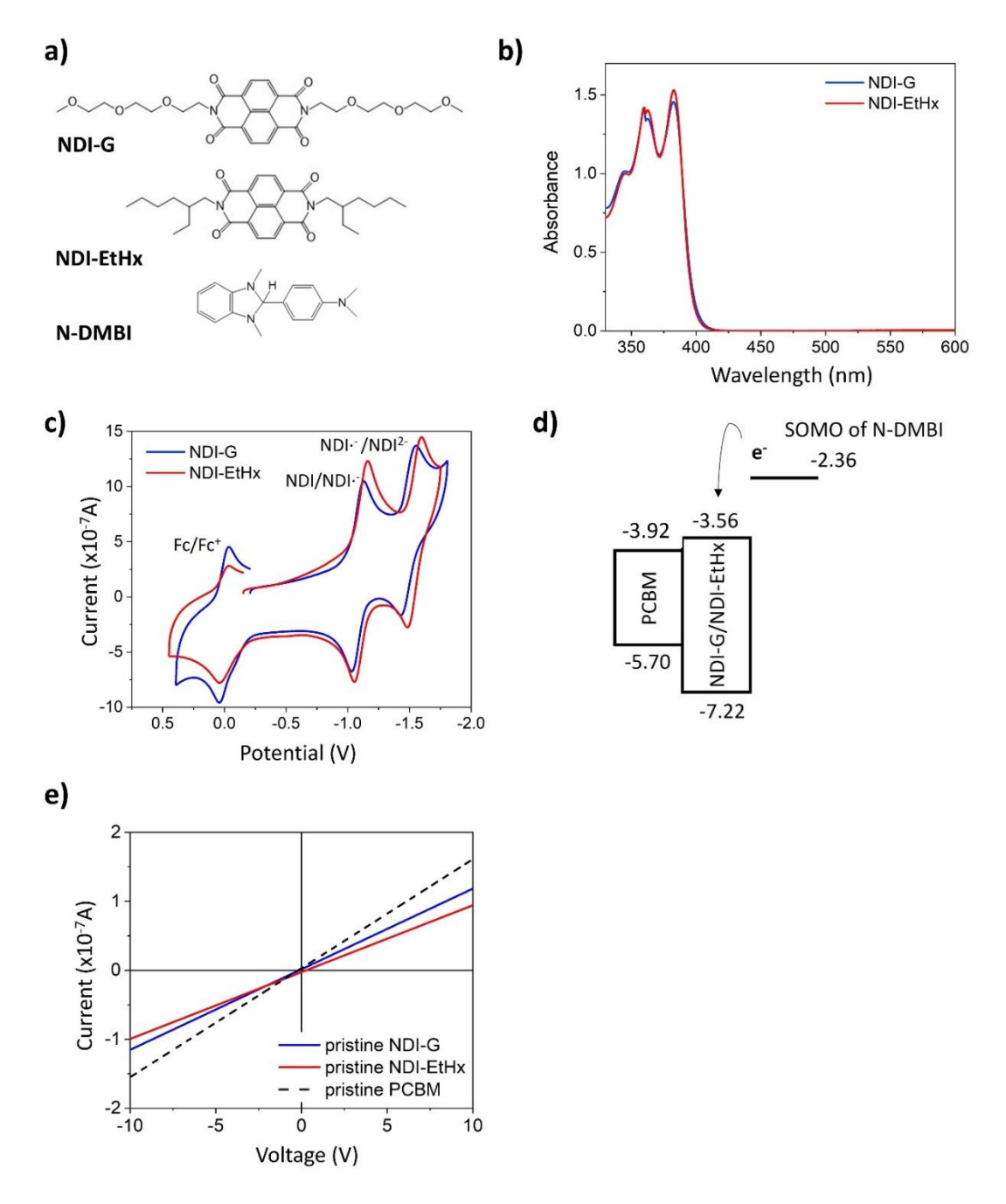


Figure 5.1. a) Structures of NDI-G, NDI-EtHx and N-DMBI; b) UV-vis absorption spectra of pristine NDI-G and NDI-EtHx in solution (1 x 10⁻⁵ M in chlorobenzene); c) CV measurements of NDI-G and NDI-EtHx (1 x 10⁻⁴ M in CH₂Cl₂; scan rate 0.1 mV/s) using ferrocene as the reference, a glassy carbon working electrode, a Pt wire reference electrode and a coiled Ag wire counter electrode. All redox processes are recorded by selecting a wide process window; d) Energy levels of PCBM, methyl-NDI and N-DMBI (HOMO and LUMO levels of methyl-NDI obtained from DFT calculations) and e) conductivity measurements of pristine NDI-G, NDI-EtHx and PCBM self-doped in air on ITO substrates

To enhance the conductivity of NDI derivatives, N-DMBI was used as an n-type molecular dopant. N-DMBI has been extensively for its ability to catalyse the reduction of organic compounds ¹³ and facilitate hydrogen and/or electron transfer reactions by generating radical species. ^{14,15} The HOMO of N-DMBI is located at -4.67 eV, which is deeper than LUMO of PCBM, NDI-G and NDI-EtHx. Consequently, a direct electron transfer between N-DMBI and NDI derivatives is not possible due to energy level misalignment. Furthermore, C-H bond dissociation at room temperature is energetically unfavourable due to high enthalpy change. Hence, either photo ¹⁶ or thermal activation ^{16,17} is necessary a hydrogen atom transfer or hydride transfer, ¹⁸ forming an N-DMBI radical with a SOMO at -2.36 eV, ¹³ which enables electron transfer and facilitates the doping process, as shown in Figure 5.1d.

To verify the NDI radical anion formation during the doping process, we conducted EPR and UV-Vis absorption measurements on NDI-G and NDI-EtHx doped with 10 mol% and 30 mol% N-DMBI, respectively. Upon addition of N-DMBI, EPR shows a strong paramagnetic signal with a g value of 2.004, accompanied by hyperfine splitting features in the case of NDI-EtHx. These features were less distinct in the NDI-G moiety, due to its larger molecular structure, which slows molecular tumbling and obscures the hyperfine details. The ESR signal further confirms the formation of an NDI radical anion, whereas the pristine NDI-G and NDI-EtHx samples exhibited no appreciable radical signal in Figure 5.2a and 5.2b. Additional evidence of radical formation was obtained from solid-state UV-Vis absorption spectrum (Figure 5.2c), along with DFT-simulated spectra (Figure 5.2d), revealed a new reduction peak at 450 nm to 475 nm, ¹⁹ This feature further supports the formation of the NDI radical anion.

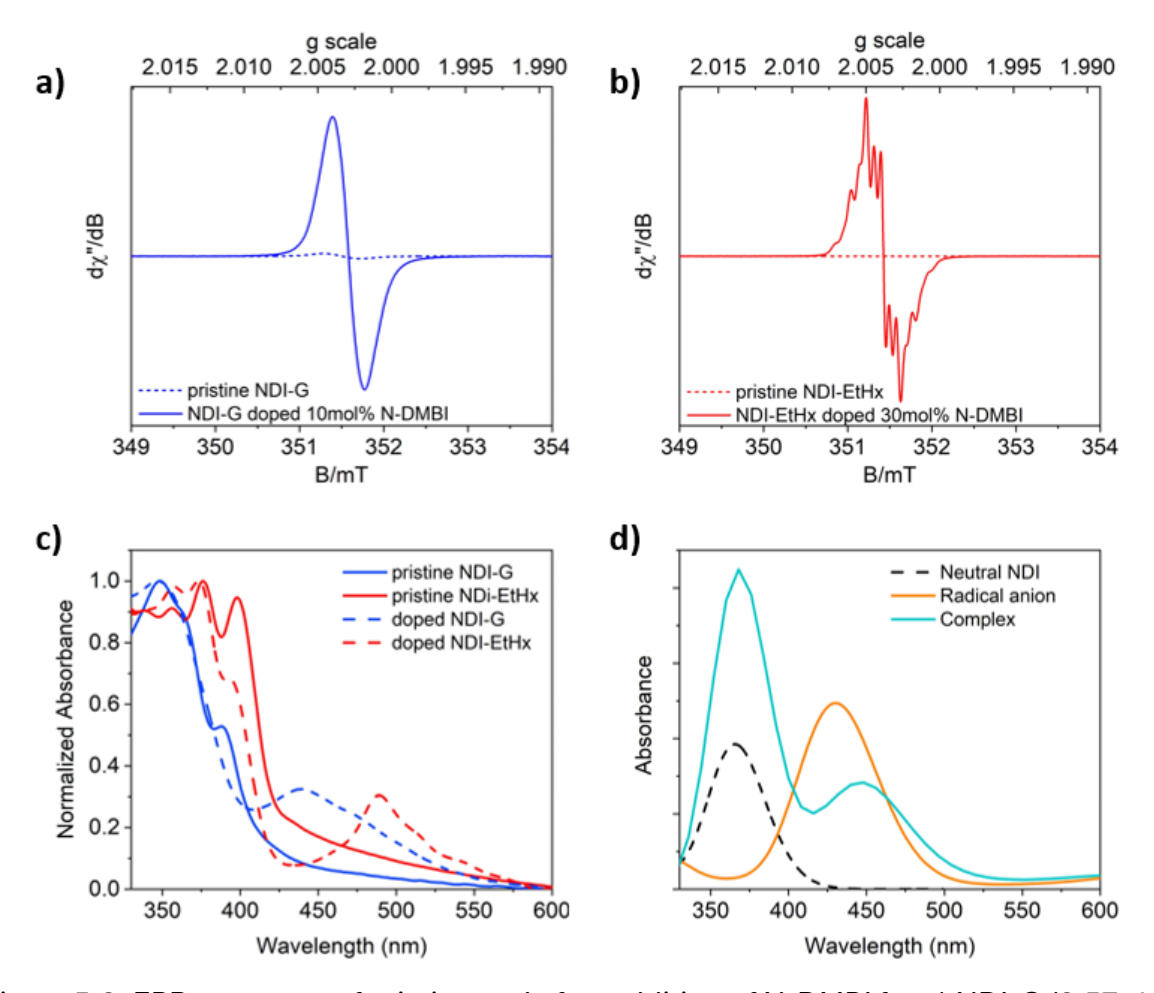


Figure 5.2. EPR spectrum of pristine and after addition of N-DMBI for a) NDI-G (3.57x10⁻² M) and b) NDI-EtHx (4.08x10⁻² M) in chlorobenzene; c) UV-vis absorption spectra of pristine and after addition of N-DMBI for both NDI derivatives (1 x 10⁻⁵ M); d) simulated UV-vis spectra of neutral methyl-NDI, [methyl-NDI/ N-DMBI]• complex and [methyl-NDI]• radical anion

The doping process in molecular electron transporters is generally described as a two-step mechanism. The first step involves the ionization of the additive, where a charge is transferred to the host materials, forming charge-transfer complexes (CTCs). In the second step, these CTCs dissociate, generating free charge carriers by transferring an electron to a nearby neutral host.²⁰ However, this second step is not straightforward in organic semiconductor due to the strong Coulombic biding energy between the host material and the additive.²⁰ To investigate this challenge, we performed DFT calculations simulating the interaction between N-DMBI and methyl-NDI. The resulting electrostatic potential (ESPs) maps and spin density distributions revealed that the negative charge

(red colour) localised predominantly on the more electronegative oxygen and nitrogen atoms of the NDI units (Figure 5.3a), while the unpaired electron is highly delocalised across the NDI unit (Figure 5.3b). These findings suggest that efficient electron transfer occurs between N-DMBI and NDI.

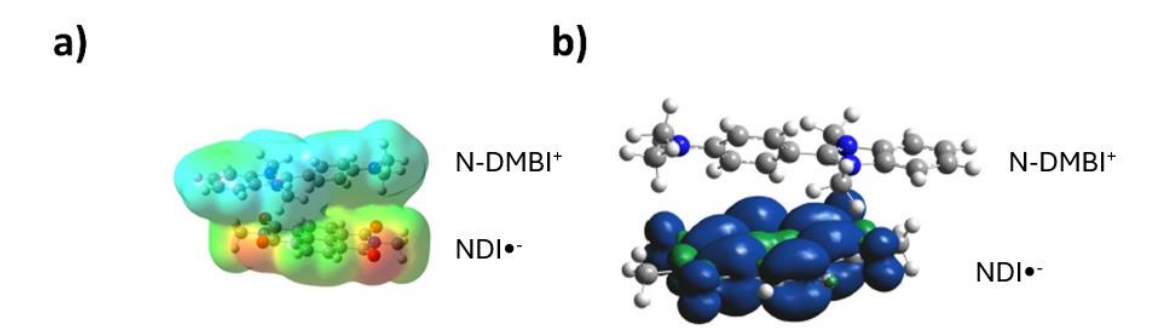


Figure 5.3. a) Electrostatic potentials (ESPs) and b) spin density maps of [methyl-NDI/N-DMBI]• complex, showing the negative

The binding energies of the [methyl-NDI/N-DMBI] complex and pi-pi dimer of methyl-NDI are 56.3 kcal/mol (2.44 eV) and 0.4 kcal/mol (0.02 eV), respectively. The significant difference highlights the much stronger binding force of the complex compared to most organic materials, which typically exhibit binding energies around 0.5 eV.²¹ The stability of the [methyl-NDI/N-DMBI]• CTC complex and its high Columbic binding energy suggest that dissociation into free charge carriers is unlikely under normal conditions. Given the one-electron transfer and strong binding energy, we define it as an integer CTC. To further investigate this behaviour, we used DFT modelling to calculate the energy level of N-DMBI radical, the [methyl-NDI/N-DMBI] complex and neutral methyl-NDI. The SOMO of the N-DMBI radical was found to be -2.51 eV, consistent with previous reported values.¹³ The LUMO level of methyl-NDI, calculated at 3.56 eV, lies deeper than the SOMO of [methyl-NDI/N-DMBI] at -3.47 eV. This energy alignment indicates the possibility of electron transfer from complex to neutral methyl-NDI in Figure 5.4. Further DFT calculations confirmed this trend for both pristine NDI derivatives and their complexes in Figure 5.5: [NDI-G/N-DMBI] vs NDI-G (-3.56 eV & -3.63 eV) and [NDI-EtHx/N-DMBI] • vs NDI-EtHx (-3.48 eV & -3.52 eV).

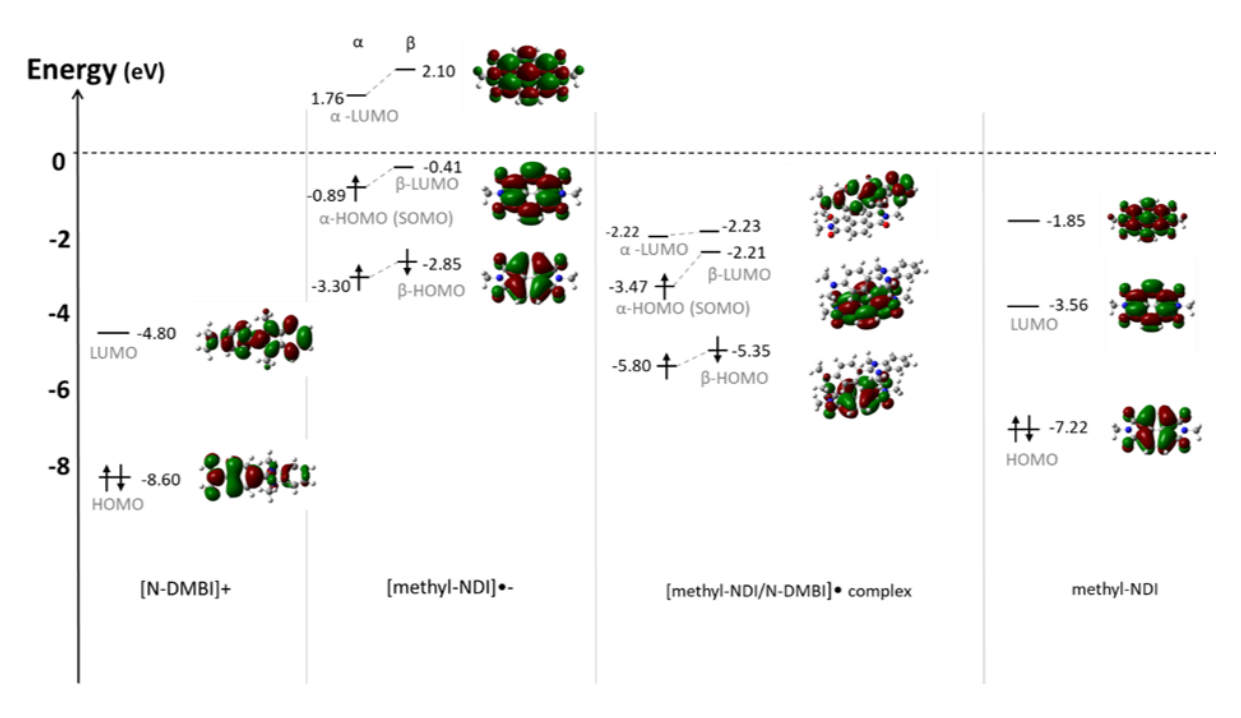


Figure 5.4. DFT predicted HOMO/LUMO maps and energies of methyl-NDI and [methyl-NDI/N-DMBI]•

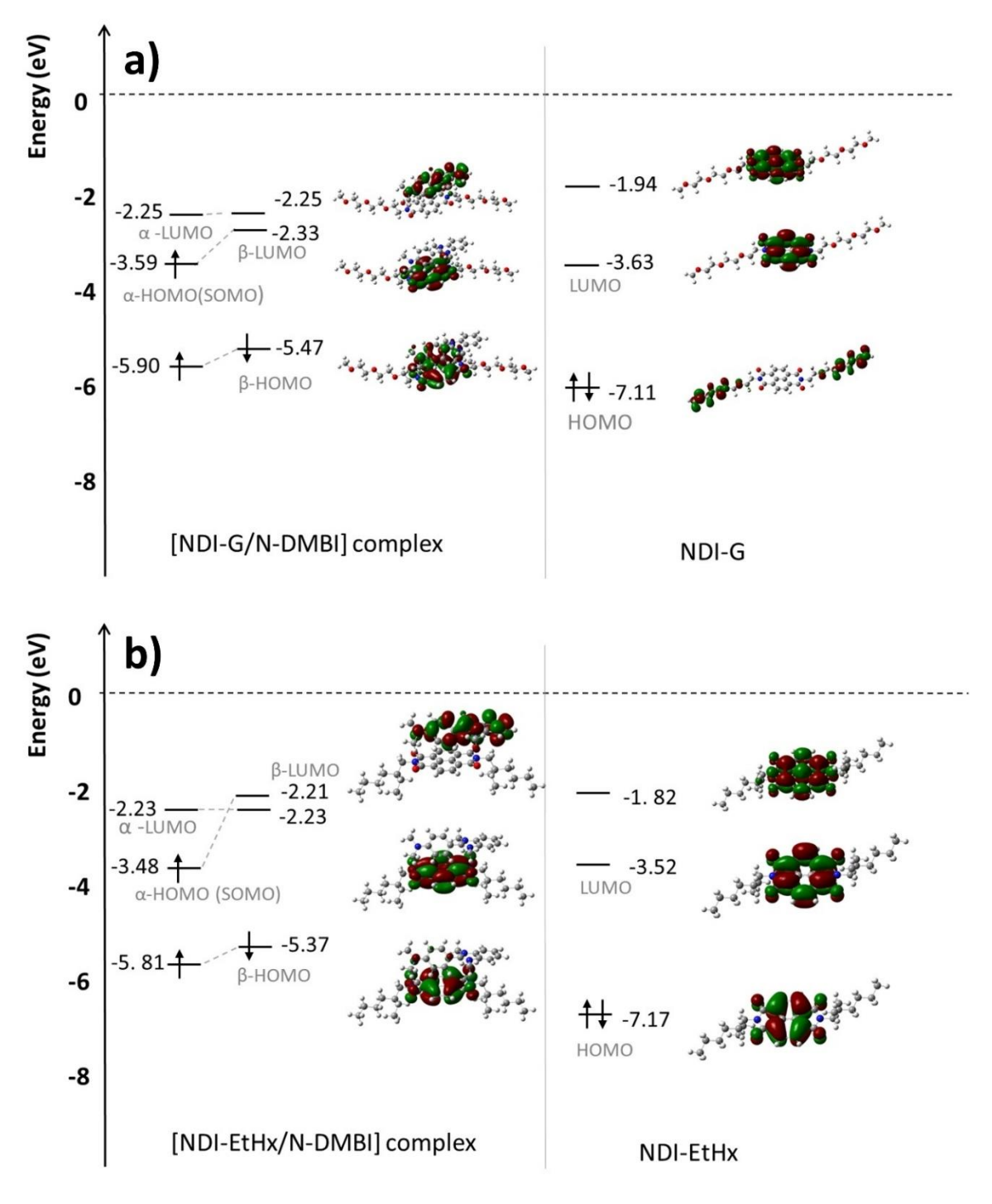


Figure 5.5. a) DFT predicted HOMO/LUMO maps and energies of NDI-G and [NDI-G/N-DMBI]• and NDI-EtHx and [NDI-EtHx/N-DMBI]•

Based on these observations, we propose a doping mechanism involving several key steps:

1. Hydride Transfer / Hydrogen Atom Transfer from N-DMBI:

N-DMBI-H + NDI
$$\rightarrow$$
 N-DMBI $^+$ + NDI/H $^-$
N-DMBI-H + NDI \rightarrow N-DMBI ullet + NDI/H ullet

2. Formation of NDI Anion Radical:

N-DMBI
$$^+$$
 + NDI/H $^-$ + NDI \rightarrow N-DMBI $^+$ + NDI $^-$ + NDI/H $^-$
N-DMBI $^+$ + NDI/H $^-$ + NDI \rightarrow N-DMBI $^+$ + NDI $^-$ + NDI/H $^-$

3. Complex Formation of [N-DMBI⁺+/NDI•⁻]:

$$N-DMBI^+ + NDI^{\bullet^-} + NDI/H^{\bullet} \rightarrow [N-DMBI^+ + /NDI^{\bullet^-}] + NDI + 1/2H_2$$

4. Electron Hopping Process:

$$[N-DMBI^++/NDI^-] + NDI \rightarrow N-DMBI^+ + NDI + NDI^- \rightarrow NDI + [N-DMBI^++/NDI^-]$$

This mechanism highlights the role N-DMBI in facilitating the formation of the NDI anion radical through hydride transfer and/or hydrogen atom transfer. However, determining the dominant pathway in this doping process is challenging, as both reactions occur spontaneously. Regardless of the initial species formed, evidence from UV-vis spectroscopy and EPR confirms the eventual formation of anion radical states in both NDI-G and NDI-EtHx. Additionally, the NDI anion radical forms a stable CTC with the N-DMBI cation, driven by strong binding energy and hydrogen gas generation. Importantly, the energy alignment between the complex and neural NDI allows efficient electron hopping process, promoting enhanced conductivity *via* charge transfer across the NDI matrix.

However, the mere formation of radicals and integer CTCs does not guarantee successful doping. Prior studies on two BF derivatives with glycol and alkyl side chains demonstrated in Chapter 4 that, although integer CTCs formed during n-type doping, electron transfer was inhibited due to unfavourable energy alignment between the integer CTC and the pristine species.²⁴ It shows that energetic alignment is a key factor in determining the effectiveness of charge-transfer, and ultimately the success of doping n-type molecular semiconductors.

To confirm the success of the doping reaction, we performed a series of solid-state UV-vis absorption (Figure 5.6) and conductivity measurements (Figure 5.8, Table 5.1 and 5.2) on NDI-G and NDI-EtHx, analysing how dopant concentration and reaction time influenced the doping process. The UV-vis absorption spectra in Figure 5.6a and 5.6b reveal differences in the reaction kinetics between the two NDI derivatives upon the addition of 50 mol% N-DMBI. A new reduction peak in 450 - 475 nm range signifies the radical anion formation during the doping process. 19 NDI-G exhibited significantly faster reaction kinetics than NDI-EtHx. For NDI-G, a distinct absorption peak appeared within 2 hours, while NDI-EtHx required approximately 24 hours to show a similar absorption band. This difference in kinetics is likely due to the polar glycol side chain in NDI-G, which enhances the overall polarity of the molecule, leading to improved miscibility within the host/dopant blend.8 This enhanced compatibility between NDI-G and N-DMBI molecules contributed to a more effective doping process compared to NDI-EtHx.8,25-27 These findings are consistent with previous reports indicating that an increase in reduction peak intensity in UV-vis absorption spectra correlates with the progression of the doping reaction time.^{28,29}

Interestingly, the intensity of the UV-vis absorption spectrum of NDI-G began to decline after reaching its peak at 2 hours, indicating a lack of stability of the NDI radical anion. This decrease in intensity likely stems from the highly reactive nature of organic radicals, which tend to degrade under ambient condition.³⁰ In contrast, NDI-EtHx displayed a steady increase in radical formation over time without a subsequent decline in intensity. However, prolonged doping (24 hour) was not entirely beneficial. A blue shift in the absorption slope of NDI-G and NDI-EtHx, associated with changes in the material's bandgap, suggests the possibility of secondary reactions occurring with NDI molecule. Additionally, after 24 hours of doping, the absorption peak of NDI-G around 750 nm became broadened, further indicating structural or electronic alterations. Additional absorption measurements (Figure 5.7) further support this observation, showing a reduction in the NDI derivative's radical peak upon exposure to air, confirming its instability.

We further explored the effect of increasing N-DMBI concentrations between 0 mol%

to 50 mol% at 2 hours (NDI-G) and 16 hours (NDI-EtHx), on the doping efficiency of NDI-G and NDI-EtHx. The radical anion absorption peaks for both derivatives began to appear at 20 mol% of N-DMBI doping for NDI-G and NDI-EtHx. As the dopant concentration increased, the equilibrium position shifted towards the product side, consistent with Le Châtelier's principle: higher reactant concentrations increase the frequency of effective collisions between the NDI and N-DMBI, thereby accelerating the forward reaction and promoting greater radical anion formation. This indicated a more pronounced doping reaction at higher dopant concentrations up to 50 mol%.

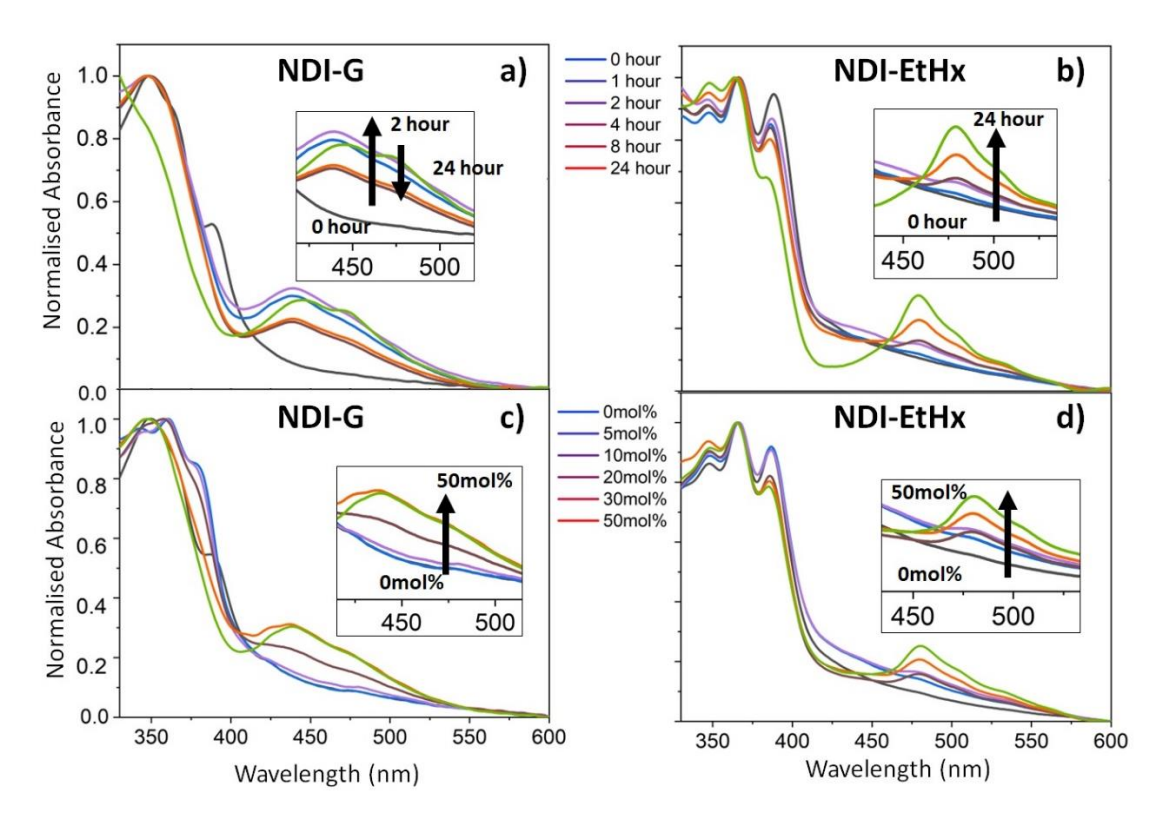


Figure 5.6. UV-vis absorption spectra of a) NDI-G and b) NDI-EtHx in film on glass substrates in the presence of 50 mol% of N-DMBI with reaction times between 0 to 24 hours; c) NDI-G and d) NDI-EtHx in film on glass substrates in the presence of 0 mol% to 50 mol% of N-DMBI at 2 hours (NDI-G) and 16 hours (NDI-EtHx)

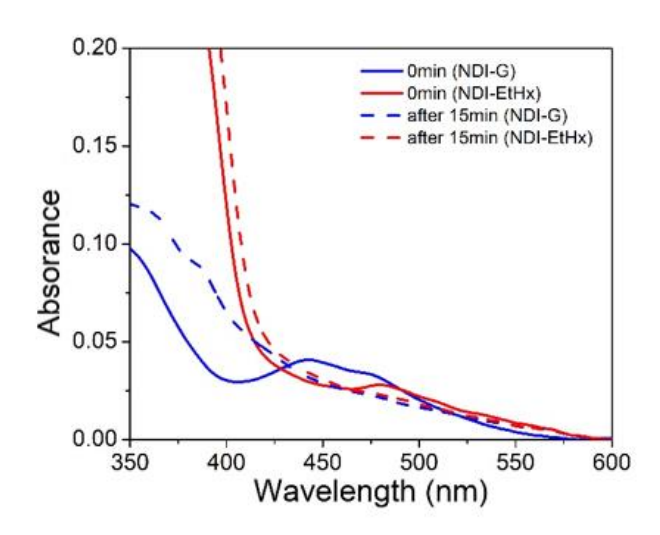


Figure 5.7. UV-vis absorption spectra of NDI-G and NDI-EtHx films on glass substrates, each containing 50 mol% of N-DMBI. Solid lines represent data at 0 min, while dashed lines show spectra after 15 min of air exposure (The variations in absorption intensity spectra are mainly attributed to differences in film thickness, which arise from the spin-coating process. NDI molecules dissolve in chlorobenzene, and NDI-EtHx is more effectively solvated in nonpolar chlorobenzene, resulting in stronger intrinsic absorption. In contrast, NDI-G exhibits lower solubility than NDI-EtHx, leading to reduced absorbance. Film thickness can vary between the two materials, as the thicker or denser NDI-EtHx films further contribute to the higher absorption intensity)

Conductivity measurements of NDI derivatives after the addition of 50 mol% N-DMBI added were conducted to evaluate the doping efficiency of the materials bearing different side-chains, as shown in Figure 5.8a. Initially, NDI-G exhibited a low conductivity of 2.52x10⁻⁷ S/cm, which dramatically increased to 4.89x10⁻⁴ S/cm after 1 hour of doping. This enhancement reached its peak at 1.09x10⁻³ S/cm after 2 hours, indicating rapid doping kinetics. However, after reaching this maximum, the conductivity declined to 5.8x10⁻⁵ S/cm after 24 hours, likely due to the instability of the NDI radical anion. In comparison, for NDI-EtHx, a 1 hour reaction with N-DMBI led to an improvement in conductivity from an initial value of 2.35x10⁻⁷ S/cm to 3.25x10⁻⁶ S/cm. This value continued to rise steadily, reaching approximately 10⁻⁵ S/cm, where it stabilised and remained constant up to 24 hours. This behaviour is consistent with the UV-vis absorption results, indicating that the glycol side-chain provides a better environment for the n-type doping, allowing NDI-G to achieve maximum conductivity more quickly than

NDI-EtHx. However, it is noteworthy that the conductivity in NDI-G dropped if the reaction was allowed to proceed for longer times, presumably due to instability of the radical anion.

Figure 5.8b shows the conductivity for NDI-G and NDI-EtHx with varying mole percentages of N-DMBI, ranging from 0 mol% to 50 mol%, with reaction times determined from the maxima in Figure 5.6a and 5.6b (NDI-G for 2 hours and NDI-EtHx for 16 hours). The initial conductivity of pristine NDI-G and NDI-EtHx ranged from 2 to 3x10⁻⁷ S/cm. In the case of NDI-EtHx, the conductivity increased to 6.21x10⁻⁶ S/cm with 5 mol% N-DMBI and reached the maximum to 2.38x10⁻⁵ S/cm at 30 mol%. However, the conductivity started to decline beyond this optimal additive concentration level, from 1.82x10⁻⁵ S/cm at 40 mol% and further decreasing to 1.40x10⁻⁵ S/cm at 50 mol%. In the case of NDI-G, the conductivity dramatically increased to 1.84x10⁻³ S/cm with 2 mol% N-DMBI and peaked at 1.00x10⁻² S/cm with 10 mol% N-DMBI doping. However, further increase in additive concentration led to a decline in conductivity, which dropped to 4.50x10⁻⁴ S/cm at 50 mol%.

These results indicate the successful electron transfer from the complex to the neutral NDI, demonstrating effective doping, with optimal conditions for NDI-G yielding conductivity values up to 10⁻² S/cm. However, excessive additive concentration had a detrimental effect. At high additive levels, trap states likely form within the material, ^{31,32} capturing electrons and leading to reduced electron conductivity ^{33,34} and mobility ^{31,33}, as well as increased recombination. ³⁵ Consequently, this behaviour reduces the number of free charges within the material. Based on our results, the optimised doping conditions for these materials are: 10 mol% N-DMBI for a 2 hour reaction for NDI-G, and 30 mol% N-DMBI for a 16 hour reaction for NDI-EtHx. Notably, the doping kinetics of NDI-G are competitive with other reports, achieving peak conductivity within 3 hours. ^{29,36}

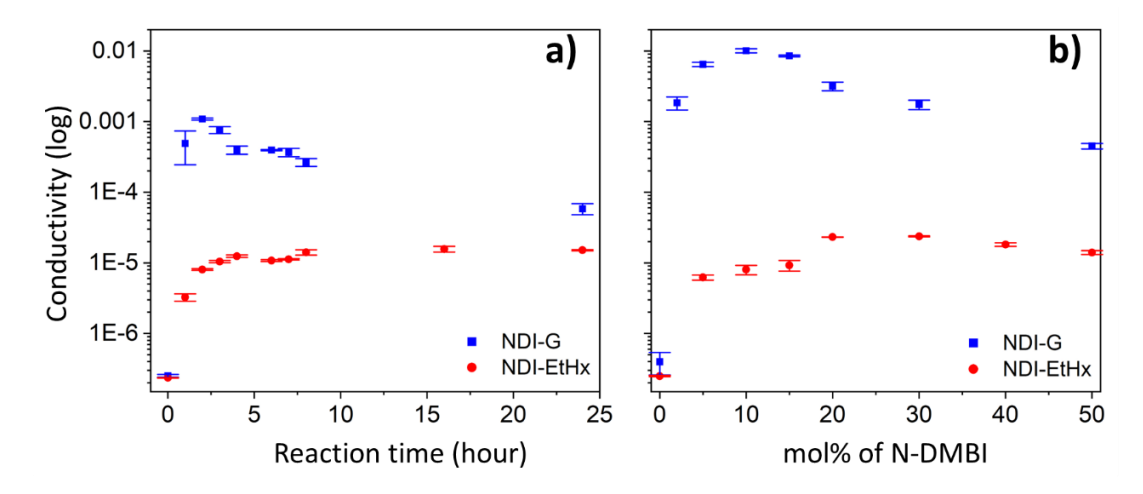


Figure 5.8. Logarithmic plot of conductivity measurements for N-DMBI doped in NDI-G and NDI-EtHx at a) reaction time ranging from 0 to 24 hours (50 mol% N-DMBI doping) and b) ranging from 0 mol% to 50 mol% (reaction time: 2 hours for NDI-G and 16 hours for NDI-EtHx). (Average of three samples with error bars for each data set) (The variation in conductivity for pristine NDI-G in Figure 5.8b is attributed to the variation for ITO substrates)

Table 5.1. Conductivity measurements for N-DMBI doped in NDI-G and NDI-EtHx at different mol% (Average of three samples with error for each data)

	NDI-G		NDI-EtHx		
mol%	average (S/cm)	error	average (S/cm)	error	
0	3.98E-07	1.39E-07	2.49E-07	4.51E-09	
2	1.84E-03	3.89E-04	/	/	
5	6.45E-03	4.63E-04	6.21E-06	5.06E-07	
10	1.01E-02	6.89E-04	8.01E-06	1.22E-06	
15	8.50E-03	2.44E-04	9.22E-06	1.58E-06	
20	3.17E-03	4.52E-04	2.32E-05	1.53E-07	
30	1.74E-03	2.61E-04	2.38E-05	3.92E-07	
40	/	/	1.82E-05	1.00E-06	
50	4.50E-04	3.93E-05	1.40E-05	8.68E-07	

Table 5.2. Conductivity measurements for N-DMBI doped in NDI-G and NDI-EtHx at different reaction time (Average of three samples with error for each data)

	NDI-G		NDI-EtHx		
Time (hr)	average (S/cm)	error	average (S/cm)	error	
0	2.52E-07	1.13E-08	2.35E-07	1.88E-09	
1	4.89E-04	2.45E-04	3.25E-06	3.85E-07	
2	1.09E-03	3.72E-05	8.04E-06	2.21E-07	
3	7.60E-04	8.63E-05	1.04E-05	3.75E-07	
4	3.96E-04	5.21E-05	1.24E-05	4.98E-07	
6	3.94E-04	8.53E-06	1.08E-05	3.44E-07	
7	3.67E-04	5.06E-05	1.12E-05	2.40E-07	
8	2.66E-04	3.33E-05	1.41E-05	1.22E-06	
16	/	/	1.57E-05	1.44E-06	
24	5.83E-05	1.05E-05	1.51E-05	3.35E-07	

To evaluate the effectiveness of n-doping of NDI derivatives and their potential for hybrid optoelectronic devices, inverted PSCs were fabricated using glass/ITO/MeO-2PACz/Al₂O₃ NPs/perovskite/ETL/BCP/Ag. The photovoltaic performance of the pristine and doped NDI derivative PSCs was compared to PCBM-based PSCs with J-V curves illustrated in Figure 5.9a and summarised in Table 5.3. Doping NDI-G with N-DMBI significantly improved both conductivity and device performance, with PCE increasing from 10.44 % to 14.12 %. The Jsc of NDI-G PSCs rose from 21.25 mA/cm² to 22.15 mA/cm² after doping, approaching the performance of PCBM-based PSCs. This increase suggests that enhanced conductivity in doped NDI-G is beneficial for charge extraction to the electrode, leading to higher Jsc. Additionally, the FF of doped NDI-G PSCs increased from 0.53 to 0.68 compared to undoped NDI-G PSCs. This enhancement is associated a reduction of the series resistance, as evidenced by the slopes of the JV curves, see Figure 5.9a. The extracted Rs values for doped NDI-G PSCs were comparable to those of PCBMbased PSCs, indicating the success of the doping strategy. In contrast, doped NDI-EtHx did not lead to performance improvements. This lack of improvement is likely a result of the less effective doping process which does not yield a high enough conductivity value to overcome the detrimental effects of the addition of the dopant molecules.

Despite the higher conductivity in doped NDI-G compared to PBCM, its overall performance is still lower than this reference system, suggesting additional interfacial effects beyond simple energy-level considerations. In particular, there is a growing body of knowledge highlighting that fullerene derivatives play additional roles to facilitate charge extraction, for instance in the form of surface passivation.³⁷ This effect attributed to the interaction at perovskite/PCBM interface, which reduces interfacial recombination and lowers the interfacial energy barrier.³⁸ Similar benefits have been observed in regular PSCs where C60 self-assembled monolayers (SAMs) were used to passivate SnO₂, reducing interfacial defects.³⁹ This defect mitigation is further supported by minimised hysteresis in PCBM-based devices compared to NDI-based devices, as shown in Figure 5.9b.

To better understand the performance discrepancies, we examined film morphology using scanning electron microscopy (SEM) (Figure 5.10). No significant morphological changes are observed between PCBM, pristine NDI-G, and NDI-EtHx. After doping, NDI-G maintained its morphology, indicating that improved PSC performance resulted from enhanced charge transport. In contrast, doped NDI-EtHx exhibited the formation of needle-shaped features, suggesting dopant-induced molecular packing disruptions or aggregation. The polarity difference between NDI-EtHx and N-DMBI leads to dopant residue aligning with the alkyl side-chain in crystalline regions, disrupting π - π stacking of NDI molecules or dopant self-aggregation, as observed in SEM images. This behaviour is similar to that observed in reported PCBM systems, 40,41 where large aggregate formation negatively impacts photovoltaic performance. It is possible that the steric hindrance of the alkyl side-chains in NDI-EtHx leads to the aggregation. This explains why the Voc of doped NDI-EtHx decreased from 1.00 V to 0.95 V, likely due to surface recombination caused by the needle-shaped features, whereas NDI-G maintained a consistent Voc value.

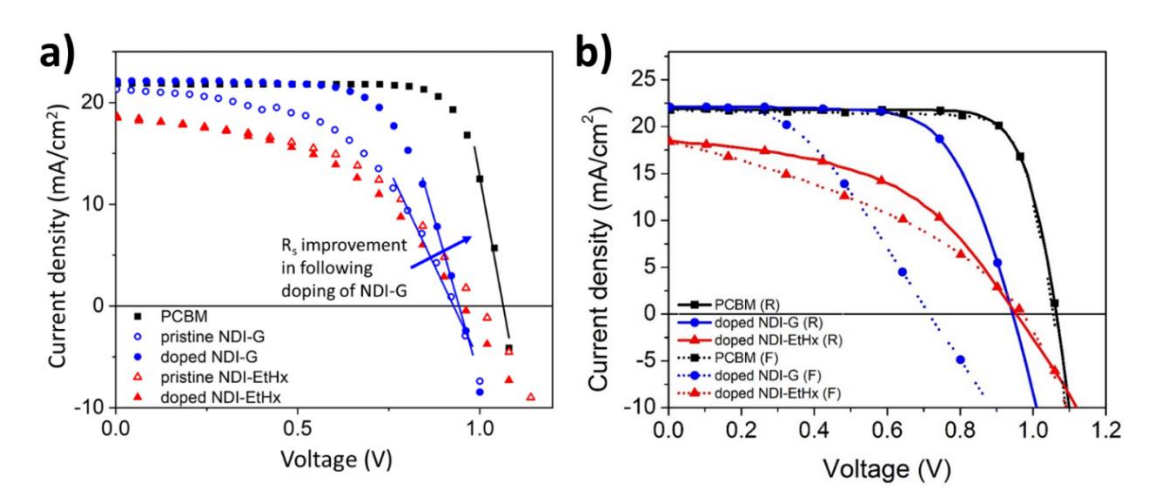


Figure 5.9. a) J–V characteristic curves of champion devices based on PCBM, pristine, and doped NDI-G and NDI-EtHx PSCs (Lines represent to fitting curves of each J-V curves) and b) JV curves showing forward (dashed line) and reverse (solid line) curves for devices incorporating PCBM, pristine and doped of NDI-G and NDI-EtHx.

Table 5.3. Photovoltaic performance of reference PCBM-based, pristine and doped NDI-G-based and NDI-EtHx-based PSCs (10 devices for each condition)

ETL	N-DMBI (mol%)	Jsc (mA/cm²)	Voc (V)	FF	PCE (%)
PCBM	/	21.86 ± 0.38	1.07 ± 0.01	0.78 ± 0.02	18.26 ± 0.69
NDI-G	0	21.25 ± 0.58	0.93 ± 0.06	0.53 ± 0.02	10.44 ± 0.80
	10	22.15 ± 1.14	0.94 ± 0.04	0.68 ±0.07	14.12 ± 1.05
NDI-EtHx	0	18.56 ± 0.63	1.00 ± 0.07	0.50 ± 0.02	9.18 ± 0.83
	30	18.47 ± 1.43	0.95 ± 0.04	0.48 ± 0.02	8.45 ± 0.77

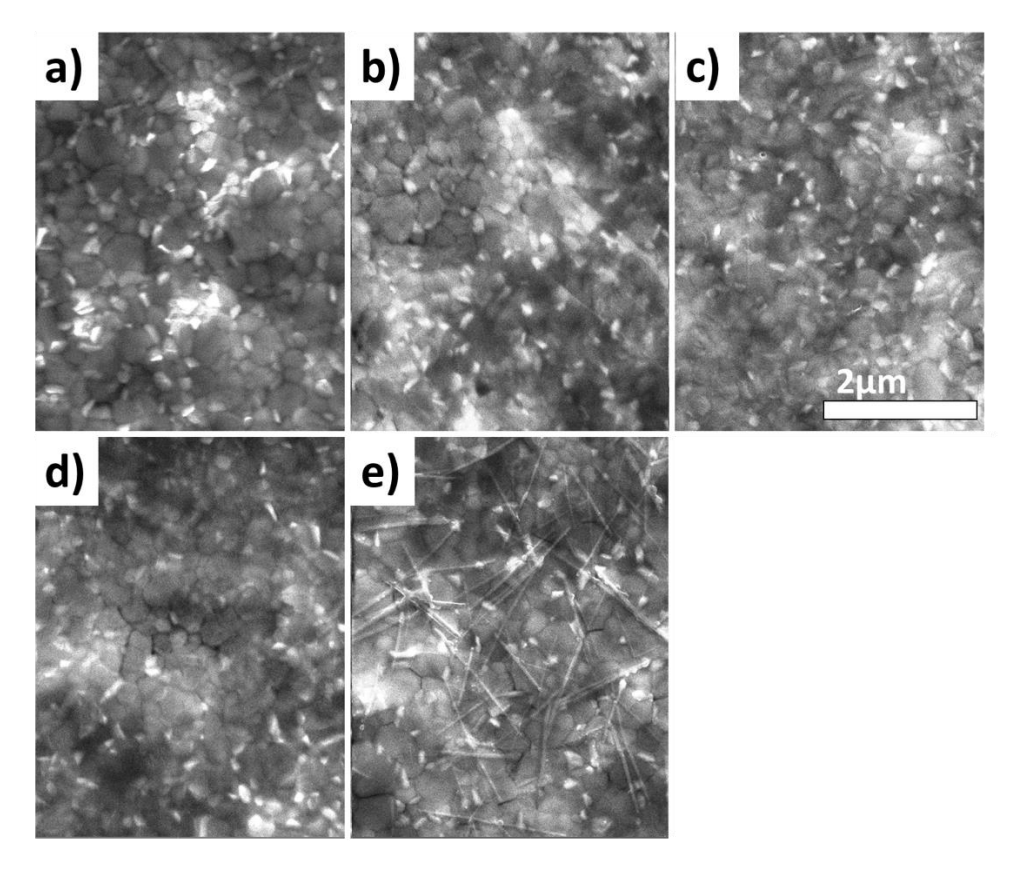


Figure 5.10. SEM images of a) PCBM; b) pristine NDI-G; c) pristine NDI-EtHx, d) doped NDI-G and e) doped NDI-EtHx

5.3. Conclusions

In this study, we investigated two non-fullerene ETMs based on NDI analogues with solubility-enhancing side-chains: glycol (NDI-G) and alkyl (NDI-EtHx). Despite exhibiting similar optical and electrochemical properties, both derivatives initially demonstrated limited conductivity. To improve their performance, we employed n-type doping using N-DMBI as the dopant. Given that the HOMO of N-DMBI is deeper than the LUMO of the NDI derivatives, direct electron transfer is energetically unfavourable. Consequently, we proposed the following doping mechanism: the formation of N-DMBI radical with a SOMO enables electron transfer to the NDI derivatives, resulting in the formation of NDI radicals, as confirmed by ESR. The electron from NDI radical then transfers to the NDI derivatives and forms NDI radicals. DFT calculations support the initial formation of an integer CTC between N-DMBI cation and NDI anion radical, stabilised by strong binding energies. The energy alignment between the integer CTC and neural NDI molecules enables effective electron transfer, ultimately generating free charges. UV-vis absorption and conductivity

measurements revealed that the polar glycol side chains in NDI-G accelerate the doping process compared to the non-polar alkyl side chains in NDI-EtHx. This enhancement is attributed to the improved polarity compatibility between the glycol side-chains and the dopant, which promotes molecular interactions and enhances doping efficiency. However, the resulting NDI radicals were found to be unstable in solution, degrading after several hours. The optimized NDI-G doped material exhibited a conductivity exceeding $10^{-2}\,\text{S/cm}$. When integrated into PSCs, NDI-G increased the PCE from 10.44% to 14.12% after N-DMBI doping, primarily by reducing the series resistance. Despite the higher conductivity of doped NDI-G compared to PCBM, the overall device performance remained lower due to greater interfacial recombination and increased hysteresis. This observation suggests that effective interface passivation plays a more critical role in device efficiency than simply reducing series resistance in the charge extraction layer. Thus, selection of non-fullerene ETMs requires a balanced approach, not only lowering series resistance through high conductivity but also focusing on interfacial engineering, such as defect-free interfaces, to suppress recombination losses. A combined strategy of moderate doping and effective passivation is required to unlock the full potential of non-fullerene ETMs.

5.4. References

- 1 T. H. Kim, J. H. Kim and K. Kang, *Jpn J Appl Phys*, 2023, **62**, SE0803.
- J. Liu, B. van der Zee, R. Alessandri, S. Sami, J. Dong, M. I. Nugraha, A. J. Barker, S. Rousseva, L. Qiu, X. Qiu, N. Klasen, R. C. Chiechi, D. Baran, M. Caironi, T. D. Anthopoulos, G. Portale, R. W. A. Havenith, S. J. Marrink, J. C. Hummelen and L. J. A. Koster, *Nat Commun*, 2020, 11, 5694.
- 3 S. K. Jung, J. H. Heo, D. W. Lee, S. C. Lee, S. H. Lee, W. Yoon, H. Yun, S. H. Im, J. H. Kim and O. P. Kwon, *Adv Funct Mater*, 2018, **28**, 1800346.
- 4 M. Korzec, S. Kotowicz, K. Łaba, M. Łapkowski, J. G. Małecki, K. Smolarek, S. Maćkowski and E. Schab-Balcerzak, *European J Org Chem*, 2018, **2018**, 1756–1760.
- D. Zhao, Q. Jiang, Y. Jia, J. Zhou, N. Zheng, D. Hu and Y. Ma, *Mater Today Energy*, 2021, **21**, 100710.
- D. Kiefer, A. Giovannitti, H. Sun, T. Biskup, A. Hofmann, M. Koopmans, C. Cendra, S. Weber, L. J. Anton Koster, E. Olsson, J. Rivnay, S. Fabiano, I. McCulloch and C. Müller, ACS Energy Lett, 2018, 3, 278–285.
- 7 D. Wang, T. Ye and Y. Zhang, *J Mater Chem A Mater*, 2020, **8**, 20819–20848.
- J. Liu, L. Qiu, G. Portale, S. Torabi, M. C. A. Stuart, X. Qiu, M. Koopmans, R. C. Chiechi, J. C. Hummelen, L. Jan and A. Koster, *Nano Energy*, 2018, **52**, 183–191.
- 9 M. Comin, V. Lemaur, A. Giunchi, D. Beljonne, X. Blase and G. D'Avino, *J Mater Chem C*, 2022, **10**, 13815–13825.
- V. Vijayakumar, E. Zaborova, L. Biniek, H. Zeng, L. Herrmann, A. Carvalho, O. Boyron,
 N. Leclerc and M. Brinkmann, ACS Appl Mater Interfaces, 2019, 11, 4942–4953.
- 11 P. Reiser, F. S. Benneckendorf, M. M. Barf, L. Müller, R. Bäuerle, S. Hillebrandt, S. Beck, R. Lovrincic, E. Mankel, J. Freudenberg, D. Jänsch, W. Kowalsky, A. Pucci, W. Jaegermann, U. H. F. Bunz and K. Müllen, *Chemistry of Materials*, 2019, **31**, 4213–4221.
- 12 M. Khalid, M. Khan, K. Mahmood, M. Arshad, M. Imran, A. A. C. Braga and R. Hussain, *Sci Rep*, 2022, **12**, 20220.
- 13 P. Wei, J. H. Oh, G. Dong and Z. Bao, *J Am Chem Soc*, 2010, **132**, 8852–8853.
- 14 D. D. Tanner and J. J. Chen, *J. Org. Chem*, 1989, **54**, 3842–3846.
- 15 D. D. Tanner, J. J. Chen, L. Chen and C. Luelo, *JAm Chem Soc*, 1991, **113**, 8074–8081.
- 16 O. Bardagot, C. Aumaître, A. Monmagnon, J. Pécaut, P.-A. Bayle and R. Demadrille,

- Appl. Phys. Lett, 2021, 118, 203904.
- S. Riera-Galindo, A. Orbelli Biroli, A. Forni, Y. Puttisong, F. Tessore, M. Pizzotti, E. Pavlopoulou, E. Solano, S. Wang, G. Wang, T. P. Ruoko, W. M. Chen, M. Kemerink, M. Berggren, G. Di Carlo and S. Fabiano, ACS Appl Mater Interfaces, 2019, 11, 37981–37990.
- 18 S. Jhulki, H. I. Un, Y. F. Ding, C. Risko, S. K. Mohapatra, J. Pei, S. Barlow and S. R. Marder, *Chem*, 2021, **7**, 1050–1065.
- 19 P. Lasitha, Photochemical & Photobiological Sciences, 2020, 19, 1603–1612.
- 20 A. Mityashin, Y. Olivier, T. Van Regemorter, C. Rolin, S. Verlaak, N. G. Martinelli, D. Beljonne, J. Cornil, J. Genoe and P. Heremans, *Advanced Materials*, 2012, 24, 1535–1539.
- 21 M. L. Tietze, J. Benduhn, P. Pahner, B. Nell, M. Schwarze, H. Kleemann, M. Krammer, K. Zojer, K. Vandewal and K. Leo, *Nat Commun*, 2018, **9**, 1182.
- 22 F. Pallini, S. Mattiello, N. Manfredi, S. Mecca, A. Fedorov, M. Sassi, K. Al Kurdi, Y. F. Ding, C. K. Pan, J. Pei, S. Barlow, S. R. Marder, T. Q. Nguyen and L. Beverina, *J Mater Chem A*, 2023, **11**, 8192–8201.
- 23 Y. Zeng, W. Zheng, Y. Guo, G. Han and Y. Yi, *J Mater Chem A Mater*, 2020, **8**, 8323–8328.
- 24 W. K. Yiu, D. Wilkinson, M. Cariello, M. Giza, N. Pant, N. Mohammed, B. Vella, S. Sproules, G. Cooke and P. Docampo, *Energy Advances*, 2024, **3**, 2939–2946.
- 25 J. Liu, M. P. Garman, J. Dong, B. Van Der Zee, L. Qiu, G. Portale, J. C. Hummelen and L. J. A. Koster, ACS Appl Energy Mater, 2019, 2, 6664–6671.
- 26 J. Liu, S. Maity, N. Roosloot, X. Qiu, L. Qiu, R. C. Chiechi, J. C. Hummelen, E. von Hauff and L. J. A. Koster, *Adv Electron Mater*, 2019, **5**, 1800959.
- 27 J. Liu, L. Qiu, R. Alessandri, X. Qiu, G. Portale, J. Dong, W. Talsma, G. Ye, A. Akbar Sengrian, P. C. T Souza, M. Antonietta Loi, R. C. Chiechi, S. J. Marrink, J. C. Hummelen, L. Jan Anton Koster, J. Liu, L. Qiu, R. Alessandri, X. Qiu, G. Portale, J. Dong, W. Talsma, G. Ye, A. A. Sengrian, M. A. Loi, R. C. Chiechi, S. J. Marrink, J. C. Hummelen, L. J. A Koster and P. C. T Souza, *Advanced Materials*, 2018, 30, 1704630.
- 28 L. Hu, T. Liu, J. Duan, X. Ma, C. Ge, Y. Jiang, F. Qin, S. Xiong, F. Jiang, B. Hu, X. Gao, Y. Yi, Y. Zhou, L. Hu, T. F. Liu, J. S. Duan, Y. Y. Jiang, F. Qin, S. X. Xiong, F. Y. Jiang, B. Hu, Y. H. Zhou, X. Y. Ma, Y. P. Yi, C. W. Ge and X. K. Gao, *Adv Funct Mater*, 2017, 27, 1703254.
- 29 S. Wang, H. Sun, U. Ail, M. Vagin, P. O. Å. Persson, J. W. Andreasen, W. Thiel, M.

- Berggren, X. Crispin, D. Fazzi and S. Fabiano, *Advanced Materials*, 2016, **28**, 10764–10771.
- 30 Q. Song, F. Li, Z. Wang and X. Zhang, *Chem Sci*, 2015, **6**, 3342–3346.
- 31 G. Zuo, Z. Li, O. Andersson, H. Abdalla, E. Wang and M. Kemerink, *Journal of Physical Chemistry C*, 2017, **121**, 7767–7775.
- 32 H. F. Haneef, A. M. Zeidell and O. D. Jurchescu, *J Mater Chem C*, 2020, **8**, 759–787.
- 33 S. Olthof, S. Mehraeen, S. K. Mohapatra, S. Barlow, V. Coropceanu, J.-L. Brédas, S. R. Marder and A. Kahn, *Phys. Rev. Lett.*, 2012, **109**, 176601.
- 34 B. Lü, M. Riede and K. Leo, *Phys. Status Solidi A*, 2007, **210**, 9–43.
- 35 X. Ma, R. A. J. Janssen and G. H. Gelinck, *Adv. Mater. Technol.*, 2023, **8**, 2300234.
- 36 T. L. Dexter Tam, T. T. Lin, M. I. Omer, X. Wang and J. Xu, J Mater Chem A, 2020, 8, 18916–18924.
- 37 A. F. Akbulatov, O. A. Kraevaya, V. S. Bolshakova, L. A. Frolova and P. A. Troshin, *Synth Met*, 2023, **299**, 117468.
- 38 W. Zhang, Y.-C. Wang, X. Li, C. Song, L. Wan, K. Usman, J. Fang, W. Zhang, Y. Wang, X. Li, C. Song, L. Wan, K. Usman and J. Fang, *Advanced Science*, 2018, **5**, 1800159.
- 39 C. Wang, D. Zhao, C. R. Grice, W. Liao, Y. Yu, A. Cimaroli, N. Shrestha, P. J. Roland, J. Chen, Z. Yu, P. Liu, N. Cheng, R. J. Ellingson, X. Zhao and Y. Yan, *J Mater Chem A Mater*, 2016, **4**, 12080–12087.
- 40 S. Sung Kim, S. Bae and W. Ho Jo, Chem. Commun, 2015, **51**, 17413.
- 41 J. H. Bae, Y. J. Noh, M. Kang, D. Y. Kim, H. Bin Kim, S. H. Oh, J. M. Yun and S. I. Na, *RSC Adv*, 2016, **6**, 64962–64966.

Chapter 6. Understanding the Impact of SAM Fermi Levels on High Efficiency p-i-n Perovskite Solar Cells

This chapter has been adapted from *J. Phys. Chem. Lett.*, **2024**, 15, 10686-10695. Acknowledgements are extended to Mr. Fraser J. Angus (University of Glasgow) for SaP measurements, Dr. Muhammad Umair Ali (University of Hong Kong) for TRPL measurements, Mr. Jingbo Wang (University of Hong Kong) for NiOx nanoparticles synthesis and Mr. Tik Lun Leung (University of Sydney) for KPFM measurements.

6.1. Introduction

Interfacial engineering is typically employed in photovoltaics research to enhance device performance. Unlike traditional photovoltaic systems, perovskite solar cells (PSCs) introduce unique challenges and opportunities due to the ionic properties of their absorber layers. These ionic characteristics necessitate specialised approaches for interfacial optimisation. For example, strategies such as incorporating ionic compounds to form layered perovskites on top of the perovskite, or simple adsorption have shown significant potential in passivating surface defects, leading to marked improvements in device performance.

Recent advancements in PSC interfacial engineering have highlighted the effectiveness of self-assembled monolayers (SAMs) in enhancing charge extraction.^{4,5} When SAMs bind to indium tin oxide (ITO), they generate dipoles that modify the work function of the contacts and introduce interfacial band bending, improving charge collection efficiency.⁶ Despite their prominence as state-of-the-art HTMs, the relationship between a SAM's dipole, surface orientation, and its effect on interfacial energetics remains poorly understood. Furthermore, the performance of SAM-based PSCs is related to the choice of perovskite composition and device structure, necessitating extensive optimization through iterative experimentation.^{7,8} This complexity is exacerbated by the constraints of conventional energy level characterization techniques, such as X-ray photoelectron spectroscopy (XPS) and ultraviolet photoelectron spectroscopy (UPS),^{9,10} which primarily probe partial device stacks and are highly surface-sensitive.

In this work, we examine how the built-in potential created by HTL and ETL affects key performance parameters in high-efficiency, hysteresis-free PSCs. Due to various dipole strengths of SAMs, we systematically quantify the potential across the perovskite layer, obtaining values between 0.6 V and 1.0 V. Additionally, we incorporate complementary characterisation techniques, including TRPL and JV characteristic analysis, to distinguish between charge recombination, charge extraction, and interfacial potential barriers. Our results offer insights into device physics of inverted PSCs, enabling performance optimisation through tailored interfacial energetics.

6.2. Results and discussion

We utilised four commercially available SAMs including [2-(9H-carbazol9-yl)ethyl]phosphonic acid (2-PACz), [2-(3,6-dimethoxy9H-carbazol-9-yl)ethyl]phosphonic acid (MeO-2PACz), (4-(3,6-dimethyl-9H-carbazol-9-yl)butyl)phosphonic acid (Me-4PACz) and (2-(3,6-Dichloro-9H-carbazol-9-yl)ethyl)phosphonic acid (Cl-2PACz) to investigate how the Fermi level shift induced by the SAMs effects on PSCs. These SAMs have been widely studied in literature, serving as important reference materials and also achieved high PCEs. 11,12 Moreover, they exhibit varying dipole strength, following the order 2PACz > Me-4PACz > MeO-2PACz, 13,14 which leads to a significant Fermi level shift when attached to metal oxide surface, which has been verified by UPS and XPS analysis. 15 By utilising these well-characterized SAMs, this study aims to further explore interfacial energetics in PSCs.

To evaluate the photovoltaic performance of the SAM, we fabricated inverted PSCs using NiOx NPs as HTL, which improve the efficiency and wetting properties compared to bare ITO.¹⁶ Two different perovskite compositions were examined: the widely studied methylammonium lead iodide (MAPI) and an optimised double-cation formulation composed of formamidinium and caesium (FA_{0.9}Cs_{0.1}Pbl_{2.9}Br_{0.1}), referred to as "DC". The ETL and hole-blocking layer comprised PCBM and BCP, respectively, with Ag as the top electrode. Complete details on device fabrication and synthesis can be found in Chapter 3.

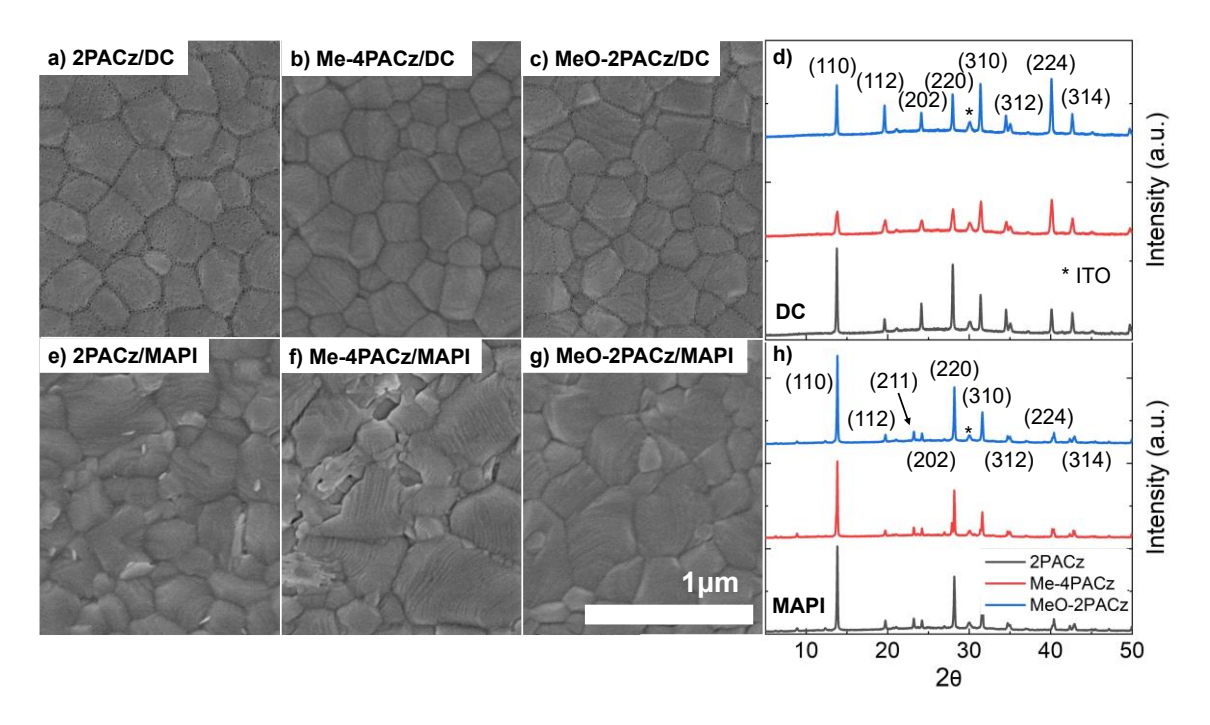


Figure 6.1. SEM morphology analysis of DC perovskite on a) 2PACz, b) Me-4PACz and c) MeO-2PACz, as well as MAPI on e) 2PACz, f) Me-4PACz and g) MeO-2PACz. XRD analysis of d) DC and h) MAPI on all SAMs

To confirm the changes in device performance from interfacial energetics rather than morphological differences, we performed SEM and XRD analysis on perovskite films (Figures 6.1). DC perovskite and MAPI films exhibited pure-phase structure, with no significant differences with different SAMs. Except for DC on Me-4PACz, the relative intensity of the 13.8° peak was lost, indicating that the disorder within the film increases and the crystals preferentially oriented along the (110) direction decreases.

Grain sizes were quantified by measuring approximately 120 grains for DC perovskite and 70 grains for MAPI samples. The average grain size was calculated of all measured diameters, with the associated error determined from the standard deviation. A summary of the average grain sizes for DC and MAPI is provided in Table 6.1. The average grain sizes remained consistent across all SAMs. As the observed variations were smaller than the standard deviation, these results confirm that differences in device performance arise from interfacial energetics rather than changes in perovskite morphology.

Table 6.1. Average grain sizes of DC perovskite and MAPI on different SAMs, measured from approximately 120 grains for DC perovskite and 70 grains for MAPI. The values represent the mean grain size ± standard deviation

	2PACz	MeO-2PACz	Me-4PACz
DC Perovskite	274.6 ± 57.5 nm	253.0 ± 60.6 nm	258.6 ± 64.6 nm
MAPI	302.8 ± 81.6 nm	289.5 ± 104.8 nm	276.6 ± 100.1 nm

JV curves obtained from solar simulator measurements further illustrate the impact of SAMs on PSC efficiency (Figure 6.2a and b). The highest-performing devices achieved power conversion efficiencies (PCEs) exceeding 22 % for DC and 20 % for MAPI. While MAPI devices exhibited some hysteresis, the DC perovskite devices displayed hysteresis-free behaviour, as expected for this material system.¹⁷ Photovoltaic performance for the best devices of each SAMs are summarised in Figure 6.2a and b.

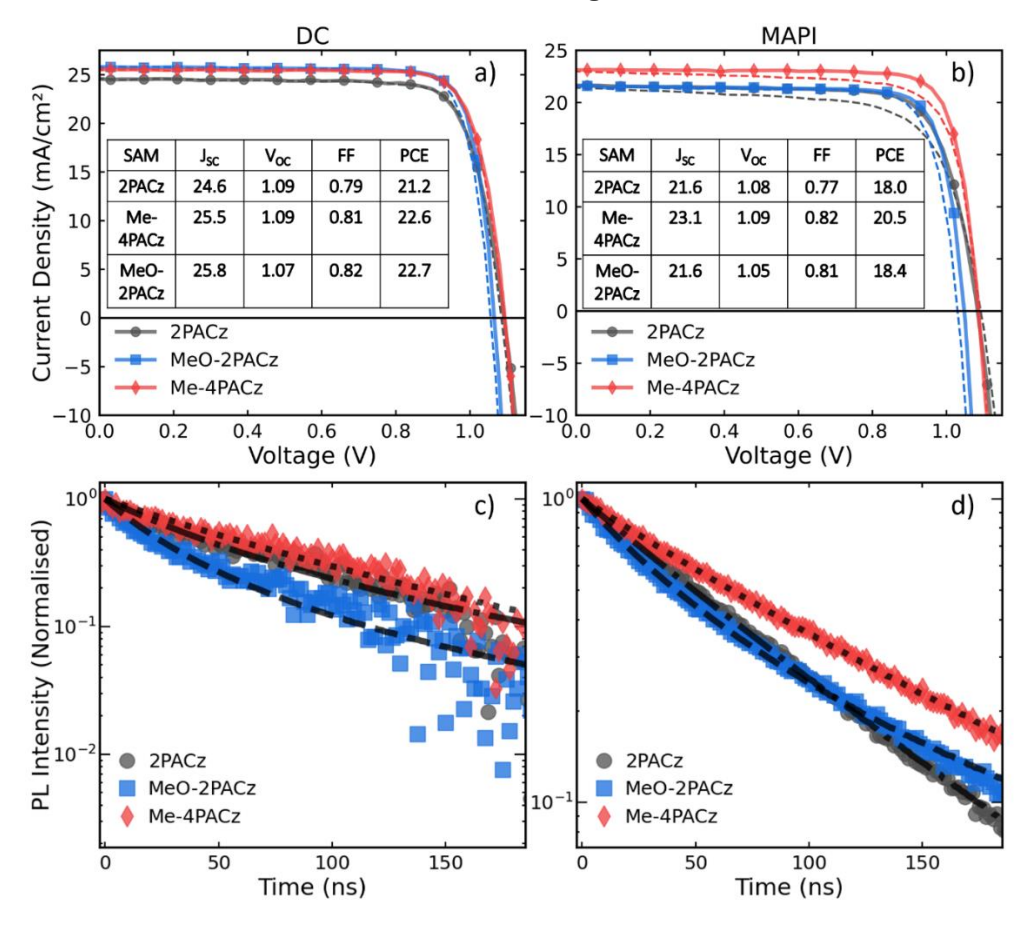


Figure 6.2. JV curves of a) DC perovskite and b) MAPI devices with the forward scans (dashed lines) and the reverse scans (solid lines). Normalised TRPL measurements for

c) DC perovskite and d) MAPI films, measured in configuration of ITO/NiOx/SAM/perovskite¹⁸

The JV curves (Figure 6.2a and b) and statistics analysis (Figure 6.3 and 6.4) indicate that inverted PSCs utilising Me-4PACz consistently exhibit higher Jsc for both perovskites. On the other hand, 2PACz yielded the lowest Jsc, while MeO-2PACz showed intermediate performance. Among all devices, Me-4PACz resulted in the highest PCE compared to MeO-2PACz and 2PACz. Additionally, devices incorporating MeO-2PACz displayed lower Voc than those incorporating 2PACz and Me-4PACz, which exhibited similar Voc values for two perovskite compositions.

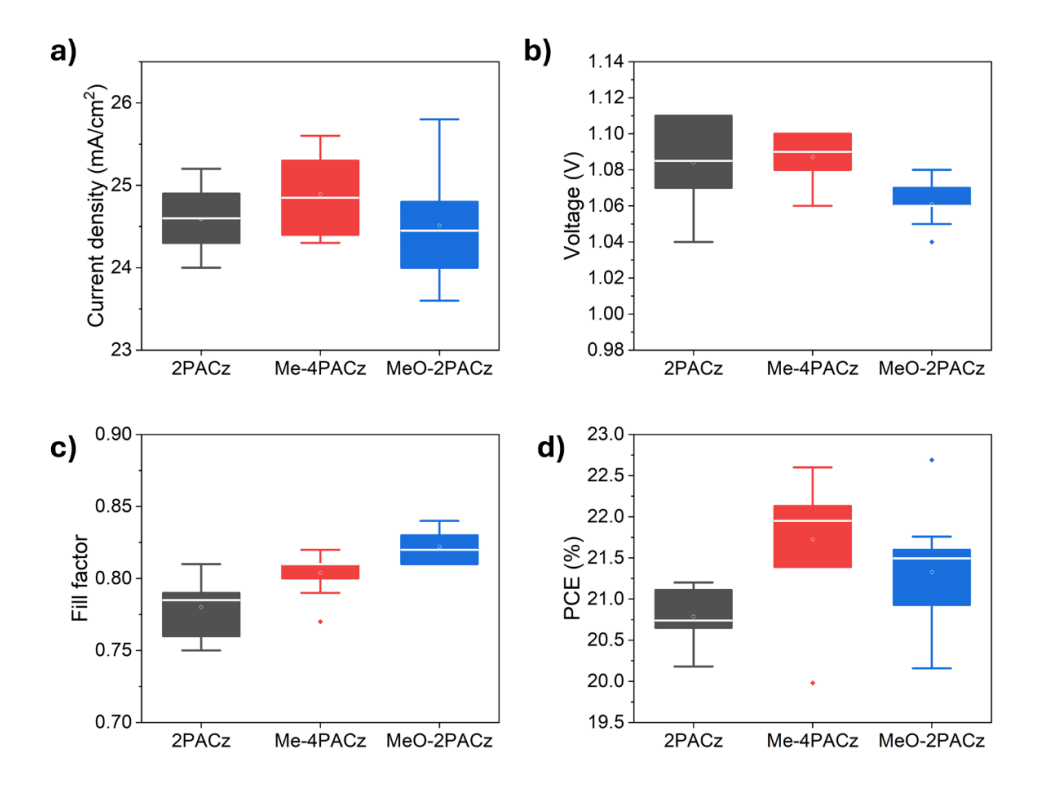


Figure 6.3. Statistical analysis of DC perovskite devices for different SAMs under simulated solar illumination for forward scan; a) Jsc; b) Voc; c) FF and d) PCE. (10 devices for each condition)

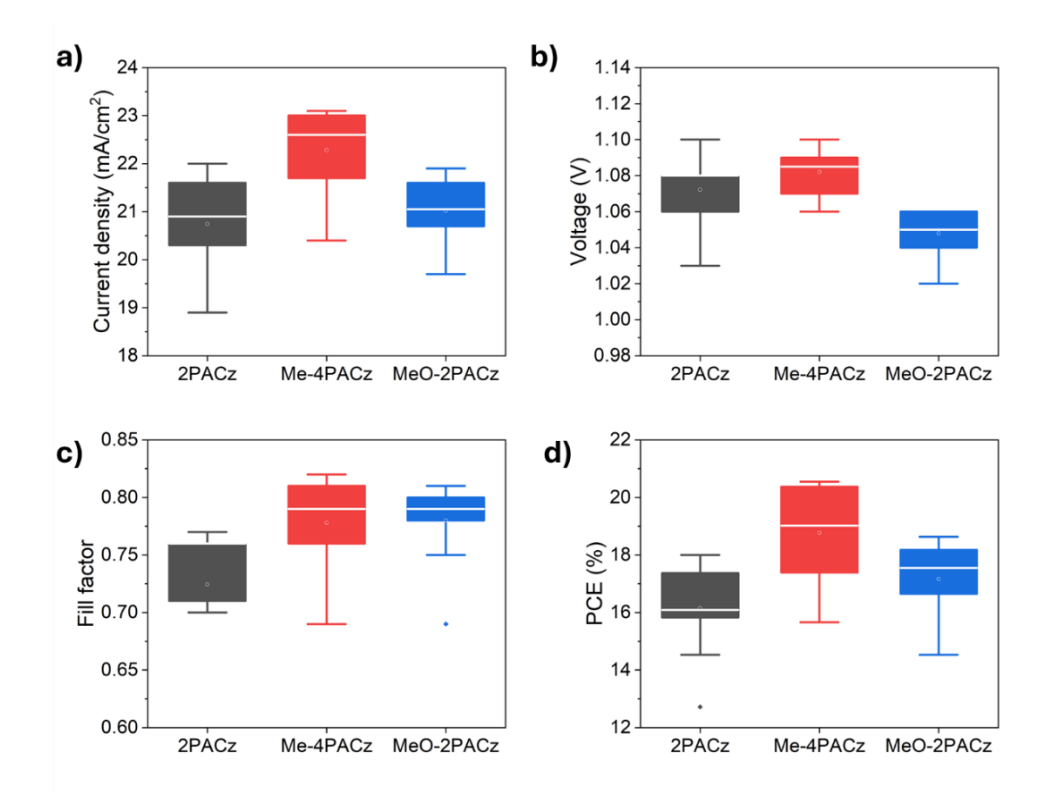


Figure 6.4. Statistical analysis of MAPI devices for different SAMs under simulated solar illumination for forward scan; a) Jsc; b) Voc; c) FF and d) PCE. (10 devices for each condition)

To investigate the charge extraction and recombination of the SAM, TRPL measurements were performed on half device stack: ITO/NiOx/SAM/perovskite (Figure 6.2c and d). The TRPL data were analysed using the PEARs online fitting tool, which employs a bimolecular-trapping-Auger recombination model to extract recombination parameters. The fitting values show in Table 6.2 and 6.3 for DC perovskite and MAPI, respectively. For MAPI films, the TRPL results show that the decay trace for MeO-2PACz exhibited significantly higher bimolecular recombination dynamics (k_2) than Me-4PACz and 2PACz, with k_2 being nearly an order of magnitude greater. The DC perovskite films show similar results, with higher k_2 value for MeO-2PACz compared to Me-4PACz.

Surprisingly, all TRPL exhibited low monomolecular recombination rates (k_1) , a widely reported trend in previous studies. Given the high efficiency of the resulting solar cells, efficient charge extraction at the interface would be expected. However, if charge extraction were highly efficient, the monomolecular recombination rate should dominate,

as is commonly observed in devices employing Spiro-OMeTAD or PEDOT:PSS as HTLs. ^{19,20} The TRPL data suggests that, contrary to conventional assumptions, charge extraction at carbazole-based SAM interfaces may be less efficient, possibly due to charge extraction barriers.

Table 6.2. Extracted TRPL rate values of DC perovskite for different SAMs using the rate equation for the bimolecular-trapping model, obtained using the PEARs fitting tool. (k_1 = rate of monomolecular recombination, k_2 = rate of bimolecular recombination, n = photoexcited carrier concentration = 10^{-15} cm⁻³ and t = time)

$\frac{dn}{dt} = -k_1 n(t) - k_2 n^2(t)$						
SAM	k ₁ (ns ⁻¹)	k ₁ (%)	1/k ₁ (ns)	k ₂ (cm ³ ns ⁻¹)	k ₂ (%)	r ²
2PACz	1.04x10 ⁻³	14.67	961.5	1.80x10 ⁻¹⁸	85.33	0.9402
MeO-2PACz	5x10 ⁻⁴	4.36	2000	3.58x10 ⁻¹⁸	95.64	0.9551
Me-4PACz	3.13x10 ⁻³	52.51	319.5	2x10 ⁻¹⁹	47.49	0.9488

Table 6.3. Extracted TRPL rate values for MAPI for different SAMs sing the rate equation for the bimolecular-trapping model, obtained using the PEARs fitting tool. (k_1 = rate of monomolecular recombination, k_2 = rate of bimolecular recombination, n = photoexcited carrier concentration = 10^{-15} cm⁻³ and t = time)

$\frac{dn}{dt} = -k_1 n(t) - k_2 n^2(t)$						
SAM	k ₁ (ns ⁻¹)	k₁ (%)	1/k₁ (ns)	k ₂ (cm ³ ns ⁻¹)	k ₂ (%)	r²
2PACz	5.66x10 ⁻³	83.26	176.7	3.24x10 ⁻¹⁹	16.74	0.9994
MeO-2PACz	2.87x10 ⁻⁴	4.22	3484.32	1.93x10 ⁻¹⁸	95.78	0.9985
Me-4PACz	3.37x10 ⁻³	67.12	296.7	4.51x10 ⁻¹⁹	32.89	0.9989

To gain further insight, KPFM measurements was conducted under dark and illuminated conditions (Figure 6.5). The results show that the surface potential of perovskite films deposited on MeO-2PACz did not change significantly (Figure 6.5h and i), indicating the recombination of charge carriers. This aligns with the increased overlap of electron and hole populations observed in the TRPL results. Conversely, KPFM images of

perovskite films incorporating 2PACz (Figure 6.5b and c) and Me-2PACz (Figure 6.5e and f) showed a distinct change in surface potential upon illumination, signifying effective charge separation and interfacial band bending. It should be noted, however, that measurements on partial device stacks may not fully represent the complex interfacial energetics present in a complete solar cell. This is particularly relevant for p-i-n PSC architectures that utilise SAMs and 3D/2D absorber layers, where energy level alignment can be more intricate.²¹

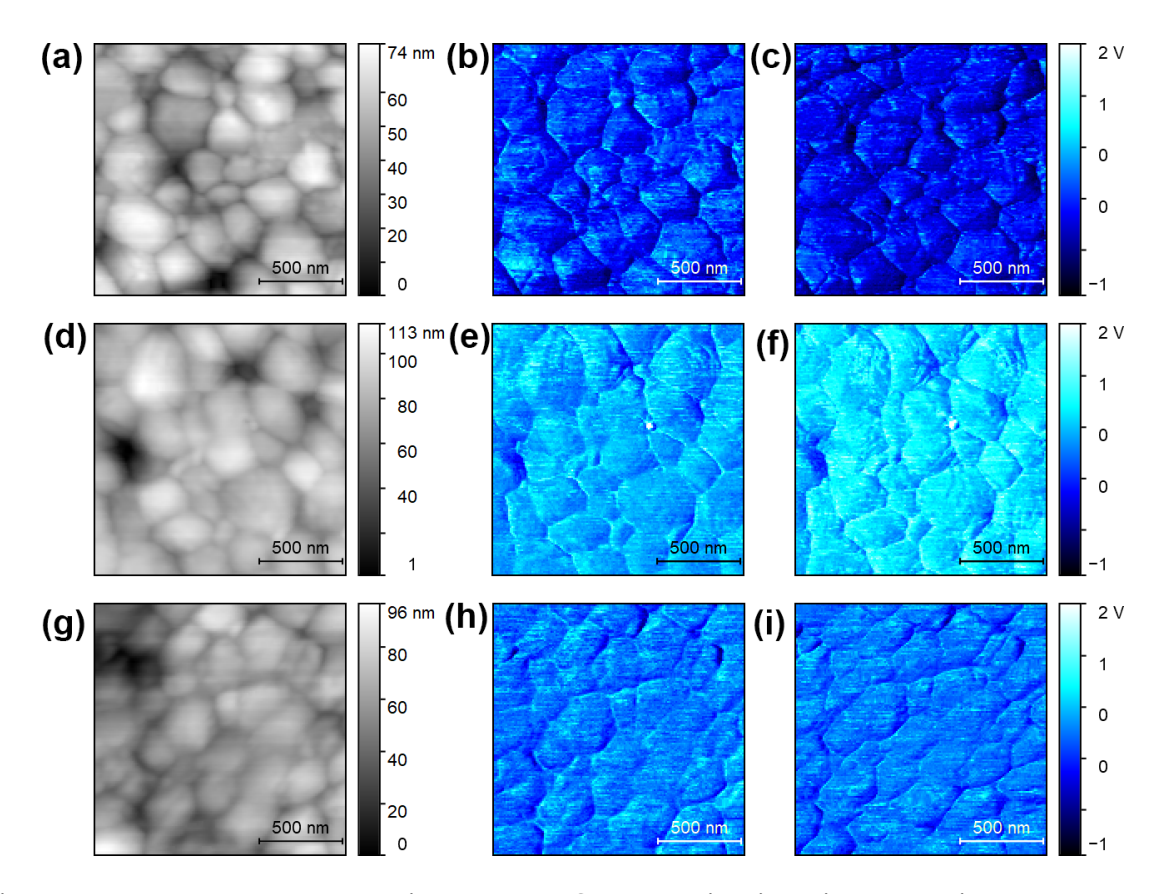


Figure 6.5.AFM (left) and KPFM images of DC perovskite films in dark (middle) and under illumination (right) on different SAMs: a-c) 2PACz; d-f) Me-4PACz and g-i) MeO-2PACz with the partial device stack (ITO/NiOx NPs/SAMs/DC perovskite)

We then performed SaP measurements for inverted PSCs devices to link the energy alignment and device performance.^{22,23} The complete JV curves obtained *via* SaP measurements are presented in Figure 6.6 for both perovskite compositions. These curves clearly illustrate the impact of ions on charge extraction. For the MeO-2PACz in both perovskite compositions, there is a little to no change in shape of the JV curves,

indicating that mobile ions in the perovskite do not affect the charge extraction. This suggests lower surface recombination, with bulk recombination dominating. In contrast, for the 2PACz and Me-4PACz, changes in the JV curves are observed compared to MeO-2PACz. In the case of 2PACz, the large variation in Voc is attributed to increased surface recombination due to energetic barrier created by the strong dipole moment. For Me-4PACz, the change in Jsc at high voltage indicates that ions are impacting charge extraction, likely due to interfacial recombination.

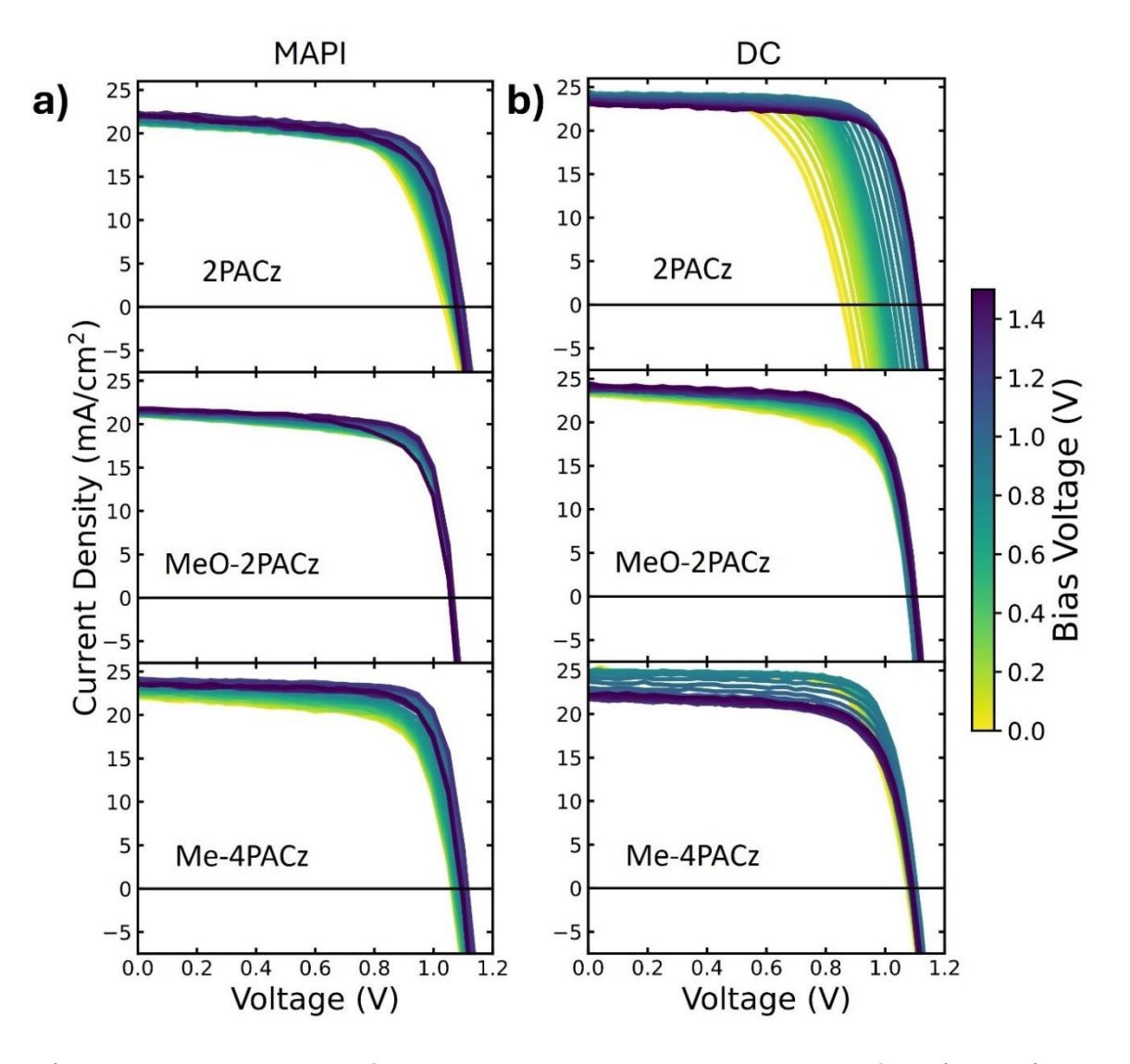


Figure 6.6. JV curves from SaP measurements for a) MAPI and b) DC devices using different SAMs

For further confirmation, the derivative of current density with respect to voltage (dJ/dV) is plotted against the stabilisation bias in Figure 6.7 to represent the distribution

of mobile ion (detail explanation provided in section 3.3.9 of chapter 3). The data is it is normalised for direct comparisons across devices. The slope of the dJ/dV curve reflects the interplay between ion-modulated interfacial recombination and bulk losses, The interface becomes less dominant with bulk recombination increased, resulting in a less pronounced slope in the dJ/dV curve. In MAPI-based devices, which contain a high density of mobile ions (10¹⁷ to 10¹⁹ cm⁻³), ²⁴⁻²⁷ interfacial recombination is dominant, leading to more pronounced slopes in dJ/dV analysis. As a result, JV hysteresis was observed in most MAPI-based solar cells. In contrast, DC perovskites contain fewer and slower-diffusing mobile ions,²⁴ reducing interfacial recombination and JV hysteresis, which results in a shallower dJ/dV slope. The extracted data further confirms that MAPI devices provide more accurate dJ/dV fits, whereas DC perovskite devices display a noisier response. Furthermore, the DC perovskite devices with MeO-2PACz exhibits a shallower dJ/dV slope compared to other devices, indicating less ionic effects and an increased bulk-to-surface recombination ratio, which is consistent with the TRPL and KPFM.

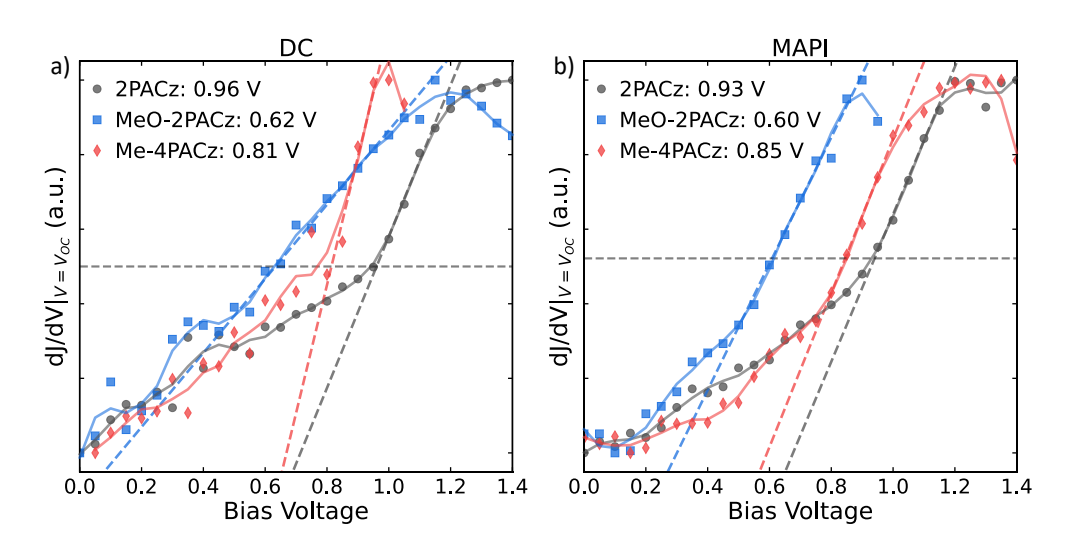


Figure 6.7. dJ/dV analysis of devices of a) MAPI and b) DC perovskite with different SAMs

To verify that ion migration effects were properly accounted for, MAPI and DC perovskite on MeO-2PACz were examined as examples. JV curves were reconstructed from SaP measurements, and Figure 6.8a and 6.8b shows no hysteresis of the reverse and forward scans. The overlapping curves confirm the absence of significant ion migration during the measurements. Additionally, current density versus time plots

remained stable throughout the measurement process, indicating that ionic redistribution had stabilised before the voltage pulse was applied. To further confirm this, the deviation of current (J) from the mean current (J_{mean}) over final 30 seconds before pulsing was plotted in Figure 6.8c and 6.8d. The resulting values near zero confirm that no substantial ionic movement occurred during this period.

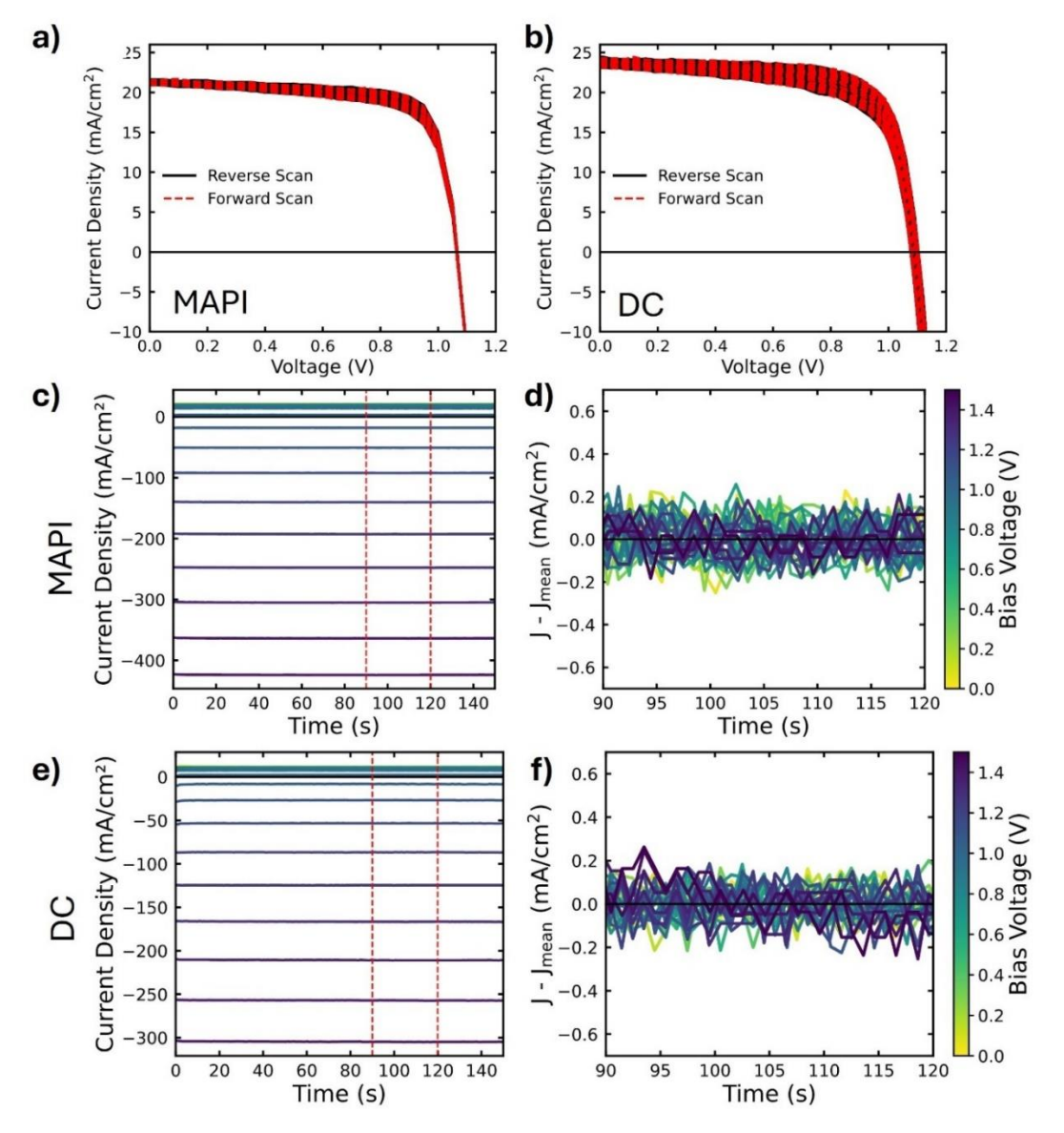


Figure 6.8. JV data from SaP measurement of MeO-2PACz on a) MAPI and b) DC perovskite with contrasting colours to highlight both scans taken during the measurement (reverse scans in black and forward scans in dashed red); Stabilisation data obtained during SaP measurement. Left: Full current density output obtained during each applied bias for MeO-2PACz on c) MAPI and e) DC perovskite. The red

dashed lines indicate the final 30 seconds before pulsing for stability analysis. Right: the current minus the average current during the final 30s before pulsing beginning for MeO-2PACz on d) MAPI and f) DC perovskite, confirming that the ionic configuration was stable before pulsing

From these curves, the flat ion potential (V_{flat}) values were determined to be approximately 0.9 V, 0.6 V and 0.8 V for 2PACz, MeO-2PACz and Me-4PACz, respectively. Table 6.4 summarised the extracted values. The data highlights a correlation between interfacial potential drops and SAM dipole strength of different SAMs. The trend is further validated using Cl-2APCz with a larger dipole moment (~4.6 D) than other SAMs. ^{28,29} Devices with Cl-2PACz exhibited significantly higher V_{flat} values for both perovskite devices (1.19 V for DC and 1.34 V for MAPI), confirming that higher dipole moments correspond to increased V_{flat}, as shown in Figure 6.9.

Table 6.4. Comparison of dipole moment and the flat ion potentials for the different SAMs on MAPI and DC

SAM	Dipole Moment	DC (V _{flat})	MAPI (V _{flat})
2PACz	~ 2 D ¹³	0.96 ± 0.05 V	0.93 ± 0.05 V
Me-4PACz	~ 1.5 D ¹⁴	0.81 ± 0.05 V	0.85 ± 0.05 V
MeO-2PACz	~ 0.2 D ¹³	0.62 ± 0.05 V	0.60 ± 0.05 V
Cl-2PACz	~ 4.6 D ^{28,29}	1.19 ± 0.05 V	1.34 ± 0.05 V

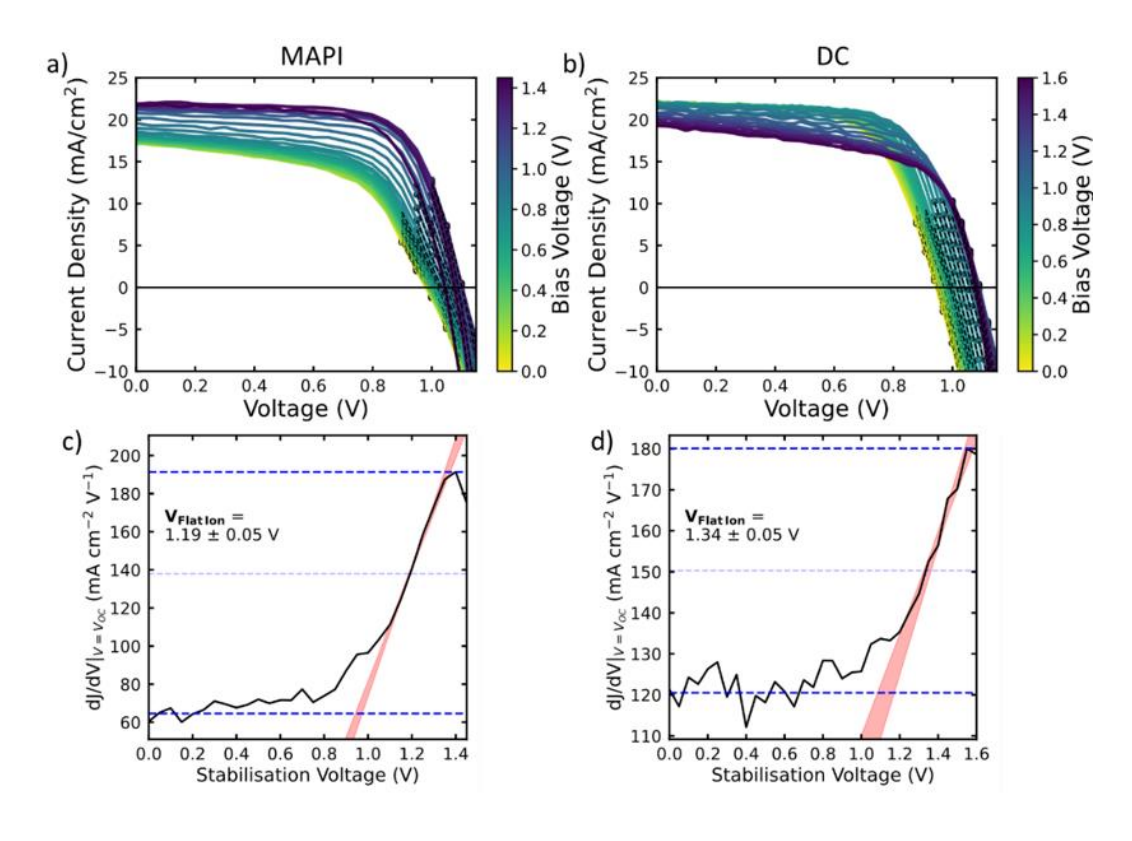


Figure 6.9. JV curves from SaP measurement utilising Cl-2PACz for a) MAPI and b) DC perovskite. dJ/dV analysis for Cl-2PACz-based devices for c) MAPI and d) DC

These findings are further supported by the consistency of the values obtained between DC and MAPI when using same SAMs. This agreement is expected because of the similar bandgaps exhibited by both perovskite compositions, as shown by UV-vis absorption and Tauc analysis: 1.49 eV for DC perovskite and 1.54 eV for MAPI, as shown in Figure 10. Given their comparable conduction and valence bands, as well as Fermi level alignments, the extract $V_{\rm flat}$ values are solely attributed to Fermi levels induced by the SAMs on ITO surface.

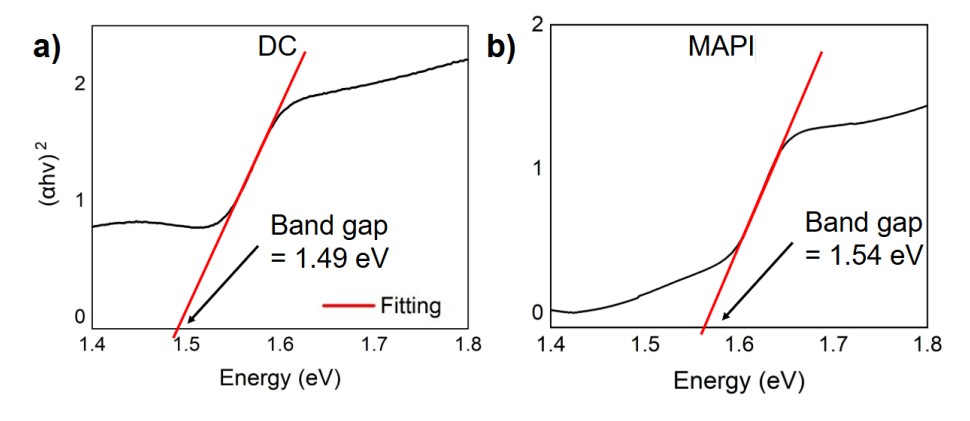


Figure 6.10. Tauc analysis of a) DC perovskite and b) MAPI

To verify the accuracy of the SaP measurements, the V_{flat} values were compared with expected energetic offsets derived from XPS/UPS studies by Siekmann *et al.*¹⁵ These results indicate Fermi level shifts of -5.2 eV, -5.0 eV and -4.8 eV for 2PACz, Me-4PACz and MeO-2PACz, respectively. These values correspond to the dipole strength of the SAMs, where a stronger dipole leads to a greater Fermi level shift.

Considering PCBM's reported Fermi level (-4.2 eV), 30,31 a conservative estimate of the Fermi level difference between the charge transport layers suggests values of 1.0 eV for 2PACz, 0.80 eV for Me-4PACz, and 0.60 eV for MeO-2PACz. These estimations closely match the extracted V_{flat} values of 0.93, 0.85 and 0.60 ± 0.05 V respectively for MAPI and DC perovskite. This strong correlation underscores the reliability of the SaP measurement technique in assessing interfacial energetic modification in highly efficient PSCs, which exhibited lower mobile ion densities and minimal hysteresis.

Analysing the impact of Fermi level shifts on SAM-based device, Figures 6.3 and 6.4 show that devices with MeO-2PACz exhibit losses in both Voc and Jsc. This reduction in Jsc is counterintuitive when considering the energetic framework of the solar cell in Figure 6.11. According to conventional understanding, this device configuration should yield the highest J_{SC} due to the offset at the HTL/Perovskite interface, which, in theory, should enhance charge extraction by providing an additional driving force.³²

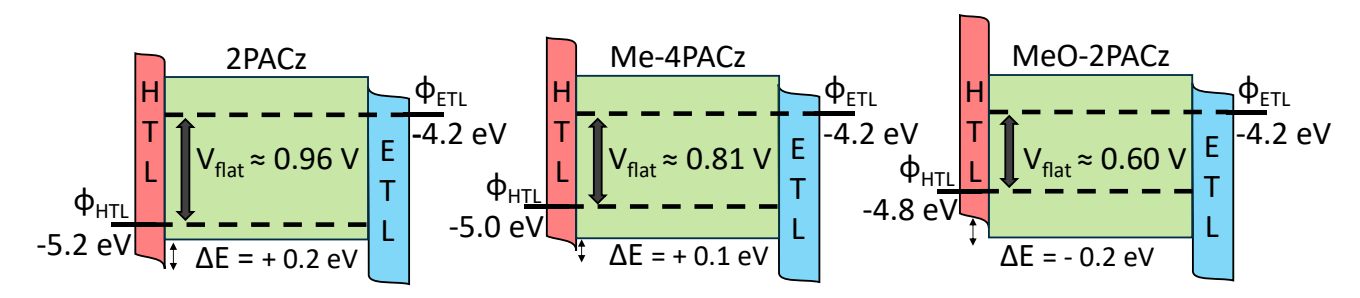


Figure 6.11. Energy level diagrams for inverted PSCs incorporating each SAM layer (HTL: NiOx/SAM and ETL: PCBM). The perovskite valence band edge is -5.4 eV from literature. The electrostatic potential drop across the perovskite layer extracted from the SaP measurements is labelled as V_{flat} . The energetic offset from the valence band of the perovskite to the valence band of the HTL is labelled ΔE and is estimated from values obtained from the literature 15

The built-in potential driven by the adjacent charge transport layers is approximately equal to V_{flat} in this device structure. Our previous work demonstrates that in 'high-injection limited' cases, where interfacial recombination is not the limiting factor, reducing the built-in potential results in a loss of both Jsc and Voc.²³ Ionic field screening leads to increased overlap of electron and hole populations, thereby enhancing bulk recombination rates. The significantly lower V_{flat} observed in MeO-2PACz-based devices aligns with TRPL data, which indicated a higher bimolecular recombination rate compared to SAM layer. This conclusion is further supported by KPFM measurements, where there is no surface potential difference before and after illumination.

The highest V_{flat} was obtained using 2PACz as HTL, which is attributed to its strong dipole moment. This resulted in an increase in Voc but a decrease in Jsc compared to the MeO-2PACz device. According to the Figure 6.11, the current loss is attributed to the small energy barrier at the interface, as the valence band of the SAM-modified NiOx layer is deeper than that of the DC and MAPI, resulting in hole accumulation at the interface and increased recombination kinetics.

In contrast, Me-4PACz exhibit the highest Jsc and Voc values, attributing to the optimal alignment of the SAM-modified NiOx valence band with that of perovskite. The small energetic offset (~0.1 eV) minimises charge accumulation and recombination compared to 2PACz, while the build-in potential remains sufficiently high to achieve the high Voc required for efficient operation. This conclusion is reinforced by the TRPL measurements, which revealed the slowest decay kinetics for Me-4PACz-based devices. The KPFM results show a charge build-up at the exposed perovskite surface after illumination, further confirmed the existence of a small potential barrier for charge extraction at the SAM/perovskite interface.

Device performance data indicate that this potential barrier does not adversely affect efficiency. Similar findings were reported by Xu et al. who demonstrated that an ETL with a slight barrier to charge extraction could still achieve high PCEs.³³ In fact, a small energetic offset at the interface can be beneficial for increasing the Voc, as shown by Chen et al. in devices that incorporated layered perovskites as interface modifiers.³⁴ This

observation signs with the increased Voc measured in devices utilising 2PACz and Me-4PACz in this study.

6.3. Conclusions

Using an advanced SaP measurement technique, we have systemically investigated how SAM-induced Fermi-level positioning affects the performance of high-efficiency inverted PSCs. This method enabled the determination of V_{flat} for two different perovskite compositions. The measured V_{flat} values for devices were 0.6 V for MeO-2PACz, 0.8 V for Me-4PACz, and 0.95 V for 2PACz, with consistent trends observed across both perovskites. Our findings demonstrate a clear correlation between low V_{flat} values and reduced Jsc and Voc. Device performance significantly improved when V_{flat} reached 0.80 V but further increases provided no additional benefit. This limitation is attributed to the stronger dipole of 2PACz, which shifts the valence band deeper than that of the perovskites, creating an interfacial energy barrier that impedes charge extraction. Supporting evidence from KPFM and TRPL measurements further validated this interpretation. KPFM revealed substantial differences in surface potential between dark and illuminated conditions for device with higher V_{flat} , indicating the presence of an energy barrier. TRPL results showed reduced monomolecular recombination rates, further suggesting inefficient charge extraction due to this barrier. These insights highlight the importance of selecting the appropriate SAM for a given device architecture to optimise performance. For example, the higher V_{flat} induced by 2PACz may necessitate a bromide-based perovskite, which can deepen the valence band and mitigate energy barrier formation. In contrast, low-bandgap perovskites may benefit more from MeO-2PACz, which induces a lower V_{flat} . This study demonstrates the value of thorough material characterization in identifying most suitable SAM for improving solar cell efficiency.

6.4. References

- 1 C. Eames, J. M. Frost, P. R. F. Barnes, B. C. O'Regan, A. Walsh and M. S. Islam, *Nat Commun*, 2015, **6**, 7497.
- 2 Y. Hu, J. Schlipf, M. Wussler, M. L. Petrus, W. Jaegermann, T. Bein, P. Müller-Buschbaum and P. Docampo, *ACS Nano*, 2016, **10**, 5999–6007.
- 3 Q. Jiang, Y. Zhao, X. Zhang, X. Yang, Y. Chen, Z. Chu, Q. Ye, X. Li, Z. Yin and J. You, *Nat Photonics*, 2019, **13**, 460–466.
- 4 A. Abrusci, S. D. Stranks, P. Docampo, H.-L. Yip, A. K.-Y. Jen and H. J. Snaith, *Nano Lett*, 2013, **13**, 3124–3128.
- 5 Z. Dai, S. K. Yadavalli, M. Chen, A. Abbaspourtamijani, Y. Qi and N. P. Padture, *Science*, 2021, **372**, 618–622.
- 6 L. Zuo, Z. Gu, T. Ye, W. Fu, G. Wu, H. Li and H. Chen, *JAm Chem Soc*, 2015, **137**, 2674–2679.
- 7 D. Kim, H. Lee, S. Lee, Y. Kang, S. Kwon, D. Kim and S. Na, *Solar RRL*, 2024, **8**, 2400067.
- 8 R. Mishima, M. Hino, M. Kanematsu, K. Kishimoto, H. Ishibashi, K. Konishi, S. Okamoto, T. Irie, T. Fujimoto, W. Yoshida, H. Uzu, D. Adachi and K. Yamamoto, *Applied Physics Express*, 2022, **15**, 076503.
- Q. Ou, Y. Zhang, Z. Wang, J. A. Yuwono, R. Wang, Z. Dai, W. Li, C. Zheng, Z. Xu, X. Qi,
 S. Duhm, N. V. Medhekar, H. Zhang and Q. Bao, *Advanced Materials*, 2018, 30,
 1705792
- 10 C. Li, S. Tscheuschner, F. Paulus, P. E. Hopkinson, J. Kießling, A. Köhler, Y. Vaynzof and S. Huettner, *Advanced Materials*, 2016, **28**, 2446–2454.
- 11 N. Phung, M. Verheijen, A. Todinova, K. Datta, M. Verhage, A. Al-Ashouri, H. Köbler, X. Li, A. Abate, S. Albrecht and M. Creatore, *ACS Appl Mater Interfaces*, 2022, **14**, 2166–2176.
- 12 K. Hossain, A. Kulkarni, U. Bothra, B. Klingebiel, T. Kirchartz, M. Saliba and D. Kabra, *ACS Energy Lett*, 2023, **8**, 3860–3867.
- A. Al-Ashouri, A. Magomedov, M. Roß, M. Jošt, M. Talaikis, G. Chistiakova, T. Bertram, J. A. Márquez, E. Köhnen, E. Kasparavičius, S. Levcenco, L. Gil-Escrig, C. J. Hages, R. Schlatmann, B. Rech, T. Malinauskas, T. Unold, C. A. Kaufmann, L. Korte, G. Niaura, V. Getautis and S. Albrecht, *Energy Environ Sci*, 2019, **12**, 3356–3369.
- 14 A. Sun, C. Tian, R. Zhuang, C. Chen, Y. Zheng, X. Wu, C. Tang, Y. Liu, Z. Li, B. Ouyang,

- J. Du, Z. Li, J. Cai, J. Chen, X. Wu, Y. Hua and C. Chen, *Adv Energy Mater*, 2024, **14**, 2303941.
- 15 J. Siekmann, A. Kulkarni, S. Akel, B. Klingebiel, M. Saliba, U. Rau and T. Kirchartz, *Adv Energy Mater*, 2023, **13**, 2300448.
- 16 S. Sajid, A. M. Elseman, H. Huang, J. Ji, S. Dou, H. Jiang, X. Liu, D. Wei, P. Cui and M. Li, *Nano Energy*, 2018, **51**, 408–424.
- 17 D. Kang and N. Park, *Advanced Materials*, 2019, **31**, 1805214.
- 18 E. V. Péan and M. L. Davies, *J Chem Inf Model*, 2023, **63**, 4477–4482.
- 19 P. Docampo, J. M. Ball, M. Darwich, G. E. Eperon and H. J. Snaith, *Nat Commun*, 2013, **4**, 2761.
- S. D. Stranks, G. E. Eperon, G. Grancini, C. Menelaou, M. J. P. Alcocer, T. Leijtens, L.
 M. Herz, A. Petrozza and H. J. Snaith, *Science*, 2013, 342, 341–344.
- 21 Y. Wang, J. Lin, Y. He, Y. Zhang, Q. Liang, F. Liu, Z. Zhou, C. C. S. Chan, G. Li, S.-P. Feng, A. M. C. Ng, K. S. Wong, J. Popović and A. B. Djurišić, *Solar RRL*, 2022, 6, 2200224
- 22 N. S. Hill, M. V. Cowley, N. Gluck, M. H. Fsadni, W. Clarke, Y. Hu, M. J. Wolf, N. Healy, M. Freitag, T. J. Penfold, G. Richardson, A. B. Walker, P. J. Cameron and P. Docampo, Advanced Materials, 2023, 35, 2302146.
- 23 L. J. F. Hart, F. J. Angus, Y. Li, A. Khaleed, P. Calado, J. R. Durrant, A. B. Djurišić, P. Docampo and P. R. F. Barnes, *Energy Environ Sci*, 2024, **17**, 7107-7118.
- 24 L. Bertoluzzi, C. C. Boyd, N. Rolston, J. Xu, R. Prasanna, B. C. O'Regan and M. D. McGehee, *Joule*, 2020, **4**, 109–127.
- 25 M. Sajedi Alvar, P. W. M. Blom and G. A. H. Wetzelaer, *Adv Electron Mater*, 2020, **6**, 1900935.
- 26 A. Walsh, D. O. Scanlon, S. Chen, X. G. Gong and S. Wei, *Angewandte Chemie*, 2015,127, 1811–1814.
- 27 S. G. McCallum, O. Nicholls, K. O. Jensen, M. V Cowley, J. E. Lerpinière and A. B. Walker, *Journal of Physics: Energy*, 2024, **6**, 015005.
- Y. Lin, Y. Zhang, J. Zhang, M. Marcinskas, T. Malinauskas, A. Magomedov, M. I. Nugraha, D. Kaltsas, D. R. Naphade, G. T. Harrison, A. El-Labban, S. Barlow, S. De Wolf, E. Wang, I. McCulloch, L. Tsetseris, V. Getautis, S. R. Marder and T. D. Anthopoulos, *Adv Energy Mater*, 2022, 12, 2202503.
- 29 Y. Wang, W. Jiang, S. Liu, C. Lin, B. Fan, Y. Li, H. Gao, M. Liu, F. R. Lin and A. K. -Y. Jen,

- Adv Energy Mater, 2024, 14, 2303354.
- 30 J. H. Lee, J.-H. Shin, J. Y. Song, W. Wang, R. Schlaf, K. J. Kim and Y. Yi, *The Journal of Physical Chemistry C*, 2012, **116**, 26342–26348.
- 31 P. Reiser, F. S. Benneckendorf, M.-M. Barf, L. Müller, R. Bäuerle, S. Hillebrandt, S. Beck, R. Lovrincic, E. Mankel, J. Freudenberg, D. Jänsch, W. Kowalsky, A. Pucci, W. Jaegermann, U. H. F. Bunz and K. Müllen, *Chemistry of Materials*, 2019, **31**, 4213–4221.
- 32 M. Mohan, V. Nandal, S. Paramadam, K. P. Reddy, S. Ramkumar, S. Agarwal, C. S. Gopinath, P. R. Nair and M. A. G. Namboothiry, *The Journal of Physical Chemistry C*, 2017, **121**, 5523–5530.
- 33 W. Xu, L. J. F. Hart, B. Moss, P. Caprioglio, T. J. Macdonald, F. Furlan, J. Panidi, R. D. J. Oliver, R. A. Pacalaj, M. Heeney, N. Gasparini, H. J. Snaith, P. R. F. Barnes and J. R. Durrant, *Adv Energy Mater*, 2023, **13**, 2301102.
- 34 H. Chen, A. Maxwell, C. Li, S. Teale, B. Chen, T. Zhu, E. Ugur, G. Harrison, L. Grater, J. Wang, Z. Wang, L. Zeng, S. M. Park, L. Chen, P. Serles, R. A. Awni, B. Subedi, X. Zheng, C. Xiao, N. J. Podraza, T. Filleter, C. Liu, Y. Yang, J. M. Luther, S. De Wolf, M. G. Kanatzidis, Y. Yan and E. H. Sargent, *Nature*, 2023, 613, 676–681.

Chapter 7. Conclusion and Future Work

This thesis explored charge transport layer (CTLs) in inverted perovskite solar cells (PSCs) through doping and interfacial engineering, with focus on non-fullerene organic semiconductors as electron transport materials (ETMs) and the role of self-assembled monolayer (SAMs) in tuning interfacial properties. By investigating bisflavin (BF) and naphthalenediimide (NDI) derivatives as alternative ETMs, we examined their conductivity properties and n-type doping mechanisms. Additionally, the influence of SAM-induced dipole moments on interfacial energetics was systematically studied using a novel Stabilisation and Pulse (SaP) measurement technique. These approaches demonstrated the critical role of interfacial engineering in optimising PSC efficiency.

This work highlighted the potential of bio-inspired BF derivatives as n-type organic ETMs, with pristine BF-based devices achieving power conversion efficiencies (PCEs) of approximately 7%, along with respectable Jsc and Voc values. However, efforts to enhance their conductivity through n-type doping with N-DMBI revealed significant challenges. Glycol-functionalised BFG exhibited faster electron transfer than alkylfunctionalised BFA, attributed to improved molecular interactions between its polar side chains and the dopant. Despite this, doping not significantly enhance conductivity or device performance. Density functional theory (DFT) calculations revealed that both BFG and BFA tend to form stable charge transfer complexes (CTCs) upon doping due to strong binding energies, making electron transfer to the LUMO of neutral molecules energetically unfavourable. This resulted in ineffective n-type doping, explaining the limited conductivity improvements observed experimentally.

Further investigations into NDI-derivatives, including NDI-G (glycol-functionalized) and NDI-EtHx (ethylhexyl-functionalized), showed similar doping behaviour to BF derivatives when treated with N-DMBI. NDI-G exhibited faster doping reactivity than NDI-EtHx, attributed to better polarity compatibility between the molecule and dopant. The proposed doping mechanism involves the electron transfer from N-DMBI, facilitating the formation of the NDI anion radical. This was confirmed through electron paramagnetic resonance (EPR) and UV-vis absorption measurements, supported by DFT calculations indicating CTC formation stabilized by strong binding energies. Unlike BF derivatives, the

energy alignment between the CTC and neutral NDI molecules facilitated efficient electron transfer, generating free charge carriers. Optimized doping of NDI-G achieved a conductivity of 10⁻² S/cm, surpassing many reported molecular charge transport materials, including PCBM. This improvement led to reduced series resistance (Rs) and enhanced charge transport in PSCs. However, despite its superior conductivity, doped NDI-G devices exhibited lower overall efficiency compared to PCBM-based devices, due to increased interfacial recombination and hysteresis. These results highlight that effective interface passivation is more critical than simply reducing Rs in the charge extraction layer for achieving optimal device performance.

The study also explored the impact of SAMs on the Fermi level position in high efficiency inverted PSCs using a novel stabilization and pulse (SaP) measurement technique. By measuring the flat ion potential (V_{flat}) between HTL and perovskite layer, it was observed that variations in SAMs-induced dipole moment significantly influenced the V_{flat}, and consequently, device performance. The SAMs MeO-2PACz, Me-4PACz and 2PACz yielded V_{flat} values of 0.60 V, 0.80 V and 0.95 V, respectively. A low V_{flat} was associated with losses in both Jsc and Voc. Maximum performance was achieved at an intermediate V_{flat} of 0.80 V, while further increases, as with 2PACz, did not yield additional improvements. Instead, a stronger dipole of 2PACz lead to formation of an interfacial energy barrier forming between the HTL and perovskite layer, as confirmed by KPFM and TRPL measurements. These results explain why different SAMs yield optimal device performance depending on the device architecture.

This thesis contributes to the understanding of doping mechanism in n-type organic ETMs and the role of SAM-induced interfacial engineering in inverted PSCs. Future research could incorporate DFT calculations during the design phase of ETMs to predict the potential for CTC formation and binding energies, as well as to further study energy alignment with materials for specific applications. Additionally, side-chain modification offers a viable approach to improving n-type doping efficiency by increasing molecular polarity and improving dopant compatibility. The SaP measurement results suggest the dipole moment of SAMs controls the built-in potential, and the use of mixed SAMs could provide a strategy to fine-tune the dipole moment of the HTL, optimizing the Fermi level

alignment at the HTL/perovskite interface for efficient charge extraction.